








CO₂-driven surface changes in the Hapi region on Comet 67P/Churyumov–Gerasimenko

Björn J. R. Davidsson ¹★, F. Peter Schloerb,² Sonia Fornasier ^{3,4}, Nilda Oklay,⁵ Pedro J. Gutiérrez ⁶, Bonnie J. Buratti,⁷ Artur B. Chmielewski,⁸ Samuel Gulkis,⁹ Mark D. Hofstadter,¹⁰ H. Uwe Keller,^{11,12} Holger Sierks,¹³ Carsten Güttler ¹³, Michael Küppers,¹⁴ Hans Rickman,^{15,16} Mathieu Choukroun,⁷ Seungwon Lee,¹⁷ Emmanuel Lellouch,³ Anthony Lethuillier ¹¹, Vania Da Deppo,¹⁸ Olivier Groussin,¹⁹ Ekkehard Kührt,²⁰ Nicolas Thomas,²¹ Cecilia Tubiana ²², M. Ramy El-Maarry,²³ Fiorangela La Forgia ²⁴, Stefano Mottola¹² and Maurizio Pajola²⁵

Affiliations are listed at the end of the paper

Accepted 2022 September 5. Received 2022 August 8; in original form 2022 May 4

ABSTRACT

Between 2014 December 31 and 2015 March 17, the OSIRIS cameras on *Rosetta* documented the growth of a 140-m wide and 0.5-m deep depression in the Hapi region on Comet 67P/Churyumov–Gerasimenko. This shallow pit is one of several that later formed elsewhere on the comet, all in smooth terrain that primarily is the result of airfall of coma particles. We have compiled observations of this region in Hapi by the microwave instrument MIRO on *Rosetta*, acquired during October and November 2014. We use thermophysical and radiative transfer models in order to reproduce the MIRO observations. This allows us to place constraints on the thermal inertia, diffusivity, chemical composition, stratification, extinction coefficients, and scattering properties of the surface material, and how they evolved during the months prior to pit formation. The results are placed in context through long-term comet nucleus evolution modelling. We propose that (1) MIRO observes signatures that are consistent with a solid-state greenhouse effect in airfall material; (2) CO₂ ice is sufficiently close to the surface to have a measurable effect on MIRO antenna temperatures, and likely is responsible for the pit formation in Hapi observed by OSIRIS; (3) the pressure at the CO₂ sublimation front is sufficiently strong to expel dust and water ice outwards, and to compress comet material inwards, thereby causing the near-surface compaction observed by CONSERT, SESAME, and groundbased radar, manifested as the ‘consolidated terrain’ texture observed by OSIRIS.

Key words: conduction – diffusion – radiative transfer – methods: numerical – techniques: radar astronomy – comets: individual: 67P/Churyumov–Gerasimenko.

1 INTRODUCTION

Near-nucleus operations of the ESA *Rosetta/Philae* spacecraft (Glassmeier et al. 2007) at Comet 67P/Churyumov–Gerasimenko (hereafter, 67P) began 2014 August 6 and ended 2016 September 30 (Taylor et al. 2017). The OSIRIS (Keller et al. 2007) Narrow Angle Camera (NAC) and Wide Angle Camera (WAC) revealed a geologically diverse landscape with two major types of morphological units: *consolidated terrain* that constitutes topographically complex structures, and *smooth terrain* dominated by $\lesssim 1$ cm-sized chunks (Mottola et al. 2015; Pajola et al. 2017) that form vast plains (e.g. Sierks et al. 2015; Thomas et al. 2015a; El-Maarry et al. 2015b) that closely follow equipotential surfaces (i.e. slopes with respect to the local gravity field are small, often $<5^\circ$; Auger et al. 2015; Sierks et al. 2015; Pajola et al. 2019). The Southern hemisphere, that is strongly illuminated near perihelion (Keller et al. 2015b), consists primarily of exposed consolidated terrain (El-Maarry et al. 2016).

The Southern hemisphere is a source of large coma particles that rain down on the Northern hemisphere (that experiences polar night near perihelion) as airfall (Keller et al. 2015b, 2017; Thomas et al. 2015b; Hu et al. 2017; Davidsson et al. 2021). Airfall thereby contributes to the formation of smooth terrain, often on top of partially exposed consolidated terrain (Thomas et al. 2015a, b; El-Maarry et al. 2015b).

In May 2015, three months pre-perihelion, the large (0.8 km²) smooth terrain at Imhotep (for region names and definitions, see Thomas et al. 2018) started to display morphological changes in the form of several roundish shallow features that grew and merged over the following months (Groussin et al. 2015b). For brevity, we occasionally use the more informal ‘pits’ for such shallow depressions. The escarpments that constituted the rims of these pits had heights on the order of one metre and moved with speeds at 0.2–0.3 m h⁻¹ (Groussin et al. 2015b). The largest single feature grew to a diameter of 220 m, and these morphological changes eventually affected 40 per cent of the surface area of the Imhotep smooth terrain (Groussin et al. 2015b). Similar phenomena were later observed in several smooth terrains on different parts of the comet (El-Maarry et al. 2017; Hu et al. 2017; Birch et al. 2019; Bouquety et al. 2022).

* E-mail: Bjorn.Davidsson@jpl.nasa.gov

Thus far, the characterization of expanding pits and moving escarpments has relied exclusively on visual images and spectrophotometry. This provides snapshots of the pit morphology that can be used to establish a time-line of how the pit size and shape evolved, and it places some constraints on composition. However, this information is not sufficient in order to understand why the pits form or what mechanisms are responsible for their evolution. We also do not know the physical properties of the near-surface material (such as temperature, porosity, and thermal inertia), and we do not know which volatiles are present, at what depths they are encountered, or what vapour pressures they are capable of reaching. Furthermore, it is necessary to know the thermal history of the location in question. This requires calculating the amount of energy that is available at any given moment to drive changes, and to understand the previous evolution that has led up to the current conditions. Only with such detailed information available it is possible to develop a pit formation and evolution scenario that is quantitative and not merely qualitative, that is physically realistic and consistent with observational data, and that explains why the phenomenon starts and ends at given points in time. We here take the first step of expanding the database of physical and chemical properties at pit formation sites by using observations made by *Rosetta*/MIRO (Microwave Instrument for *Rosetta* Orbiter; Gulkis et al. 2007), and apply the state-of-the-art comet nucleus thermophysics model NIMBUS (Numerical Icy Minor Body evolUtion Simulator; Davidsson 2021) in order to analyse the MIRO data and to provide the contextual information necessary to develop a quantitative understanding of the pit formation phenomenon.

This work is important because we still have a poor understanding of comet activity (a post-*Rosetta* analysis of the state of affairs is made by Keller & Kührt 2020). Pit growth is one of the most dramatic expressions of comet activity observed by *Rosetta*. Reaching an understanding of how and why these pits form and grow is therefore needed in order to better understand comet activity itself. One of the four main measurement goals of the *Rosetta* mission was ‘Study of the development of cometary activity and the processes in the surface layer of the nucleus and inner coma (dust/gas interaction)’ (Schwehm & Schulz 1999). If the problem of pit growth could be solved, substantial progress could be made to understand comet activity and fulfil a key *Rosetta* science goal.

As stated previously, Imhotep was not the only smooth terrain in which pits were formed. In this paper, we focus on one particular set of shallow pits in the Hapi region, that formed around 2014 December 31 and grew until growth stopped sometime between 2015 February 28 and March 17. Hapi is a smooth terrain located on the Northern hemisphere on the neck between the two lobes of the comet (Sierks et al. 2015). Its properties have been described in detail by Pajola et al. (2019). We use a sequence of OSIRIS images to reconstruct the temporal evolution of the depressions, as well as OSIRIS spectrophotometry to obtain constraints on the composition of the material within, and around, the pits. We use observations by MIRO acquired in October and November 2014, that provides the thermal emission of the surface material during the months leading up to pit formation. A combination of thermophysical and radiative transfer models are employed in order to analyse the MIRO microwave data and to place constraints on the thermal inertia, diffusivity, chemical composition, stratification, extinction coefficients, and scattering properties of the near-surface material. From this analysis, we infer that significant changes in chemical stratification and physical properties took place prior to pit formation. We use thermophysical models of the nucleus from the May 2012 aphelion to mid-March 2015 to place our findings into a broader context. This allows us to place important constraints on

the properties of airfall material (by demonstrating the presence of a solid-state greenhouse effect), and on the mechanism responsible for morphological changes in smooth terrain (by demonstrating that the MIRO observations and the timing of pit formation are consistent with CO₂-driven activity). Furthermore, we demonstrate that such activity may be responsible for the observed near-surface compaction of cometary material, and ultimately for the formation of consolidated terrain.

Section 2 describes the observational data, specifically, OSIRIS images and spectrophotometry in Section 2.1, and MIRO data in Section 2.2. Section 3 summarizes our models: illumination conditions (Section 3.1); a relatively simple (Section 3.2) and a relatively advanced (Section 3.3) nucleus thermophysical model; and a radiative transfer model (Section 3.4). Our results are described in Section 4, focusing on the MIRO October 2014 data (Section 4.1), the MIRO November 2014 data (Section 4.2), and the contextual simulations (Section 4.3). These results are discussed in Section 5 and our conclusions are summarized in Section 6.

2 OBSERVATIONAL DATA

2.1 OSIRIS observations

2.1.1 OSIRIS imaging

The images shown in this section (Sierks et al. 2020) are available on the ESA Planetary Science Archive (PSA¹), as well as on the NASA Planetary Data System (PDS²). Fig. 1 (upper left-hand panel), shows Hapi and its surroundings – Seth on the large lobe to the left, and the steep Hathor cliff of the small lobe to the right. Fig. 1 (upper right-hand panel), shows a 213 × 213 m part of Hapi, at a location marked by a square in the upper left-hand panel. Here, Hapi is dominated by material with a particle size smaller than the 0.35 m px⁻¹ spatial resolution, forming a rather flat plain. The plain is covered with boulders with sizes ranging from the resolution limit to several tens of meters. Three boulders have been labelled for reference purposes (B1–B3). Note the ridge above B3, running parallel to the B1–B2 line.

Fig. 1 (upper right-hand panel), was acquired on 2014 December 10, prior to any detectable change. The first-known indications of changes are from 2014 December 30, where Fig. 1 (lower left-hand panel) shows two crescent-shaped dark features between boulders B1 and B2. The two features, indicated by the arrows, are 4.9 ± 0.5 and 7.7 ± 0.5 m across, respectively. During the following 12.10 d (Fig. 1, lower right-hand panel), the features grew in size to 12.9 ± 2.6 and 13.1 ± 2.6 m. If assuming circular expansion, that corresponds to average radial propagation velocities of 0.33 ± 0.13 m d⁻¹ (13.7 ± 5.4 mm h⁻¹) and 0.22 ± 0.13 m d⁻¹ (9.4 ± 5.4 mm h⁻¹).

The upper left-hand panel image in Fig. 2 was taken on 2015 January 22, or 11.40 d after the lower right-hand panel image in Fig. 1. The two features have now merged into a single shallow depression located between boulders B2 and B3, and a new feature has appeared to the left of boulder B2. The large depression to the right has a length of ~ 63 m and a width of ~ 22 m. The escarpment is located 30.9 m from B2 in the direction towards B3, and is 42.6 m from B3 along the same line. The features appeared near the line between B1 and B2, thus the escarpment has moved about 22 m

¹<https://www.cosmos.esa.int/web/psa/rosetta>

²https://pds-smallbodies.astro.umd.edu/data_sb/missions/rosetta/index.shtml

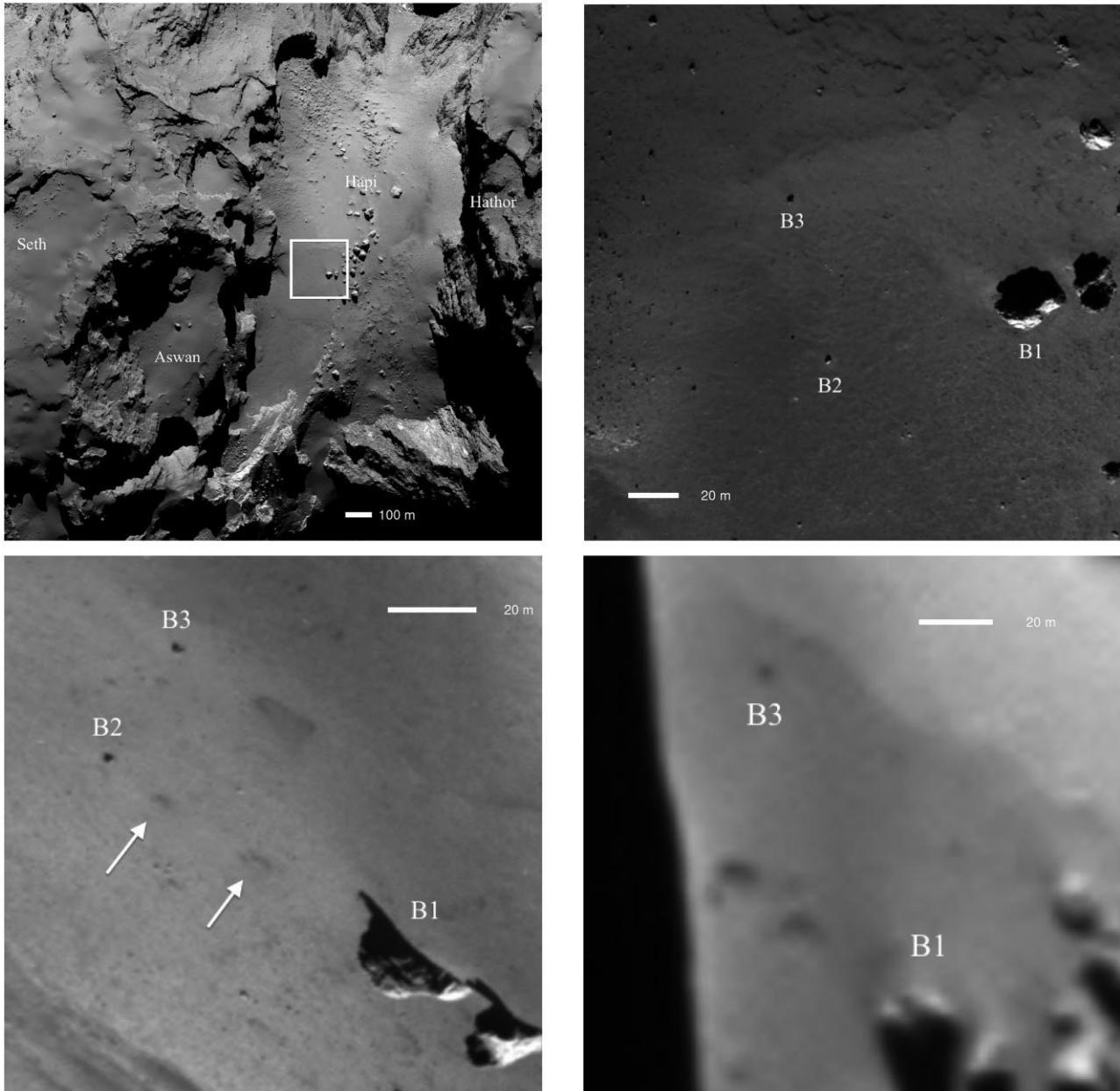


Figure 1. Upper left-hand panel: NAC context image of Hapi and surroundings taken on 2014 August 30. The large lobe is to the left and the small lobe is to the right (outside the image). The distance from *Rosetta* to the comet surface was approximately 55.5 km and the resolution was 0.98 m px^{-1} . The square marks the area in which the currently discussed changes took place, and is the approximate field of view in the upper right panel. Image MTP006/n20140830t034253546id20f22.img. Upper right-hand panel: This NAC image of a small portion of the Hapi region was acquired on 2014 December 10, prior to any detectable change (see the upper left-hand panel for context). The distance from *Rosetta* to the comet surface was $\sim 19.9 \text{ km}$ and the resolution was 0.35 m px^{-1} . The boulder B1 measures $27.4 \pm 0.4 \text{ m}$ across. Boulders B2 and B3 are $1.8 \pm 0.4 \text{ m}$ and $2.1 \pm 0.4 \text{ m}$ across, respectively, and the projected distance between the two is $65.5 \pm 0.4 \text{ m}$. Image MTP010/n20141210t062855791id20f22.img. Lower left-hand panel: This NAC image, taken on 2014 December 30, shows the first-known indications of changes (two dark features marked with arrows). The distance from *Rosetta* to the comet surface was approximately 27.8 km and the resolution was 0.49 m px^{-1} . The surface is seen at a high emergence angle that distorts the perspective. The left feature is $4.9 \pm 0.5 \text{ m}$ across, and the right feature is $7.7 \pm 0.5 \text{ m}$ across. Image MTP011/n20141230t081300834id20f22.img. Lower right-hand panel: This WAC image was taken on 2015 January 11. The distance from *Rosetta* to the comet surface was approximately 27.1 km and the resolution was 2.57 m px^{-1} . The features have grown with respect to the lower left-hand panel. The left feature is $12.9 \pm 2.6 \text{ m}$ across, and the right feature is $13.1 \pm 2.6 \text{ m}$ across. Image MTP011/w20150111t125858091id20f13.img.

in 23.5 d, yielding an average propagation speed of approximately 0.9 m d^{-1} . About 28 m right of B2 there is a rim with a slope facing right, and $\sim 27 \text{ m}$ farther away is a second rim with a slope facing left. If this quasi-circular structure is interpreted as the expanded 13.1 m feature in Fig. 1 (lower right-hand panel), those rims propagated with a speed of about 0.6 m d^{-1} . These speeds are 2–4 times higher than

those measured for the period 2014 December 30 to 2015 January 11, suggesting that the propagation speed may have accelerated.

At the time the image in Fig. 2 (upper left-hand panel) was taken, the solar incidence angle was $\sim 68^\circ$ (for facet F#1, see Section 3.1). Because the horizontally oriented rims in that image cast shadows into the depressions, we can infer that the rims have slopes steeper

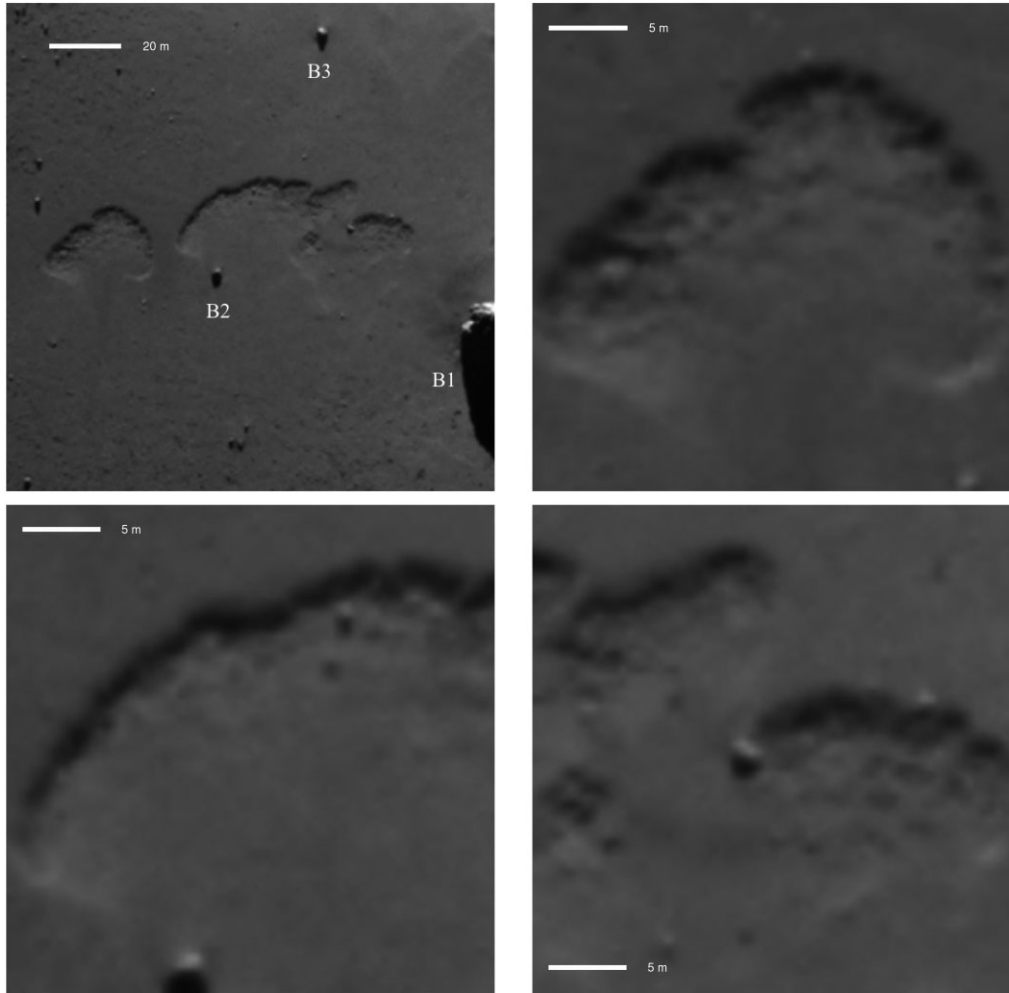


Figure 2. Upper left-hand panel: This is a portion of a NAC image taken on 2015 January 22, and shows two shallow and flat-bottomed depressions that were not present six weeks earlier (Fig. 1). The distance from *Rosetta* to the comet surface was an approximately 27.3 km and the resolution was 0.49 m px^{-1} . The projected distance between boulders B1 and B2 is $73.1 \pm 0.4 \text{ m}$. Image MTP012/n20150122t223400384id20f22.img. Upper right: Close-up of the left feature in the upper left-hand panel, on 2015 January 22. Lower left-hand panel: Close-up of the left rim of the right feature in the upper left-hand panel, on 2015 January 22. Lower right-hand panel: Close-up of the right rim of the right feature in the upper left-hand panel, on 2015 January 22.

than $\sim 68^\circ$. Based on the length of these shadows being 1–2 m, the depth of the depressions can be estimated as $0.5 \pm 0.1 \text{ m}$.

The isolated depression to the left is roughly triangular in shape with dimensions $\sim 29 \text{ m}$ by $\sim 20 \text{ m}$. The surface area is an approximately 290 m^2 , and the volume affected by the change is about 140 m^3 , corresponding to nearly 80 metric tons of material if assuming that the density is identical to the nucleus bulk density $\rho_{\text{bulk}} = 535 \text{ kg m}^{-3}$ (Preusker et al. 2015; Jorda et al. 2016).

The lower rim is diffuse and featureless. The rest of the rim, seen magnified in Fig. 2 (upper right-hand panel), is continuous and seems to consist of a number of weakly curved segments, each being a few meters in size. If mass wasting takes place at the steep rims, this material is too small to be resolved. Compared to the immediate surroundings, the bottom of the depression has a larger degree of resolved roughness, at least in the upper half of the depression.

The left half of the large depression to the right in Fig. 2 (upper left-hand panel), is seen magnified in Fig. 2 (lower left-hand panel). An $\sim 5 \text{ m}$ wide region, tracing the curved escarpment, appears rougher at resolved size scales than the material below. The smoother material may form a tongue-shaped feature (just right of B2 in Fig. 2, upper left-hand panel, though the contrast is poor.

Fig. 2 (lower right-hand panel) is a close-up of the right part of the right depression in Fig. 2 (upper left-hand panel). The rim lacks shadows in two places, suggesting that the slope locally is less than $\sim 68^\circ$. Just below the rim, the floor of the depression is hummocky in appearance, with a half-dozen relatively bright structures visible. Just right of the central boulder in Fig. 2 (lower right-hand panel), a number of concavities and hills are seen on the floor of the depression.

The upper left-hand panel image in Fig. 3 taken on 2015 February 5, or 13.12 d after the upper left-hand panel image in Fig. 2, shows that the two depressions have merged, having a common escarpment. The width of the bridge between the depressions in Fig. 2 (upper left-hand panel) was 7.4 m, suggesting a propagation velocity of $\geq 0.28 \text{ m d}^{-1}$ if both depressions grew at similar speeds. The width of the depression, as measured from the B1–B2 line towards the escarpment near B2, varies between 30–45 m, suggesting an average propagation velocity of $0.8\text{--}1.2 \text{ m d}^{-1}$ for the escarpment. The distance between boulders B2 and B3 is $75.1 \pm 2.1 \text{ m}$ in the image plane. Since 2015 January 22, the distance from the escarpment to boulder B3 decreased from ~ 43 to $\sim 21 \text{ m}$, suggesting a propagation velocity of $\sim 1.7 \text{ m d}^{-1}$. Considering that the propagation speed from

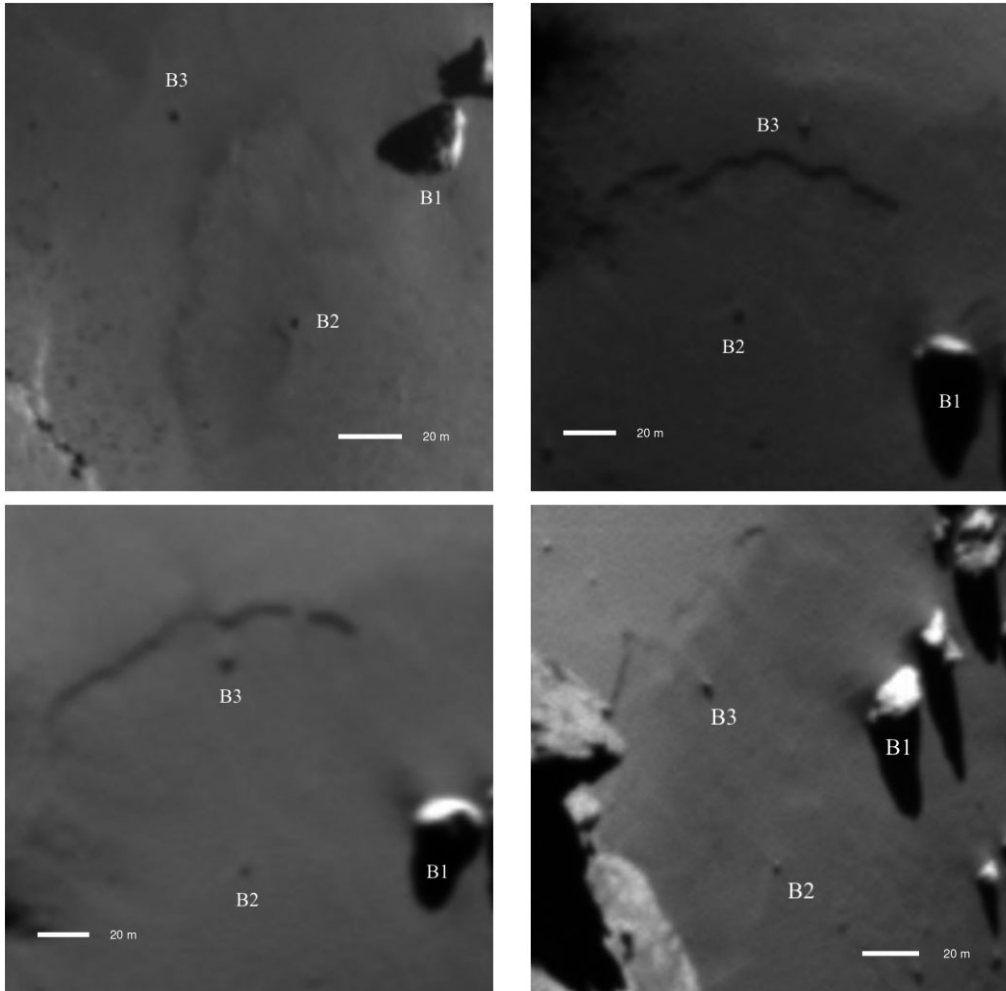


Figure 3. Upper left-hand panel: On 2015 February 5, the two depressions have merged into a single one. The distance from *Rosetta* to the comet surface was approximately 58.9 km and the resolution was 1.05 m px^{-1} . Image MTP012/n20150205t013716672id20f41.img. Upper right-hand panel: This NAC image was taken on 2015 February 9. The distance from *Rosetta* to the comet surface was approximately 106.1 km and the resolution was 1.89 m px^{-1} . MTP012/n20150209t123142699id20f22.img. Lower left-hand panel: This NAC image was taken on 2015 February 28. The distance from *Rosetta* to the comet surface was approximately 108.3 km and the resolution was 1.93 m px^{-1} . Image MTP013/n20150228t044349351id20f22.img. Lower right-hand panel: This NAC image was taken on 2015 March 17. The distance from *Rosetta* to the comet surface was approximately 77.2 km and the resolution was 1.37 m px^{-1} . Image MTP014/n20150317t061250371id20f22.img.

Fig. 1 (lower right-hand panel) to Fig. 2 (upper left-hand panel) was estimated as 0.9 m d^{-1} , again suggests acceleration. At this stage, the full length of the depression was $\sim 140 \text{ m}$.

Fig. 3 (upper right-hand panel) was taken on 2015 February 9, 4.45 d after Fig. 3 (upper left-hand panel). The escarpment is now $13 \pm 4 \text{ m}$ from B3, suggesting a propagation speed of $1.8 \pm 0.9 \text{ m d}^{-1}$, which is similar to the speed during the previous two weeks. The irregular shape of the escarpment suggests that there are some differences in propagation speed in different places. Although the resolution is comparatively poor, there is some indication of a rougher region just behind the escarpment, compared to much earlier locations.

The next image of this region was taken 23.13 d after Fig. 3 (upper right-hand panel) on 2015 February 28. As seen in Fig. 3 (lower left-hand panel), the escarpment passed underneath boulder B3, and continued $\sim 15 \text{ m}$ beyond it. The projected distance between B2 and B3 is $\sim 83 \text{ m}$. The distance from boulder B2 to the escarpment increased by $\sim 34 \text{ m}$ with respect to Fig. 3 (upper right-hand panel), implying an escarpment propagation velocity of $\sim 1.5 \text{ m d}^{-1}$. This

is similar to the speed measured since 2015 January 22, implying quasi-constant progression for about a month.

The last image of this region before perihelion with $\sim 1 \text{ m px}^{-1}$ resolution was taken on 2015 March 17, and is shown in Fig. 3 (lower right-hand panel). During these 17.06 d, the escarpment moved very little, suggesting that it came to a halt at the beginning of March. The total size of the region affected by this phenomenon is about 100 m wide and about 140 m long. For simplicity, this region is hereafter referred to as ‘Hapi D’ (D for depression). Thus, a total area of $\sim 14000 \text{ m}^2$ was crossed by the escarpment, and considering the 0.5-m depth, the volume affected was $\sim 7000 \text{ m}^3$. This corresponds to ~ 3700 metric tons of mass.

2.1.2 OSIRIS spectrophotometry

Multispectral analysis of Hapi, together with other active areas, shows sub-units within the region (Oklay et al. 2016b). While the region was interpreted as covered with well-mixed icy and non-icy materials, Hapi D is known to have had lower spectral slopes

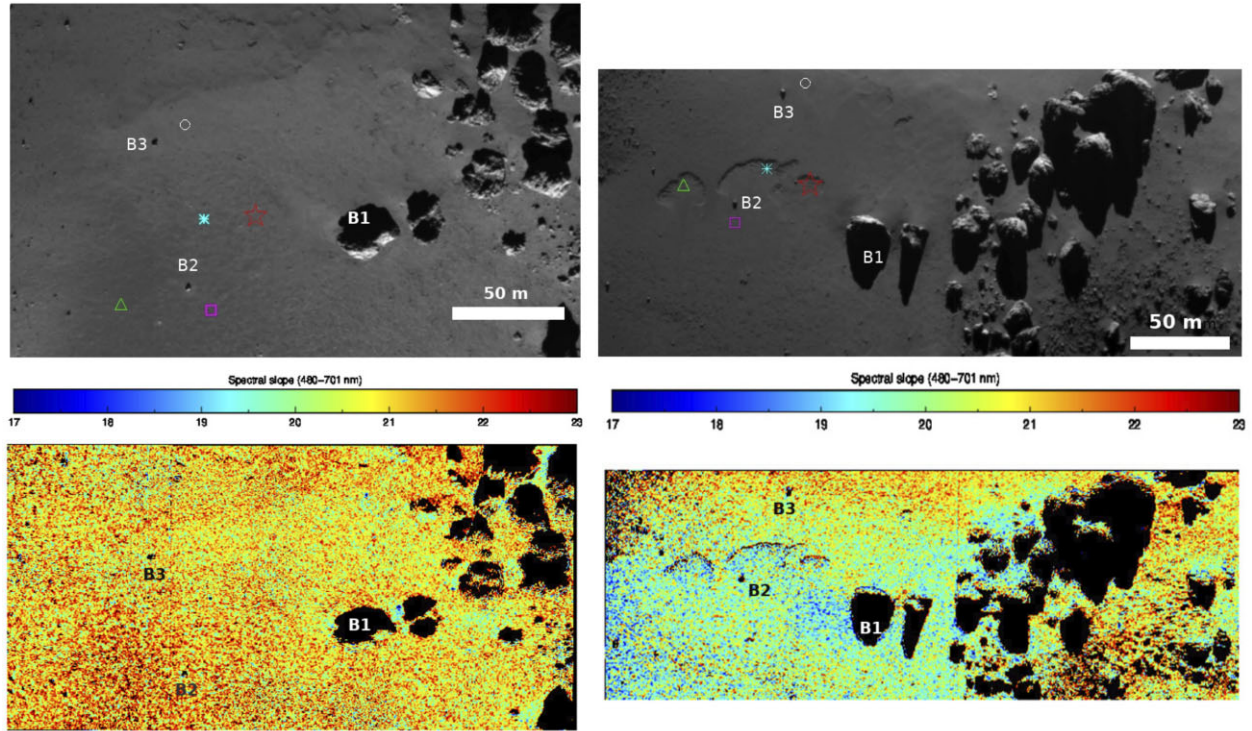


Figure 4. Images and associated spectral slope S map, evaluated in the 480–701-nm range and normalized at 480 nm, for data acquired on 2014 December 10 (left-hand panel; MTP010/n20141210t062911447id4bf24.img and MTP010/n20141210t062919757id4bf27.img) and on 2015 January 22 (right-hand panel; MTP012/n20150122t223416529id4bf24.img and MTP012/n20150122t223425034id4bf27.img). In both figures the symbols represent ROIs near and inside the pits, before and after their formation, for which we tabulate S in Table 1.

than the areas beyond (towards B3 in Fig. 2, upper left-hand panel) and compared to the large boulders (towards Hathor in Fig. 1, upper left-hand panel). The high-resolution views of Hapi D on 2014 December 10 (Fig. 1, upper right-hand panels) acquired before visible changes, and that on 2015 January 22 (Fig. 2, upper left-hand panels) obtained when pit formation was well underway, are available in different camera filters. Specifically, the filters F24 (480.7 nm), F23 (535.7 nm), F22 (649.2 nm), and F27 (701.2 nm), are common to the two dates. This allows for the detection of potential exposures of volatiles at the surface (Pommerol et al. 2015; Oklay et al. 2016a, 2016b; Fornasier et al. 2016), as well as spatial and temporal variability in ice abundance. We calculated the spectral slope for the two filters with the largest wavelength difference,

$$S = \frac{(R_{701.2} - R_{480.7}) \times 10^4}{(701.2 - 480.7)R_{480.7}}. \quad (1)$$

Here, S is in units per cent $(100 \text{ nm})^{-1}$ and R is the radiance factor at the indicated wavelengths (i.e. the observed radiance in units $\text{W m}^{-2} \text{ster}^{-1} \text{nm}^{-1}$ divided by $F_{\lambda}/(r_h^2\pi)$, where r_h is the heliocentric distance and F_{λ} with units $\text{W m}^{-2} \text{nm}^{-1}$ is the monochromatic solar irradiance at the central wavelength of the filter at 1 au). These radiance factor images are produced using the OSIRIS standard pipeline, including corrections for geometric distortions, following the reduction steps described in Tubiana et al. (2015) and Fornasier et al. (2015, 2019). The two data sets were acquired at high and very similar phase angles (92° on 2014 December 10, and 93° on 2015 January 22), thus the phase reddening effect, observed on Comet 67P (Fornasier et al. 2015, 2016) should be negligible.

The reliable determination of the subtle variations in spectral slope is delicate, and the results are susceptible to artefacts. To assess the reliability of the results, two independent groups analysed

the data with two different methods. In the first approach, the sequences were coregistered using the F22 NAC filter as reference with dedicated python scripts (Fornasier et al. 2019). To improve the quality of the coregistration to sub-pixel level, the full images were cropped and we coregistered only the region of interest around the pit location. Considering that the shape model does not take into account the morphological surface changes, we did not apply a Lommel–Seeliger disc function correction, as normally done for the 67P spectrophotometry (Fornasier et al. 2017), in order to avoid biases in the illumination corrections. However, considering that S is normalized at a given wavelength (480.7 nm), this should not be an issue, because the same disc function appears at the numerator and denominator of equation (1), and thus any normalization applied would cancel out. The slope S obtained with the first method is shown in Fig. 4.

A comparison of the spectral slope at Hapi D before and during the appearance of pits reveals some local colour changes. Globally, for the area shown in Fig. 4, the spectral slope decreases from 21.0 per cent $(100 \text{ nm})^{-1}$ to 20.2 per cent $(100 \text{ nm})^{-1}$. A substantial fraction of the region, including the pits, is spectrally bluer in January 2015 compared to December 2014. This cannot be explained by phase reddening effects, but points to a local removal of dust caused by the cometary activity. In fact, seasonal spectral slope variations have been reported for 67P, with progressively bluer colours as the level of activity increases when approaching perihelion (Fornasier et al. 2016, 2017). This seasonal variation in colours has been attributed to the progressive thinning of the dust-coating with increasing activity, with relatively bluer colour and thus smaller spectral slope values associated to the exposure of the underlying layers richer in volatiles. Simultaneous VIRTIS and OSIRIS observations have indeed confirmed that a smaller spectral slope in the visible

Table 1. Spectral slope S , computed in the 480–701-nm wavelength range and normalized at 480 nm, for the five ROIs selected around and inside the pits (see Fig. 4), selected at the same position in the images acquired before (December 2014) and during (January 2015) their formation.

ROI	Spectral slope S [% (100 nm) ⁻¹] December 2014	Spectral slope S [% (100 nm) ⁻¹] January 2015
Circle	21.2 ± 0.2	21.2 ± 0.2
Red star	21.7 ± 0.2	20.7 ± 0.3
Cyan asterisk	21.5 ± 0.2	19.8 ± 0.2
Green triangle	21.5 ± 0.2	19.0 ± 0.2
Magenta square	21.3 ± 0.3	19.7 ± 0.2

range is associated with absorption bands in the near-infrared region due to H₂O or CO₂ ice (Barucci et al. 2016; Filacchione et al. 2016; Deshapriya et al. 2016). Similar correlations are seen in Comets 9P/Tempel 1 and 103P/Hartley 2 (Oklay et al. 2016a).

We also investigated the spectral slope in specific Regions Of Interest or ROI (measuring 3 × 3 pixels and shown in Fig. 4) at the floor of the pits and surroundings before and during their formation. The S values for the ROIs are reported in Table. 1. We notice that the floor of the pits, represented by the red star, cyan asterisk, and green triangle, are spectrally less red than surroundings in January 2015 data, notably compared to the ROI represented by the circle that appears unchanged both in morphology and colours in the two selected data sets. The spectral slope inside the pits decreased by about $\Delta S = 1.0$ – 1.7 per cent (100 nm)⁻¹ from 2014 December 10 to 2015 January 22, or a relative 7 per cent change in only 40 d, compared to the 1 per cent error bars on spectral slope. The slope at the magenta square becomes smaller despite not being located within a pit, suggesting that resurfacing may take place without resulting in detectable morphological changes. This is an important point, that we will return to in Section 2.2.3.

The 2015 January 22 data were also analysed using a second, alternative, approach. Here, the images taken with different filters were coregistered to a reference image (F23 at 535.7 nm) in sub-pixel accuracy using Integrated Software for Imagers and Spectrometers (USGS ISIS3 software,³ Anderson et al. 2004). In this way, the colour artefacts introduced due to rotation of the comet and the motion of the spacecraft are eliminated. Every step of this procedure can be found in Oklay et al. (2016b). The spectral slope S was calculated according to equation (1) and is shown in Fig. 5. The two methods give consistent results – the depressions are spectrally different from their surroundings. In the close vicinity of the depressions in the direction of B1 and B2 there are small areas with mean spectral slopes of 17.60 per cent (100 nm)⁻¹, which is lower than their surrounding with a value of 20.25 per cent (100 nm)⁻¹.

Similar feature formation associated with sub-surface water-ice exposures were observed later in various places on the comet including the Hapi region (Birch et al. 2019). While the spectral slope definition in the scarps study of Birch et al. (2019) is slightly different than ours (the F41 filter at 882.1 nm was used instead of the F27 filter at 701.2 nm), both studies find about 2 per cent (100 nm)⁻¹ lower spectral slopes in the areas close to the depressions. The escarpments in the Imhotep region reported in Groussin et al. (2015a) are different from those in Hapi. The Imhotep escarpments contained bright material that had almost neutral spectra, indicating those were

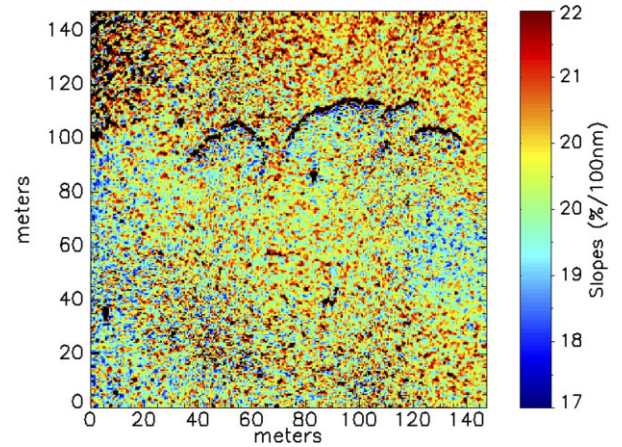


Figure 5. Spectral slope S map, calculated in an alternative way than was used in Fig. 4 (see text), evaluated in the 480–701-nm range and normalized at 480 nm. The spectral slopes in the close vicinity of the depressions are about 2 per cent (100 nm)⁻¹ lower than the average of their surroundings. Images MTP012/n20150122T223416529id4bf24.img and MTP012/n20150122T223425034id4bf27.img.

rich in water ice. While the Hapi depressions expose local small areas of bright and presumably water-ice-rich material, those are not as prominent as seen in the escarpments described by Groussin et al. (2015a). In conclusion, the pit formation in Hapi D exposed material that was somewhat richer in ice than the undisturbed surface, but not by much. At the time of pit formation, the top ~ 0.5 m appears to have been already largely devolatilized.

2.2 MIRO observations

Observations by MIRO have previously been analysed and discussed by, for example, Choukroun et al. (2015), Gulkis et al. (2015), Lee et al. (2015), Schloerb et al. (2015), Marshall et al. (2018), Biver et al. (2019), and Rezac et al. (2019, 2021). We here consider thermal emission from 67P observed by MIRO in two broad-band continuum channels centred at the wavelengths $\lambda = 0.533$ mm and 1.594 mm (Gulkis et al. 2007; Schloerb et al. 2015), referred to as the sub-millimetre (SMM) and millimetre (MM) channels, respectively. The measured antenna temperatures have been averaged over 1 s intervals and stored at NASA’s Planetary Data System (PDS) with a wealth of ancillary information, including the time of observation and the Cheops-system spherical coordinates (Preusker et al. 2015) of the interception point of the SMM and MM beam centres with the nucleus surface (Hofstadter et al. 2019). Time is measured in ‘day numbers’ with $d_n = 1$ occurring 2014 January 1 at 00 : 00 UTC and incremented by unity every 24 h.

The archived antenna temperatures T''_{SMM} and T''_{MM} need to be corrected for two instrumental effects, in order to obtain values relevant for the main beams: spillover and beam efficiency (Frerking et al. 2020). Spillover refers to losses due to incomplete interception of radiated power at the optical components, and is 1.5 per cent at the secondary mirror and 2.5 per cent at the primary mirror, amounting to a total of 4 per cent in both channels. Spillover-corrected antenna temperatures are therefore $T'_{\text{SMM}} = T''_{\text{SMM}}/0.96$ and $T'_{\text{MM}} = T''_{\text{MM}}/0.96$. Beam efficiency refers to additional losses caused by μm -scale roughness on optical surfaces and optics misalignment (coma effects). By integrating over the laboratory-measured beam patterns out to 100 arcmin (far beyond the main beams with full width at half-maximum, FWHM, of 7.5 arcmin

³<http://isis.astrogeology.usgs.gov/index.html>

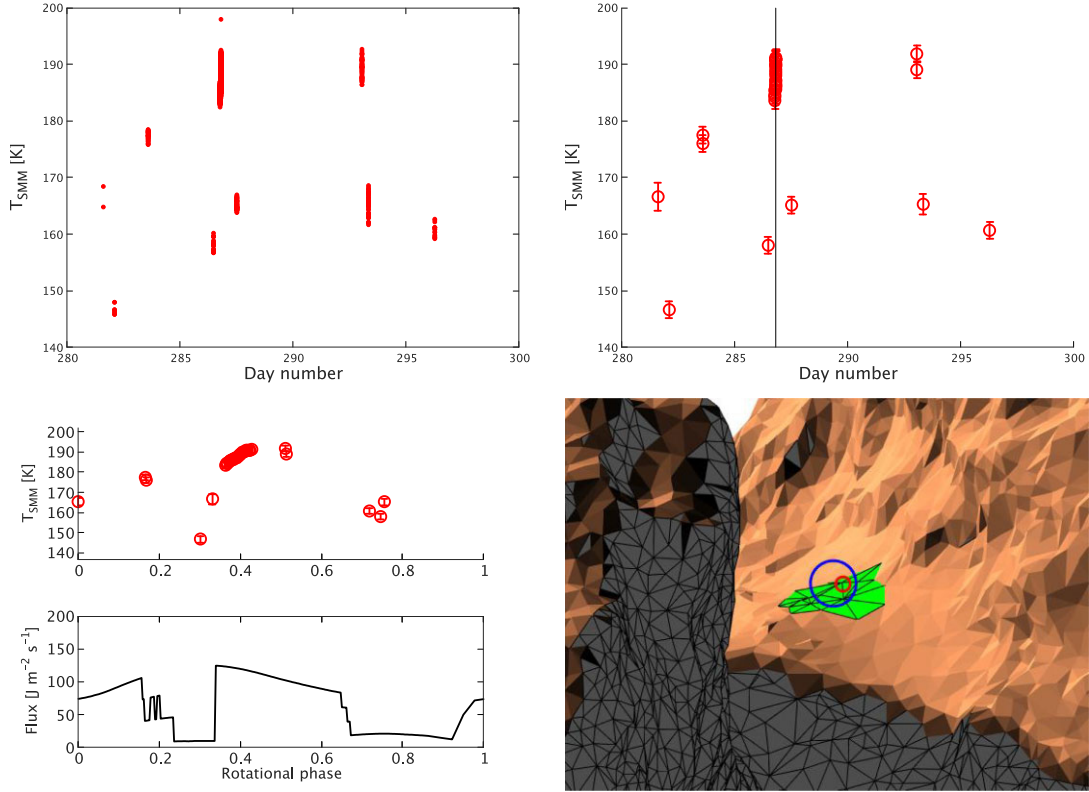


Figure 6. Upper left-hand panel: Raw SMM 1-s continuum MRO antenna temperature observations of Hapi D in October 2014, on the original time-line, assuming a beam efficiency (see text) of $B_e = 0.96$. Upper right-hand panel: Binning the SMM data into 2.4 min-wide bins (error bars show the standard deviation for the data within a given bin), on the original time-line. Middle left-hand panel: The binned SMM data are here time-shifted to a common master period. Lower left-hand panel: The time-shifted data are here compared to the flux (direct solar illumination plus infrared self-heating) as described in Section 3.1. Lower right-hand panel: The nucleus of 67P as seen from the *Rosetta* spacecraft on 2014 October 13, at 19 : 21 UTC, during the continuous stare. The intensity of the copper colour scales with the local solar flux, grey areas are in shadow, the green field shows Hapi D, and the red (SMM) and blue (MM) rings are the MRO FWHM beam footprints.

at SMM and 23.8 arcmin at MM; Schloerb et al. 2015), the beam efficiency is found to be nearly complete at MM, but $B_e = 0.96 \pm 0.02$ at SMM. Therefore, we apply finally calibrated antenna temperatures $T_{MM} = T'_{MM}$ and $T_{SMM} = T'_{SMM}/B_e$. We nominally use $B_e = 0.96$, but occasionally apply other values in the $0.94 \leq B_e \leq 0.98$ range (sometimes $B_e = 1$ for comparison), as indicated in the text. When the nucleus is close enough to enter the antenna side lobes (at 1° – 6° from the beam centre, or at $\lesssim 20$ – 100 km from the nucleus), small reductions of T_{MM} and T_{SMM} take place because of the extra peripheral signal, that slightly counter the effect of spillover and beam efficiency. We estimate that these are sufficiently small to be absorbed by the uncertainties assigned to the antenna temperatures and B_e . Calibrated antenna temperatures are here generically referred to as T_A if we do not need to distinguish SMM and MM.

The archive was searched for suitable observations as follows. The 3.1×10^6 -facet SHAP5 version 1.5 shape model of 67P (Jorda et al. 2016) was read into the MESHLAB⁴ tool that allows the user to visualize the geometry of the nucleus. The region corresponding to the 2015 March 17 extension of the depression (Fig. 3, lower right-hand panel) was identified visually and marked using the Z-painting tool of MESHLAB. Searching the shape model data files for marked facets showed that the region is located between longitudes 6° – 44° E, latitudes 44° – 71° N, at a distance 0.53–0.58 km from

the nucleus core. The MRO data base was searched for entries having simultaneous SMM and MM observations with beam centres within the specified longitude, latitude, and radial ranges, excluding observations at emergence angles $e \geq 80^\circ$. This was done for October and November 2014, the months prior to the onset of surface changes when *Rosetta* was closest to the nucleus.

We first discuss the retrieved observations for October (Section 2.2.1) and November (Section 2.2.2). We then discuss the spatial resolution of these observations in relation to the size of the area of interest (Section 2.2.3).

2.2.1 MRO observations in October 2014

For October 2014, a total of 2712 observations were found, as shown in the upper left-hand panel of Fig. 6. All occurred during the 15-d period between October 8–23. Ideally, the region should have been observed continuously during a nucleus revolution to allow for a comparison between calculated and observed diurnal temperature variations. However, the longest continuous stare lasted 48 min, and the other data points were acquired when the MRO beams passed Hapi D briefly and serendipitously during scanning. The dispersions of antenna temperature during these crossings are roughly 2–8 K, exemplifying the sensitivity to the exact pointing in this region. An empirical diurnal temperature curve was created by sampling the available data in 2.4 min-wide bins (upper right-hand panel of Fig. 6),

⁴Visual Computing Lab – ISTI – CNR, <http://meshlab.sourceforge.net/>

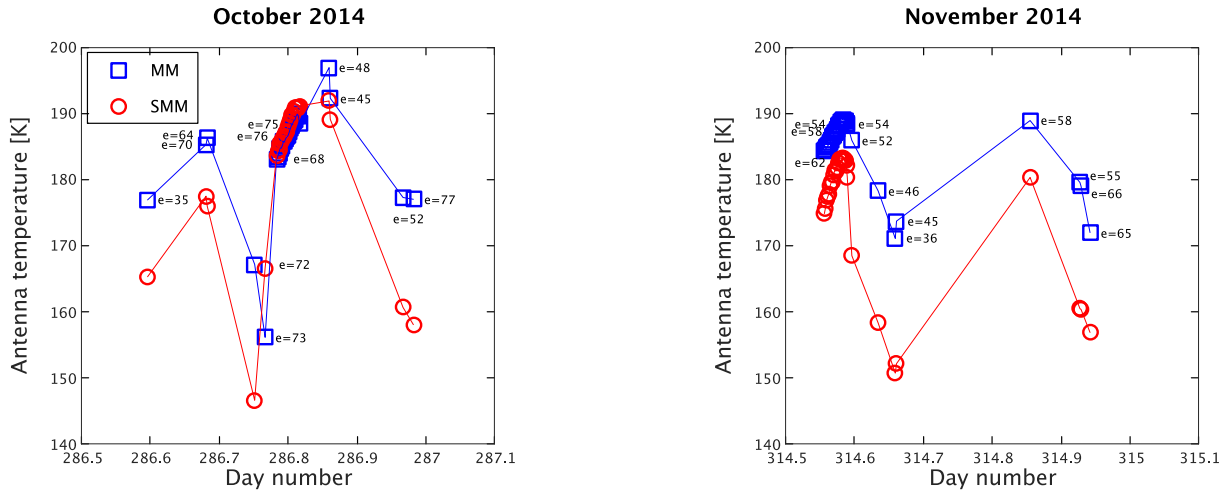


Figure 7. The MM and SMM (with $B_c = 0.96$) binned 1-s continuum antenna temperatures, shifted to the October 2014 (left-hand panel) and November 2014 (right-hand panel) master periods. Both panels show the beam centre emergence angle e at the time of observation.

roughly corresponding to a nucleus angular rotation of 1° , and time-shifting those bins on to a common nucleus master period starting 2014 October 13 at 14 : 18 : 12 UTC ($d_n = 286.596$). The error bars of the bins are the standard deviation of the temperatures within each bin, ranging between 1.5–2.4 K. These are larger than the ~ 1 K absolute calibration error of each data point (Schloerb et al. 2015), reflecting the fact that each bin consists of numerous data points with some temperature dispersion. It was decided to apply a flat ± 2.5 K error bar for the purpose of assessing goodness of fit with respect to synthetic temperature curve (Section 3.4.3). The temperature increase due to a reduced heliocentric distance during the period of observation is smaller than 2.5 K. The time-shifted curve, consisting of 31 bins, is shown in the middle left-hand panel of Fig. 6, above the calculated illumination conditions at this location during the master period (see Section 3.1). The rise and fall of the antenna temperature with rotational phase correlates with changes of the incident flux, as expected. As a precaution, the observing geometry at the time of each bin was visualized as seen from *Rosetta*, including the illumination and shadowing conditions on the nucleus, as well as the location of Hapi D with respect to the MM and SMM FWHM beams (one example is shown in the lower right-hand panel of Fig. 6). If the beams intercept foreground or background terrain in addition to the region of interest (potentially having strong temperature differences), the corresponding bins would be removed for both MM and SMM. A single bin had to be removed, situated at the very end of the time-shifted curve. At the time of observation, Hapi D was in darkness and observed just above the fully illuminated small lobe in the foreground that intercepted parts of the beams. The antenna temperature of the deleted bin is some ~ 10 K warmer than other observations acquired at similar rotational phases, consistent with the suspicion that the warm small lobe is influencing the measurements.

2.2.2 MIRO observations in November 2014

A similar 1-s continuum data base search for November 2014 resulted in 4936 observations concentrated in a 20-d period between November 10–30. These data contained a 55 min stare at Hapi D plus several substantially shorter glimpses. These were binned and time-shifted to create a single diurnal temperature curve, using a master period starting on 2014 November 10 at 13 : 21 : 01 UTC ($d_n = 314.5563$). The temperature increase due to a reduced heliocentric

distance during the period of observation is smaller than the ± 2.5 K uncertainties. The curve consisted of 36 bins. However, four of those had to be removed. In one case, Hapi D was in darkness and both MIRO beams contained foreground terrain on the small lobe that was in full illumination. In the other three cases, Hapi D was illuminated but the MIRO MM beam contained foreground terrain on the large lobe that was in darkness. In all cases, the substantial temperature difference between interfering terrain and Hapi D caused significant anomalies that could not be tolerated.

Fig. 7 shows the MM and SMM antenna temperature curves plotted in the same diagram, with October and November shown side by side for comparison (using the nominal $B_c = 0.96$ for SMM). Two main differences between the October and November data sets are discernible. Both concern *the first peak and dip* of the curves. At these rotational phases, the maximum and minimum incident fluxes are ~ 100 and $\sim 10 \text{ J m}^{-2} \text{ s}^{-1}$, respectively, which is true for both months. Despite the similarity in illumination conditions it is seen that: (1) the MM amplitude is reduced from ~ 30 K in October to ~ 15 K in November, but no corresponding warmer change is seen at SMM; (2) the SMM first peak and dip are warmer by some 5–8 K in November compared to October, and the MM curve is somewhat warmer as well. These systematic changes from one month to the other, under similar illumination conditions, suggest a significant change in the physical conditions of the surface material between October and November.

2.2.3 MIRO beam footprint sizes

As stated previously, the Hapi D pits covered a region that measured $100 \text{ m} \times 140 \text{ m}$. Pit formation was associated with a reduction of the spectral slope, presumably because ice-free material was ejected, thus exposing material containing small amounts of water ice. However, Figs 4 and 5 show that similar spectral slope changes took place in a larger region extending for at least another 100 m below block B2. It is reasonable to assume that the mechanism that ejected dust at the pits also was active below Hapi D, albeit causing too subtle morphological changes to be easily recognized at the available resolution. The larger region that experienced spectral slope changes roughly coincides with the white square in the upper left-hand panel of Fig. 1, with approximate dimensions $200 \times 200 \text{ m}^2$. The green regions in Figs 6 (lower right-hand panel) and 8 show shape model

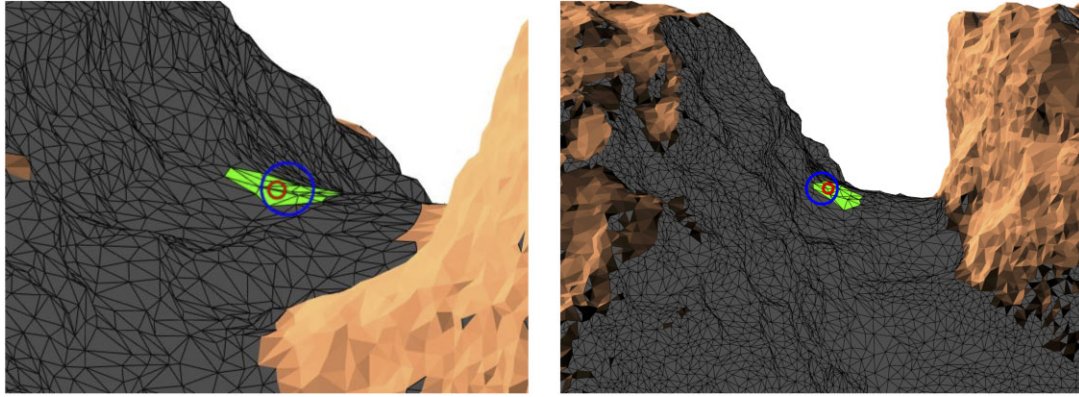


Figure 8. Left-hand panel: The viewing geometry on 2014 October 13, at 11:09 UTC, when the emergence angle was $e = 77^\circ$ and the MIRO beam footprints were the largest for the selected October observations: 37-by-171 m in the SMM (red) and 119-by-544 m in MM (blue), when projected on to the nucleus. Right-hand panel: The viewing geometry on 2014 November 18, at 04:15 UTC, when the emergence angle was $e = 65^\circ$ and the MIRO beam footprints were the largest for the selected November observations (71-by-166 m in the SMM and 226-by-527 m in MM). The SMM and MM FWHM footprints are shown as red and blue circles, respectively.

facets with centres located within Hapi D, but because the facets are rather large,⁵ they extend somewhat beyond and cover an area similar in size to the white square. MIRO receives radiation from an extended area of the nucleus, primarily from within the FWHM beams of 7.5 arcmin at SMM and 23.8 arcmin at MM (amounting to 76 per cent of the collected power). We here compare the sizes of these footprints with the area of interest.

When the October observations were acquired, *Rosetta* was 9.2–18.2 km from the nucleus centre. At such distances, the SMM footprint is 20–40 m across on perpendicular surfaces. Considering the spacecraft-Hapi D distances and the emergence angles at the time of observations, the long-axes of the resulting elliptic footprints are larger, 24–171 m, due to the cosine-effect. However, the short-axes are still 20–40 m. Note that 22 out of 30 bins have footprint long-axes smaller than 140 m (the largest extension of Hapi D). Observations were selected so that SMM and MM beam centres are placed within Hapi D, and visual inspection shows that the SMM FWHM falls entirely within the green field. This is exemplified by the red circle in Fig. 6 (lower right-hand panel), that projects as 35-by-123 m on the nucleus. The confinement to the green field is also illustrated by the largest 2014 October SMM footprint (37-by-171 m and corresponding to the last bin in Fig. 7, left, near $d_n = 287$), shown in Fig. 8 (left-hand panel). This bin is merely ~ 3 K cooler than the second last bin, at nearly the same rotational phase but having a much smaller 20-by-32 m footprint. This indicates that footprint size effects the antenna temperature rather little.

During the November observations, *Rosetta* was 29.6–41.7 km from the comet. The SMM footprints are then 65–91 m on perpendicular surfaces. The long-axes of the elliptic footprints during slanted observations ranged 79–166 m, but only three of 32 bins had footprints in excess of 140 m. The median long axis decreased from 129 m in October to 115 m in November, due to smaller e -values. The viewing geometry for the largest November 2014 SMM footprint (71-by-166 m and corresponding to the last bin in Fig. 7, right-hand panel, near $d_n = 314.95$) is shown in Fig. 8 (right-hand panel).

Clearly, the SMM beam is dominated by emission emanating from the pit-forming Hapi D region in both October and November, with

small contributions from the immediate surroundings. Judging from the similarity in spectral slope evolution, which suggests an enhanced capability of ejecting material to space, these surroundings likely had thermal properties comparable to those of Hapi D itself. It will therefore be assumed that the SMM observations sampled the special conditions that led to pit formation.

The situation is more complex at the MM wavelength, because of the ~ 3 times larger MM footprint, which made presence of undesirable terrain within the MM beam unavoidable. The green area typically fills 25–50 per cent of the MM FWHM, as illustrated by the blue circles in Figs 6 and 8. In case the physical properties of the top few centimetres of Hapi D surface material are drastically different from those of the surrounding smooth terrain, the dominating signal from the surroundings could distort signatures that are unique to Hapi D.

We approach this problem in two ways. First, we independently search for physical conditions (temperature and composition versus depth and time) that reproduce the observed antenna temperature, at both MM and SMM, for a given month. If those solutions are unique and turn out to be identical for MM and SMM, we consider this evidence of insignificant distortion of the MM signal. That investigation is presented in Section 4. Secondly, we investigate whether a substantial dislocation of the MIRO pointing results in a significant change of the measured antenna temperature. If this is not the case, then the thermophysical properties in the vicinity of Hapi D are similar to those in the pit forming area, and distortion effects should be small.

For this reason, a nearby region ~ 100 m to the north-west of Hapi D was selected, called ‘Hapi C’ (C for control unit). It consists of smooth terrain (seen in the lower half of the upper right-hand panel image of Fig. 1) that is visually indistinguishable from that of Hapi D. Because both terrains sit on a relatively flat portion of the nucleus their illumination conditions are similar. SMM data for Hapi C, located at longitudes 18° W– 27° E, latitudes 61° – 78° N, and 0.49–0.53 km from the nucleus centre, were binned and time-shifted to the same November 2014 master period as the Hapi D data. The Hapi C curve has only four bins. The two data sets overlap temporally at points where Hapi D has high, intermediate, and low antenna temperatures, i.e. covering a wide range of conditions. At these points, the Hapi C T_{SMM} are located within the error bars of the Hapi D T_{SMM} . The strong similarity between the neighbouring

⁵The graphical rendering uses a degraded shape model with 5×10^4 facets.

regions suggests that Hapi D is similar to its surroundings, at least in the more shallow surface layer sampled by the SMM. The Hapi C MM curve is also very similar to the Hapi D MM curve. Although the SMM observations have sufficiently high-resolution to not mix signals from Hapi C and D, this is not necessarily the case at MM. However, even if the MM observations of Hapi C might contain peripheral signal from Hapi D, that contribution is very small due to the Gaussian shape of the instrument sensitivity profile that peaks at the beam centre. If Hapi D had been drastically different from its surroundings (at the slightly larger depth sensed at MM wavelengths), the antenna temperatures ought to have changed measurably when the beam centre moved from Hapi D to Hapi C. The lack of such a change again suggests that the two regions have very similar physical properties. It is therefore likely that the MM observations indeed are representative of Hapi D despite the relatively large footprint that includes surrounding terrain. We recall that the spectral slope change in Hapi C (represented by the magenta square in Fig. 4 and in Table 1) also was very similar to that in Hapi D. This further strengthens the notion that both regions experienced the same thermophysical and spectral evolution.

3 NUMERICAL MODELS

Section 3.1 describes the calculations performed to obtain illumination conditions for Hapi D. These are fed to two nucleus thermophysical models of different levels of complexity, BTM (Section 3.2) and NIMBUS (Section 3.3). The resulting physical nucleus temperature, as function of time and depth, are fed to the radiative transfer equation solver THEMIS described in Section 3.4, that calculates the emitted radiance and converts those to synthetic antenna temperatures that can be directly compared with MIRO observations. Note that we first describe our nominal approach, which takes advantage of the global flatness of Hapi D to calculate temperatures for a representative location within that region, instead of performing point-by-point evaluations of temperature within the MIRO beams. This approach is later motivated in Section 3.4.2.

3.1 Illumination conditions

In order to calculate the illumination conditions at Hapi D we proceed as follows. The facets at Hapi D on the 3.1×10^6 -facet SHAP5 version 1.5 shape model had already been identified (Section 2.2). The average outward surface normal vector was calculated (because the region is rather flat, the normal vectors of individual facets deviate at most a few degrees from the average). Because the million-facet shape model is too large to practically carry out some of the calculations to follow, MESHLAB was then used to degrade the SHAP5 version 1.5 shape model to one with 5×10^4 facets, and the facets corresponding to Hapi D on that model were identified. Among those, a centrally placed facet with a surface normal close to the average Hapi D normal vector of the high-resolution model was found (aligned to within $1^\circ.6$). We took this facet, here called F#1, to represent Hapi D.

An algorithm developed by Davidsson & Rickman (2014) was used to identify the 2,698 facets on the degraded shape model that are visible from F#1 (here called ‘the terrain’). We emphasize that this method carefully avoids including facets that formally are along a line-of-sight, but are located behind foreground topography. Terrain facets are capable of shadowing F#1 by intercepting the line between F#1 and the Sun. They are also capable of illuminating F#1 with parts of their scattered visual and emitted infrared radiation (this process is referred to as ‘self-heating’, meaning one facet of the

nucleus radiatively heats another facet). We also identified the 14 672 facets that are visible from at least one terrain facet (here called ‘the surroundings’). These are facets capable of shadowing the terrain. We used the model by Davidsson & Rickman (2014) in order to calculate the total flux at F#1 (direct solar and diffuse self-heating by scattered visual and emitted infrared radiation from the terrain) at specific nucleus rotational phases, throughout one 67P orbit around the Sun (applying the nucleus spin axis determined by Jorda et al. 2016).

Specifically, we calculated all view factors of the terrain facets with respect to F#1, and the approximate temperatures of terrain facets by balancing local direct solar illumination with thermal reradiation, assuming zero albedo. The temperatures were set to zero if a terrain facet was shadowed by the surroundings. This temperature distribution across the terrain was then used to calculate the self-heating flux on to F#1 at any given rotational phase and orbital position. The direct solar flux was added, unless the Sun was located behind nucleus topography, as seen from F#1.

This is a simplification with respect to the nominal model of Davidsson & Rickman (2014), that evaluates temperatures based on *all mutual exchanges of radiation between facets*, and additionally accounts for heat conduction (either along each facet surface normal, or in full 3D). The simplifications meant substantial savings in calculation time, while still providing reasonably accurate illumination conditions at F#1. By ignoring self-heating at terrain facets themselves, the local fluxes are off by typically ~ 10 – 20 per cent, corresponding to $\lesssim 10$ K. By setting the albedo of terrain facets to zero, we artificially remove scattered visual radiation (with respect to the real surface) but increase the thermal emission by the corresponding amount. As seen from F#1, it still receives the same amount of energy it would have done for a realistic albedo (assuming that scattering is Lambertian, as is the case for thermal emission). By ignoring heat conduction effects, terrain facets do not experience the modest thermal lag of the real nucleus surface. By setting the temperature of shadowed terrain facets to zero, we somewhat reduce the self-heating flux at F#1 (but it would have been worse to allow those facets to illuminate F#1 as if having been fully exposed to sunlight). In reality, shadowed regions would have temperatures of ~ 130 K, compared to the ~ 215 K of the surrounding cliff walls (if illuminated) that provide most self heating. To evaluate the error in the flux on to F#1, introduced by assuming 0 K for shadowed terrain facets, we made test simulations with shadows at 130 K for the two master periods. In October, the total flux increased by 6.2 (mean) and 3.7 (median) per cent. The corresponding numbers for November were 7.4 and 3.9 per cent. In terms of physical temperature, that corresponds to a 2.2–2.5 K increase if assuming $\Gamma = 0$, but smaller values for our actual modelling, that includes a non-zero thermal inertia. The antenna temperatures would be affected even less, therefore we consider our assumptions acceptable.

To further test the effect of uncertainties in the calculated self-heating, it was reduced by half during the October master period and the model re-run. The resulting reduction of the MM antenna temperature was at most 3.8 K, and on average it was 1.6 K. For the SMM, the maximum antenna temperature drop was 5.0 K, and the average was 2.0 K. It therefore seems that the self-heating would have to be off by a factor of ~ 2 in order to give errors in the antenna temperatures that start to approach (and locally exceed) the ± 2.5 K error margins applied for the binned data. To have errors in the self-heating flux of this magnitude, the temperatures would have to be systematically off by more than 30 K (e.g. a drop from 200 to 168 K corresponds to a 50 per cent lower flux). Systematic errors in temperature of that magnitude are not likely.

We performed illumination condition calculations for F#1 every 10° of nucleus rotational phase for a full 360° nucleus rotation, at every 12th nucleus rotation, throughout the orbit. Because illumination conditions change very slowly with time, an accurately evaluated illumination sequence was therefore copied to the next 11 rotations, before the actual conditions were calculated anew (in order to obtain a continuous time-sequence). The master periods were evaluated accurately with a higher resolution (1° in nucleus rotation angle) compared to the 10° applied elsewhere. The calculation of the nucleus rotational phase accounted for the changes in nucleus rotation period caused by outgassing torques. We used a table of nucleus rotation periods throughout the mission as determined by ESA in weekly internal *Rosetta*-team communications, assembled by Dr. H. U. Keller (private communication), of which some have been published (Keller et al. 2015a). We validated our calculations of the nucleus rotational phase by generating synthetic views of the nucleus (including shadows caused by topography) as seen from *Rosetta*, that were cross-compared with actual OSIRIS images.

Fig. 6 (lower left-hand panel) exemplifies the evaluated flux for F#1 at Hapi D during the 2014 October 13 master period. As seen, the daytime illumination of Hapi D is interrupted by shadowing (caused by the small lobe) during an ~ 2 h period. According to our calculations, the onset of sudden full illumination at F#1 took place just prior to the MIRO observations corresponding to the fifth bin in Fig. 7 (left-hand panel). Because of the finite sizes of the SMM and MM footprints, the transition is in reality not instantaneous, and it took place at different times in the two channels. At the time of the fifth bin, calculations show that the SMM FWHM only viewed illuminated terrain. Indeed, the SMM channel has registered a substantial antenna temperature increase with respect to the previous bin. However, at this point, a substantial fraction of the MM FWHM was still in shadow, and the corresponding antenna temperature bin is the coldest in the sample. During analysis, several variants of partial illumination were tested, but as it turned out, it was very difficult to match the observed low MM antenna temperature. Therefore, the nominal approach for analyzing the MM data was to extend the period of shadowing by an additional ~ 15 min, so that the fifth bin was still in full darkness. In Section 4.1.2, we find that models including CO_2 reaches the low T_{MM} more readily than models only containing H_2O . If partial illumination of the MM beam at the dip had been included, the need for such additional cooling would only have become stronger. The solar flux file generated as described in Section 3.1 was passed to both thermophysical models (described in the following).

3.2 The basic thermophysical model BTM

The first-thermophysical model applied in this paper is relatively simple. It considers a homogeneous, porous medium with fixed (i.e. temperature-independent) heat conductivity and heat capacity. The Hertz factor (correcting the heat conductivity for porosity) is used to give the medium a desired thermal inertia Γ . The temperature (as function of depth and time) is obtained by solving the 1D energy conservation equation (accounting for heat conduction). The boundary condition at the upper surface balances the absorbed radiation (the flux in Section 3.1 corrected for albedo), the thermal emission to space, the conductive heat flow to/from the surface and the interior, and energy consumption due to sublimation of surface water ice. Sublimation only takes place from a part of the available surface area, given by the volumetric ice fraction f_i of the medium. The refractory and icy patches are assumed to be sufficiently small and well mixed to be isothermal.

Accounting for the possibility of having thermally isolated patches of hot dust and cold ice would only be important if the ice coverage is large, but in Hapi it is $\ll 5$ percent, except in small zones near shadows (De Sanctis et al. 2015). The model does not consider sub-surface sublimation, condensation, or vapour transport, nor stratification or erosion.

We refer to this as the Basic Thermophysical Model, or the BTM. The governing equations have been provided elsewhere (see section. 2.3, Davidsson et al. 2021) and are not repeated here. The physical properties taken into consideration are admittedly simple: this is intentional. If observational data can be fitted by such a simple model, it means that the effects of real and significant deviations from the model limitations are not detectable. This, by itself, disqualifies any claim that higher order physics is necessary in order to explain the observations. However, if no BTM fits the data convincingly, or only does so for unphysical parameter values, there is a real need to introduce a more elaborate description of the physical environment in the upper layer of the comet nucleus. By carefully scrutinizing if, how, and when BTM fails, important information is provided that can be used to better understand what additional physical processes need to be introduced. For this reason, we make quite some effort in describing ‘failed’ solutions, because we believe they are illuminating in the process of better understanding the cometary near-surface region.

The parameters used to run the BTM are summarized in Table 2. We solve the 1D energy conservation equation using the finite element method. We always resolved the diurnal skin depth by ~ 6 equidistant grid cells. With the parameters in Table 2, this corresponded to grid cell thicknesses of $(1-7.7) \times 10^{-3}$ m for a thermal inertia $\Gamma = 30-230$ MKS. We always applied 3400 grid cells, thus modelling the upper 3.4–26.2 m of the nucleus (a zero temperature-gradient boundary condition was applied at the lower boundary, placed several times below the seasonal skin depth). All models were run from aphelion (with an initial temperature of 120 K) up to and including the October or November 2014 master period under consideration, with 10-s time-step.

3.3 The advanced thermophysical model NIMBUS

The second thermophysical model applied in this paper is relatively complex. We use the Numerical Icy Minor Body evolUtion Simulator, or NIMBUS, that is fully described by Davidsson (2021). In its currently applied form, it considers a porous mixture of dust, crystalline water ice, and (in certain models) CO_2 ice. NIMBUS has the capability to consider amorphous and cubic water ice, as well as CO ice (that partially may be trapped in any of the H_2O ices and/or the CO_2 ice), but such material is not considered here (heating by short- and long-lived radionuclides is switched off as well). The ices are considered finite resources, which means that they may form sublimation fronts that withdraw underground. Heat is transported both through solid-state conduction and through radiative transfer, using temperature-dependent heat conductivities that have been measured in the laboratory for all species under consideration (heat capacities are temperature-dependent as well). NIMBUS considers sub-surface sublimation, gas diffusion within the porous medium along temperature and vapour pressure gradients, gas venting to space at the upper surface, and recondensation at depth if sufficiently cool regions are encountered by the vapour. These processes consume (sublimation), release (condensation), and transports (advection) energy as well. In essence, NIMBUS solves a coupled system of differential equations describing energy and (vapour/ice) mass conservation.

Table 2. These parameters were applied in the Basic Thermophysical Model (BTM) work. The only free parameters are f_i and Γ (regulated through h). For evaluating the thermal skin depth, we applied a fixed approximate nucleus rotation period of $P = 12.4$ h (Mottola et al. 2014). Here, ‘ice’ means H_2O .

Quantity	Symbol	Value	Unit	Reference/comment
Input parameters				
Hertz factor	h			
Volumetric ice fraction	f_i			
Constants				
Bond albedo	A	0.0123 ± 0.007		Fornasier et al. (2015)
Ice specific heat capacity	c_i	1200	$\text{J kg}^{-1} \text{K}^{-1}$	Klinger (1981) Average of 100 K, 200 K values
Dust specific heat capacity	c_d	420	$\text{J kg}^{-1} \text{K}^{-1}$	Forsterite, Robie, Hemingway & Takei (1982) Average of 100 K, 200 K values
Ice latent heat	$L_{\text{H}_2\text{O}}$	$2.66 \cdot 10^6$	J kg^{-1}	Tancredi, Rickman & Greenberg (1994) 200 K value
Emissivity	ε	0.9		Standard
Ice conductivity	κ_i	4.25	$\text{W m}^{-1} \text{K}^{-1}$	Klinger (1980) Average of 100 K, 200 K values
Dust conductivity	κ_d	5.00	$\text{W m}^{-1} \text{K}^{-1}$	Forsterite, Horai (1971)
Ice density	ρ_i	917	kg m^{-3}	Weast (1974)
Dust density	ρ_d	3250	kg m^{-3}	Forsterite, Horai (1971)
Porosity	ψ	0.7		Pätzold et al. (2019)
Dependent parameters				
Volumetric heat capacity	$c = (1 - \psi)(\rho_i f_i c_i + \rho_d f_d c_d)$		$\text{J m}^{-3} \text{K}^{-1}$	
Heat conductivity	$\kappa = h(f_i \kappa_i + (1 - f_i) \kappa_d)$		$\text{W m}^{-1} \text{K}^{-1}$	
Thermal inertia	$\Gamma = \sqrt{c\kappa}$		$\text{J m}^{-2} \text{K}^{-1} \text{s}^{-1/2} = \text{MKS}$	
Thermal skin depth	$\mathcal{L} = \sqrt{P\kappa/2\pi c}$		m	

The full-scale NIMBUS code considers both radial and latitudinal internal transport of energy and vapour. However, the current work applies a specialized version (NIMBUSD with D for ‘dust’) that sacrifices latitudinal energy and mass transport in order to enable erosion of the upper surface (injecting dust and potentially ice into the coma, while thinning the dust mantle). Such simplifications are acceptable because of the short-duration of the current simulations (latitudinal energy and mass transport are important on geological time-scales). We apply the erosion rate (as function of heliocentric distance) of Davidsson et al. (2022b), based on *Rosetta* observations of the 67P dust mass-loss. Because there is no risk of confusion as to which version is being applied in the current paper, we here refer to NIMBUSD simply as NIMBUS.

The governing equations and many auxiliary functions are described in detail by Davidsson (2021) and are not repeated here. The initial composition is determined by assigning a certain mass ratio between refractories and water ice μ , and a certain molar abundance of CO_2 relative to water (see Sections 4.1.2 and 4.2.2). The initial porosity is determined by requiring a bulk density of 535 kg m^{-3} (Preusker et al. 2015). Overtime the porosity and bulk density change because of local sublimation of ice and recondensation of vapour. The heat conductivity and heat capacity depend on the continuously changing porosity and temperature, as well as on a porosity-dependent Hertz factor, obtained by using the method of Shoshany, Prialnik & Podolak (2002). This gives rise to a certain (range of) instantaneous thermal inertia during nucleus rotation. Deviations from this nominal Hertz factor correction (introduced when it is desirable to drastically change the thermal inertia) are described in Sections 4.1.2 and 4.2.2 when necessary. Another important free parameter in NIMBUS in the context of the current simulations is the diffusivity (regulated through tube lengths L , tube radii r_p , and tortuosity ξ , see equation 46 in Davidsson 2021). NIMBUS is fed with the same illumination sequence as the BTM (see Section 3.1). NIMBUS here uses radial grid cells that grow with

geometric progression from 1 mm at the surface to 200 m at the core. It uses a dynamic time-step that ensures that certain criteria regarding changes of energy and pressure are respected at all times.

3.4 The radiative transfer model THEMIS

3.4.1 Fundamentals and nominal procedures

The temperature as function of depth, obtained with BTM or NIMBUS, is fed to a radiative transfer equation solver called THEMIS (short for THERmal EMISSion) that calculates the radiance emitted toward MIRO, that can be converted to a synthetic antenna temperature. THEMIS is a Monte Carlo-based parallel code implemented in C++/MPI by one of us (Davidsson), described here for the first time. THEMIS generates a large number of ‘test photons’ in proportion to the Planck function, evaluated at the local temperature and wavelength λ . Each photon is emitted into a random direction, and is followed individually through a sequence of transfers (with lengths chosen at random to statistically conform with a given extinction coefficient E_λ) and interactions with the solid medium. The interaction can be absorption (the photon is lost), scattering (with a probability determined by the scattering coefficient $S_\lambda = w_\lambda E_\lambda$, where w_λ is the single-scattering albedo), or escape across the upper boundary. In case scattering takes place, a new direction of motion and flight distance to the next interaction are selected, and the process repeats until the photon is absorbed, escapes, or penetrates so deep into the medium that it most likely will not make it across the upper boundary. THEMIS keeps track of the number of escaping photons, and the angle between the surface normal and their direction of travel at the time of escape. This information is used in order to calculate the radiance $R_\lambda(e)$ of emitted radiation from the comet surface, as function of emergence angle e . Given a certain temperature profile (that changes with time during nucleus rotation), the only free parameters of the

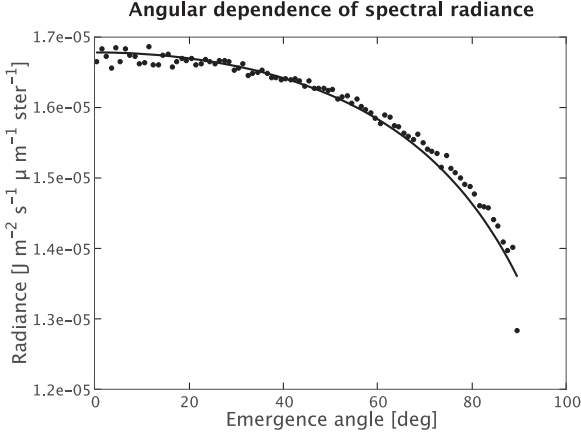


Figure 9. Verification of the numerical radiative transfer equation solver THEMIS (dotted curve) against the analytical Hapke solution, equation (3), as a solid curve.

model are the extinction coefficient E_λ and the single-scattering albedo w_λ .

In order to verify the correctness of THEMIS radiances, we cross-checked it against known solutions to the radiative transfer problem. Under the condition that the radiation source function can be written on the form

$$U(\tau) = U_0 + U_1 \exp(-\tau/Y), \quad (2)$$

(where U_0 , U_1 , and Y are constants and τ is optical depth), and in the limit of isotropic scattering, Hapke (1993) demonstrated that the equation of radiative transfer can be solved analytically, with the radiance given by

$$I_\lambda(e) = \gamma H(\mu_e) \frac{U_0}{\pi} + \frac{Y}{Y + \mu_e} \gamma^2 H(Y) H(\mu_e) \frac{U_1}{\pi}, \quad (3)$$

where $\mu_e = \cos(e)$,

$$H(x) = \frac{1 + 2x}{1 + 2\gamma x}, \quad (4)$$

and

$$\gamma = \sqrt{1 - w_\lambda}. \quad (5)$$

In one specific verification attempt of THEMIS, a temperature profile with $T = 200$ K at the surface, falling linearly to $T = 150$ K at a depth of $z_{\max} = 0.15$ m was considered. An extinction coefficient of $E_{\text{MM}} = 338 \text{ m}^{-1}$ was applied for the relation between optical and physical depths of $\tau = E_{\text{MM}} z$, and the Planck function was used to generate a radiation source function $P_{\text{MM}} = P_{\text{MM}}(\tau)$. The parameter $U_0 = 5.9875 \times 10^{-5} \text{ J m}^{-2} \text{ s}^{-1} \mu\text{m}^{-1}$ was obtained from $U_0 = P_{\text{MM}}(\tau = 1.3)$, and the $\tau \leq 1.3$ part of $\ln(P_{\text{MM}}(\tau) - U_0)$ was fitted with a linear curve in a least-squares sense, having a slope Y^{-1} and crossing with the $\tau = 0$ axis of $\ln U_1$. That allowed us to evaluate $U_1 = 3.3755 \times 10^{-7} \text{ J m}^{-2} \text{ s}^{-1} \mu\text{m}^{-1}$ and $Y = 0.61532$. It was verified that equation (2) provided a reasonable fit to $P_{\text{MM}}(\tau)$ down to an optical depth of unity. Assuming $w_{\text{MM}} = 0.5$, equation (3) was evaluated for these values of $\{U_0, U_1, Y\}$, as shown by the solid curve in Fig. 9. THEMIS was run with $\lambda = 1.594 \times 10^{-3} \text{ m}$, $E_{\text{MM}} = 338 \text{ m}^{-1}$, and $w_{\text{MM}} = 0.5$, using 150 depth bins, 90 emergence angle bins in the upper hemisphere and generating 4×10^8 Monte Carlo test photons, of which 8.6×10^6 escaped through the upper surface and contributed to the THEMIS solution seen in Fig. 9 as dots. The similarity between the THEMIS solution and equation (3) is sufficiently high for us to have confidence in our numerical radiative

transfer calculations. We emphasize that the reason for using THEMIS instead of equation (3) for the simulations in this paper is that THEMIS can handle any temperature versus depth function, whereas the analytical solution is limited to situations where equation (2) applies.

The THEMIS simulations in this paper all used 9.6×10^7 test photons, 90 emergence angle bins (each 1° wide), and a slab thickness d_z that would result in radiation being attenuated to a fraction $\exp(-d_z E_\lambda) = 10^{-6}$ when escaping at the surface, compared to the production at that depth. The calculated radiances $R_\lambda(e)$ are converted into a synthetic antenna temperature as follows (see Gulkis et al. 2010, but note that we here express the radiance per wavelength interval instead of per frequency ν interval, remembering that $R_\lambda(e) = c_0 R_\nu(e)/\lambda^2$):

$$T_{\text{sy}} = \frac{R_\lambda(e) \lambda^4}{2c_0 k_B}, \quad (6)$$

where c_0 is the speed of light in vacuum and k_B is the Boltzmann constant. The differing antenna temperatures at SMM and MM are obtained by applying the corresponding channel wavelength λ (furthermore, the applied extinction coefficients E_{SMM} and E_{MM} , as well as single-scattering albedos w_{SMM} and w_{MM} depend on λ).

As seen from Fig. 9, the calculated radiance often depends on the emergence angle e when temperature changes with depth. When calculating antenna temperature curves for the master periods, we applied the e -values valid at the time of MIRO observations, as seen for several bins in Fig. 7. In order to obtain a continuous synthetic antenna temperature curve, we applied interpolated e -values between bins.

The solution provided by THEMIS works for materials with substantial surface roughness on the MM-decimetre size scale, but not for perfectly flat medium/vacuum interfaces, for the following reason. When radiation within a solid medium reaches a flat boundary with vacuum, a fraction of the radiation is reflected and the remainder is transmitted according to the Fresnel law. Transmission dominates at small emergence angles, but for $e \gtrsim 50^\circ$ the reflected fraction grows rapidly and is additionally a function of polarization: the reflection is stronger for radiation having its electric field oscillating perpendicularly to the plane of incidence than when the field oscillates parallel to it (see, e.g. Lagerros 1996). This means that the emissivity (the ratio between the emerging radiance and the Planck function evaluated for the surface temperature) drops rapidly at $e \gtrsim 50^\circ$ (even for isothermal media). Furthermore, the MIRO SMM and MM receivers observe the nucleus in orthogonal polarizations, which potentially could introduce systematic differences in the observed intensity at large emergence angles. However, surface roughness randomises the orientation of locally planar boundaries. Lagerros (1996) demonstrates that surface roughness rapidly removes the part of the emergence-angle dependence of microwave transmission caused by refraction. For this reason, THEMIS does not apply Fresnel expressions when evaluating the emerging radiance. The same is true for the Hapke (1993) solution above: the reflection and transmission governed by the Fresnel expressions are applied on constituent grain level (when calculating the single-scattering albedo as function of the refractive index of the grain material) but not at the interface between the medium and the exterior vacuum. In fact, the THEMIS solution is very close to that of Hapke (1993) according to Fig. 9. The question is then whether the surface material at Hapi D behaves more like a flat or a rough medium. Fig. 7 (left-hand panel) has two bins near $d_0 = 287$ with $e = 52^\circ$ and 77° . The fact that the measured MM antenna temperatures are virtually identical, and the SMM differing by merely ~ 2 K speaks against a strong e -dependence

Table 3. This table quantifies the difference between calculating the antenna temperature \tilde{T}_{MM} based on all facets within the MM FWHM \times 1.5 footprint, and just considering a single representative facet F#1 with antenna temperature $\tilde{T}_{\text{F\#1}}$. Footprint facets have individually calculated illumination conditions, BTM thermophysical solutions (assuming ice-free media with $\Gamma = 30$ MKS) and radiances (assuming $E_{\text{MM}} = 25 \text{ m}^{-1}$), and contribute to \tilde{T}_{MM} in proportion to their projected surface area and beam power at the relevant distance from the beam centre. The small $\delta\tilde{T}_{\text{MM}} = \tilde{T}_{\text{F\#1}} - \tilde{T}_{\text{MM}}$ values indicate nearly isothermal footprints due to quasi-flat terrain.

October				November			
Bin	e	\tilde{T}_{MM}	$\delta\tilde{T}_{\text{MM}}$	Bin	e	\tilde{T}_{MM}	$\delta\tilde{T}_{\text{MM}}$
#1	34.5	171.2	+0.5	#1	61.7	177.1	+1.7
#2	69.8	181.8	-0.7	#3	61.1	178.3	+1.3
#3	64.5	182.5	-1.6	#5	59.9	179.3	+0.9
#4	71.6	163.4	+5.6	#7	58.8	180.0	+0.6
#5	73.3	167.0	+3.7	#9	57.7	180.6	+0.2
#6	67.8	184.4	-4.2	#11	58.5	181.2	-0.1
#20	73.6	189.2	-3.1	#13	57.6	181.6	-0.3
#26	74.8	191.2	-3.5	#15	55.1	181.2	-0.5
#27	48.2	184.6	-2.0	#17	54.3	181.0	-0.7
#28	45.3	179.1	+1.6				
#30	77.4	173.4	-1.1				

for radiation transmission. Additionally, the antenna temperatures for observations with $e = 64^\circ$ and 70° near $d_n = 286.7$ are similar as well, at both SMM and MM. To fully account for roughness, we apply a beaming effect that increases R_λ by a factor of 1.04 (Müller 2002). We therefore consider THEMIS adequate for modelling emission from the rough surface of Hapi D.

3.4.2 Testing the need for sub-FWHM temperature resolution

If the temperature varies drastically within the MIRO beams, it is necessary to calculate the radiance as function of position within the fields of view. However, a sizeable region at and around Hapi D is nearly flat and similarly illuminated, so the emission within the MIRO beams is expected to be homogeneous on macroscopic level.

To quantify the level of temperature dispersion within the beam footprints, all facets within the MM FWHM \times 1.5 footprint were identified (this 36 arcmin region collects 92 per cent of the observed power) for a given October or November bin, and their illumination conditions were calculated for the relevant master period, including self heating and shadowing from the terrain facets. Temperatures versus time and depth were calculated individually for each facet using an ice-free BTM model with $\Gamma = 30$ MKS, for simplicity considering steady-state solutions. Radiances emerging from each facet were calculated, assuming $E_{\text{MM}} = 25 \text{ m}^{-1}$. Those were used to calculate a weighted mean antenna temperature \tilde{T}_{MM} , equivalent to what would have been observed with the MM channel. The weighting factors included both the projected facet areas as seen from along the line of sight, as well as a Gaussian beam power profile with a FWHM of 23.8 arcmin that reduces the relative importance of the radiance contribution with increasing distance from the footprint centre. This was compared to the corresponding antenna temperature emanating from the representative facet F#1 itself, $\tilde{T}_{\text{F\#1}}$, assumed to apply within the entire footprint.

Table 3 reports the emergence angle e , the antenna temperature \tilde{T}_{MM} , as well as the difference $\delta\tilde{T}_{\text{MM}} = \tilde{T}_{\text{F\#1}} - \tilde{T}_{\text{MM}}$ for a selection of bins from both the October and November data sets (counted consecutively from left to right, as displayed in Fig. 7). In October, bins #1–#3 constitute the beginning of the curve and the first-peak,

bins #4 and #5 are at the first-dip, bins #6, #20, and #26 represent the continuous stare, #27–#28 constitute the second peak, and #30 represents the end of the curve. The differences between full-beam and F#1 synthetic antenna temperatures are admittedly somewhat larger than the ± 2.5 K uncertainties of the data. Yet, they are small compared to the level of variation in the observed data that we try to fit (and as it will turn out, compared to the 10–30 K level discrepancies between the data and the best models achievable prior to the introduction of the solid-state greenhouse effect and CO_2 ice). Also note that the differences will be substantially smaller at SMM, because of the thinner beam.

Because the November footprint sizes tend to be smaller than the October ones (see Section 2.2.3), we expected $\delta\tilde{T}_{\text{MM}}$ to be smaller as well. To verify this expectation, we considered a selection of bins limited to the sunlit part of the continuous stare (bins #1–#17). Indeed, the November $|\delta\tilde{T}_{\text{MM}}|$ values are smaller, and are all below 2.5 K. Note, again, that $|\delta\tilde{T}_{\text{SMM}}|$ would be smaller still. This reinforces the visual impression that Hapi D (and the extended region fitting within the MM footprint) is quasi-flat, thus similarly illuminated, and consequently rather isothermal.

Because we need to consider illumination conditions with high (~ 20 min) temporal resolution for an orbital arc stretching over several years, performing this type of evaluation (and the associated thermophysical modelling) for each facet in the MIRO footprints is not computationally feasible – thus direct illumination, self heating, and thermophysical modelling is only made for the representative facet F#1 (for which THEMIS provides the radiance $R_\lambda(e)$). Based on the investigation presented in Table 3, we consider the observed terrains sufficiently flat and isothermal to allow for such a simplified treatment.

3.4.3 Goodness of fit

In order to quantify the goodness of fit of a synthetic antenna temperature curve $T_{\text{sy}}(t)$ with respect to the observed MIRO antenna temperature $T_{\text{A}}(t)$ with uncertainties ΔT_{A} at M specific instances (the bins), we calculate the incomplete gamma function (see Press et al. 2002). It is given by

$$Q = Q(\beta, \omega) = \frac{\int_0^\omega e^{-z} z^{\beta-1} dz}{\int_0^\infty e^{-z} z^{\beta-1} dz}, \quad (7)$$

where $\beta = (M - \eta)/2$, η is the number of free parameters in the model, and $\omega = \chi^2/2$, where

$$\chi^2 = \sum_M \left(\frac{T_{\text{sy}}(t) - T_{\text{A}}(t)}{\Delta T_{\text{A}}} \right)^2 \quad (8)$$

is the χ^2 residual between measurements and model.

Assuming that T_{sy} represents reality, a single attempt by MIRO to measure the diurnal antenna temperature curve at the M bins would result in some residual χ^2 , because T_{A} at each bin would be off by some amount consistent with the standard deviation ΔT_{A} . Hypothetically, if MIRO could repeat the measurements of the same temperature curve a large number of times (each having a χ^2 -value corresponding to that particular attempt) one would obtain a distribution of χ^2 values. $Q(\beta, \omega = \chi^2/2)$ is the probability that the particular χ^2 -value (for which it is evaluated) is exceeded by chance in a single measurement of T_{A} . That is to say, the closer Q is to unity, the higher the probability that any discrepancy between T_{A} and T_{sy} is due to ‘bad luck’ (i.e. for a large number of $T_{\text{A}}(t)$ measurements the averaged curve would approach T_{sy}). Of course, $T_{\text{A}}(t)$ is the measured reality, and $Q \ll 1$ will be interpreted as T_{sy}

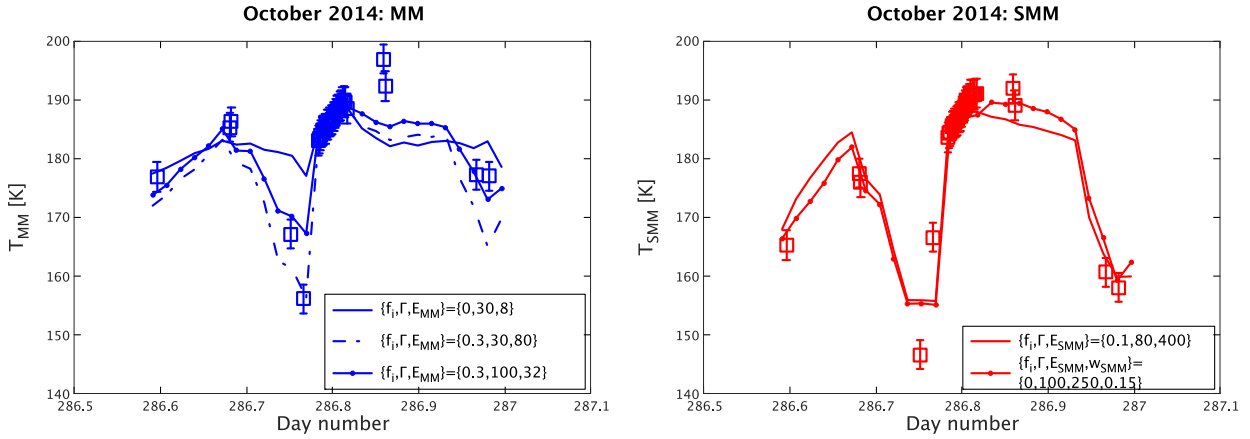


Figure 10. Left-hand panel: BTM solutions versus MIRO October 2014 MM data. Ice-free media are far too warm, unless an unrealistically low extinction coefficient is applied, which then makes the amplitude too small. Adding significant cooling due to water ice sublimation, and applying a low thermal inertia matches parts of the curve, but the highest antenna temperatures are not reproduced. No BTM model managed to reproduce the MIRO MM data, regardless of ice abundance, thermal inertia, extinction coefficient, or single-scattering albedo. Right-hand panel: BTM solutions versus MIRO October 2014 SMM data (assuming $B_c = 0.96$). The best available fits do not match the lowest antenna temperature. Furthermore, the low abundance and high thermal inertia is inconsistent with the MM solutions.

not being a good representation of that reality. It is customary that a theoretical curve is considered to provide a good fit to measured data if $Q \geq 0.01$ (Press et al. 2002), and this is the criterion that will be considered in this paper.

As previously mentioned, we apply $\Delta T_A = 2.5$ K. The BTM has $\eta = 3$ at MM (f_i , Γ , E_{MM} are free parameters) and $\eta = 4$ at SMM (addition of the SMM single-scattering albedo w_{SMM}). We nominally do not consider scattering at MM (i.e. $w_{MM} = 0$) because it is not seen on the Moon (Gary & Keihm 1978) and we assume that the granular material of the comet is similar to lunar regolith in terms of optical properties. We applied the same η -values for NIMBUS to allow for a direct comparison between the models.

We noticed one flaw of this method. Some models fitted the dense swarms of bins (see Fig. 7) at $d_n \approx 286.80$ (October 2014) or $d_n \approx 314.55$ (November 2014) extremely well, which yielded a high Q -value despite the fact that T_{sy} completely missed one or several bins elsewhere. In order not to bias the goodness of fit to that particular dense part of $T_A(t)$, the swarms were replaced by three representative bins during Q -evaluation. By doing so, false-positives were avoided, and $Q \geq 0.01$ values were only obtained when the entire overall $T_A(t)$ was well represented by a T_{sy} model curve. We note that Q is a strongly non-linear function. In cases where visual inspection would suggest that there was ‘almost a fit’, the Q -value would still be very low ($\sim 10^{-8}$, and often orders of magnitude lower), unless T_{sy} was fully statistically consistent with the bins and their error bars. In the following, when stating that a model does not fit the data, it implies $Q \ll 0.01$ (for brevity we rarely report the actual value).

4 RESULTS

4.1 October 2014

4.1.1 October: BTM results

The BTM has two free parameters: the volumetric ice fraction f_i and the thermal inertia Γ (the specific heat capacity is assumed fixed at the values in Table 2, and only the heat conductivity is varied). A small and sparse grid was originally considered, focusing on low thermal inertia and small ice abundance, consistent

with previous work (Schloerb et al. 2015). When finding solutions proved difficult, that grid was densified and extended into other regions of parameter space that appeared more promising. The final grid considered the $0 \leq f_i \leq 0.3$ interval with $\Delta f_i = 0.05$ resolution and $\Gamma = \{30, 50, 80, 100, 130, 150, 180, 200, 230\}$ MKS, plus a region with $0.35 \leq f_i \leq 0.55$ with the same Δf_i but $\Gamma = \{130, 150, 180, 200, 230\}$ MKS. Thus, a total of 88 thermophysical models were run. We first attempted to fit the MM data. For each BTM solution, the THEMIS code was run for different E_{MM} -values while keeping $w_{MM} = 0$, in order to find the antenna temperature solution with the smallest possible residual with respect to the empirical data. A total of 812 such THEMIS models were considered.

The simulations show that ice-free models are too warm for realistic E_{MM} -values ($E_{MM} = 26_{-6}^{+11} \text{ m}^{-1}$ on average, according to Schloerb et al. 2015). Generally, an increasing extinction coefficient increases the day-side antenna temperature. This is because a higher extinction coefficient means a larger number of absorbers per volume unit, which also translates to a larger number of emitters. At $\Gamma = 30$ MKS the extinction coefficient has to be reduced to $E_{MM} = 8 \text{ m}^{-1}$ (if so, material down to 12 cm depth would contribute significantly to the signal) for the modelled antenna temperature to drop to the level of the data. But then the amplitude is not anywhere near that of the observed curve, as seen in the left-hand panel of Fig. 10. Increasing the thermal inertia for such models only reduces the amplitude further.

When introducing cooling due to sublimation of near-surface water ice, the models can be brought to the general level of the data using more reasonable extinction coefficients. Fig. 10, left-hand panel, shows a case with $\{f_i, \Gamma, E_{MM}\} = \{0.3, 30 \text{ MKS}, 80 \text{ m}^{-1}\}$, that roughly has the right amplitude at the first-peak and dip. However, there are severe problems at the second peak. The model climbs correctly towards the second peak and reproduces the dense collection of data bins, but instead of reaching the high temperatures at $d_n \approx 286.85$ the model temperature drops. Model curves that are significantly warmer around $d_n \approx 286.8$ than at $d_n \approx 286.85$ (while the observed curve clearly indicates a continuously increasing antenna temperature beyond $d_n \approx 286.8$ that peaks at $d_n \approx 286.85$) are here referred to as having a ‘peak shape problem’. Additionally, the second dip near $d_n = 287$ becomes far too cold. Increasing

the thermal inertia, as illustrated in the left-hand panel of Fig. 10 by the $\{f_i, \Gamma, E_{\text{MM}}\} = \{0.3, 100 \text{ MKS}, 32 \text{ m}^{-1}\}$ model, reduces the amplitude (thus ruining the fit at the first-dip), without improving the situation at the second peak. There seemed to be a weak improvement by simultaneously increasing both f_i and Γ , but the best achievable model with $\{f_i, \Gamma, E_{\text{MM}}\} = \{0.4, 200 \text{ MKS}, 330 \text{ m}^{-1}\}$ performed as poorly as the $\{f_i, \Gamma, E_{\text{MM}}\} = \{0.3, 30 \text{ MKS}, 80 \text{ m}^{-1}\}$ model at the first dip and second peak, although the second dip was closer to the data.

Having failed to find convincing MM solutions with BTM for October 2014 when using $w_{\text{MM}} = 0$, scattering was introduced in the THEMIS modelling. We did this reluctantly because scattering is not expected at the MM wavelength, as mentioned previously. The effect of increasing w_{MM} is to lower the antenna temperature, so we applied $w_{\text{MM}} > 0$ for models that were too hot and increased the single-scattering albedo in steps of $\Delta w_{\text{MM}} = 0.05$ until reaching the level of the data, resorting to fine-tuning when it was deemed meaningful. We considered $777 w_{\text{MM}} > 0$ models spread across the thermophysical model grid, bringing the total of THEMIS MM runs to 1,589. The smallest residuals were obtained for $\{f_i, \Gamma, E_{\text{MM}}, w_{\text{MM}}\} = \{0, 130 \text{ MKS}, 50 \text{ m}^{-1}, 0.3\}$. Although most of the data bins could be fitted, the modelled temperature remained 10 K too warm at the first dip (despite the fact that the MM model assumed complete darkness at this point, even when some illumination of the actual footprint took place, see section 2.2.3). In conclusion, no convincing reproduction of October 2014 MM data could be found using thermophysical solutions based on BTM.

Next, the SMM case was considered. Another 18 thermophysical models were added to form a rectangular grid with $0 \leq f_i \leq 0.4$ ($\Delta f_i = 0.05$ resolution) and $\Gamma = \{30, 50, 80, 100, 130, 150, 180, 200, 230\}$ MKS. Higher f_i -values were not considered. For each $\{f_i, \Gamma\}$ combination, THEMIS was run at the SMM wavelength to find the E_{SMM} -value that minimised the residual between the synthetic antenna temperature curve and the empirical bins, assuming $w_{\text{SMM}} = 0$. In total, 208 such simulations were made. The closest match was found for $\{f_i, \Gamma, E_{\text{SMM}}\} = \{0.1, 80 \text{ MKS}, 400 \text{ m}^{-1}\}$. As seen in the right-hand panel of Fig. 10, that model is not sufficiently cold at the first dip, and failed to reproduce the second peak. Scattering is more likely to take place at SMM than at MM wavelengths, therefore another 258 THEMIS simulations with $w_{\text{SMM}} > 0$ were considered, bringing the total number of simulations to 466. The best of these simulations, having $\{f_i, \Gamma, E_{\text{SMM}}, w_{\text{SMM}}\} = \{0, 100 \text{ MKS}, 250 \text{ m}^{-1}, 0.15\}$ improved the fit at the second peak modestly (though not performing well at the continuous stare), and still failed to match the first dip. After having completed this extensive investigation of the parameter space we had to conclude that the Basic Thermophysical Model is not capable of reproducing the MIRO measurements and that its time-dependent temperature solutions, at and below the surface, do not match those of the comet. We note that the discrepancies were far too large to realistically be attributed to any of the simplifications described in Section 3.

4.1.2 October: NIMBUS results

As a starting point, a NIMBUS model with refractory to water ice mass ratio $\mu = 2$, tube length and radius $\{L, r_p\} = \{100, 10\} \mu\text{m}$, and tortuosity $\xi = 1$ was considered (these values were consistent with the pre-perihelion H_2O and CO_2 production rates observed by *Rosetta*/ROSINA, according to the NIMBUSD modelling by Davidsson et al. 2022b). In order to prevent the thermal inertia from decreasing

below ~ 30 MKS at high porosities, a Hertz factor $h = 0.0016$ ceiling was introduced (this constraint was later modified to consider lower thermal inertia in a controlled manner). The model was propagated from aphelion on 2012 May 23 to 2014 October 6 (at 3.23 au). To illustrate the weak water-driven activity in this ~ 2.3 yr segment of the orbit, the water withdrew merely 8.5 mm under the surface and the dust mantle was eroded by only 4 mm. The temperature distribution at the final date was used as initial condition for a series of simulations with different model parameters. Thus, a time period of ~ 8 days for thermal re-adjustments due to the new parameters were applied, before reaching the October 14 master period. A first series of 15 simulations systematically explored the effects of considering different dust mantle thicknesses (2–8 mm), thermal inertia ranges, and $\{L, r_p\}$ values. The thinner the dust mantle, and the larger the $\{L, r_p\}$ values, the more effective is the cooling due to water sublimation. The lower porosity below the dust mantle (because of the presence of ice), leads to enhanced heat conductivity and heat capacity in that region compared to the dust mantle. Furthermore, for $r_p \gtrsim 1$ mm, radiative heat transport starts to add visibly to the instantaneous thermal inertia. For the largest diffusivity considered, $\{L, r_p\} = \{28, 6.6\}$ mm, the total thermal inertia is ~ 25 MKS at night and ~ 50 MKS at day.

Moving the sublimation energy sink from the top cell (as in the BTM) to a sub-surface region surrounding the water ice sublimation front (as in NIMBUS) unfortunately did not introduce any significant qualitative changes to the synthetic antenna temperature curves. Applying temperature-dependent heat conductivities and heat capacities had no significant effect either. The peak shape problem remained severe, illustrated by the thin blue curve in the left-hand panel of Fig. 11. Note that BTM produced curves of that type as well, when using higher E_{MM} values than in Fig. 10 in order to force a match with the warmest MIRO antenna temperatures at $d_n \approx 286.85$. In short, a properly modelled dust mantle, overlaying a sublimating icy interior, did not provide a better match than the admittedly non-physical BTM scenario where all cooling takes place at the very surface.

We decided to try to understand the reason why the modelled antenna temperature, when applying a sufficiently large E_{MM} value to match the hottest measurements at $d_n \approx 286.85$, yielded an even higher temperature at $d_n \approx 286.8$ that exceeded the measurements by ~ 20 K or more. First it was recognized that the MIRO observations near $d_n \approx 286.8$ were acquired at very large emergence angles, sometimes exceeding $e = 75^\circ$, as seen in Fig. 7. Secondly, because of the relatively strong solar illumination at this point of the diurnal curve, the temperature gradient is very steep, having a high-surface temperature and cooling rapidly with depth (upper right-hand panel of Fig. 11). The analytical solution to the equation of radiative transfer (equation 3) was scrutinized to understand how the radiance would depend on emergence angle in such conditions. In the absence of scattering ($w_{\text{MM}} = 0$ and $\gamma = 1$), the $H(x)$ function (equation 4) becomes constantly equal to unity. It means that the first term in equation (3) is a constant, and that $H(\mu_e)$ in the second term no longer introduces any e -dependence. It is therefore only the term $Y/(Y + \mu_e)$ that is changing with emergence angle, taking a value of $Y/(Y + 1) < 1$ at nadir observations that grows towards unity as $e \rightarrow 90^\circ$ and $\mu_e \rightarrow 0$. Because $U_1 > 0$ for a negative temperature gradient (T falling with depth), the observed radiance is expected to increase strongly with e , growing from $I_\lambda(0) = (U_0 + |U_1|Y/(Y + 1))/\pi$ towards $I_\lambda(90^\circ) = (U_0 + |U_1|)/\pi$. Therefore, the unusually high-modelled antenna temperature near $d_n \approx 286.8$ appeared to be a consequence of a strongly negative temperature gradient in combination with very large e -values.

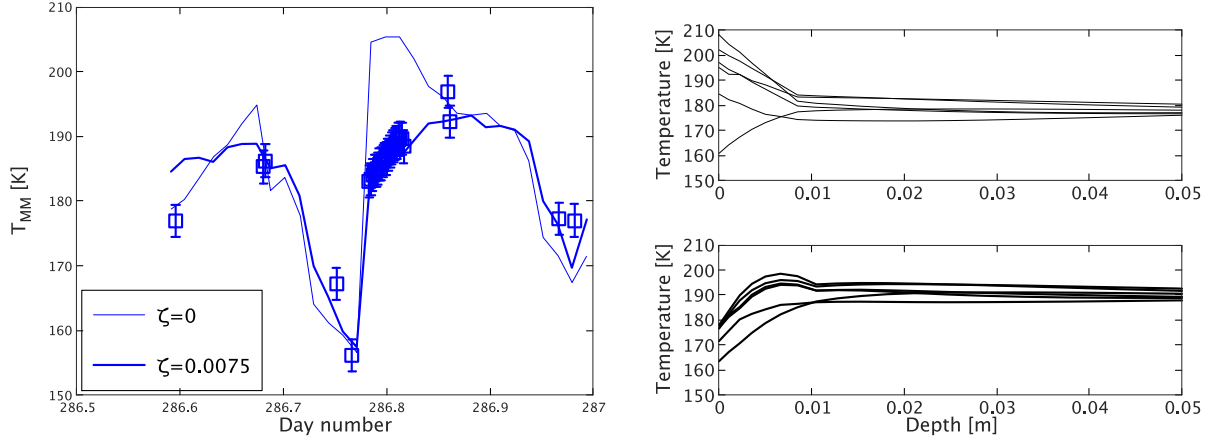


Figure 11. Left-hand panel: NIMBUS solutions versus MIRO 2014 October MM antenna temperatures. The model with $\zeta = 0$ had an 8 mm dust mantle and $\{L, r_p\} = \{10, 1\}$ mm. The model that included the solid-state greenhouse effect ($\zeta = 7.5 \times 10^{-3}$ m) had a 9.9 mm dust mantle and $\{L, r_p\} = \{7.5, 0.75\}$ mm. Both models were applying $E_{MM} = 100 \text{ m}^{-1}$. The large temperature reduction near day number $d_n = 286.8$ when ζ increases is caused by a high sensitivity of the radiative transfer solution to the sign of the near-surface temperature gradient at large emergence angles. The significant improvement of the fit as ζ increases is taken as evidence of the solid-state greenhouse effect in smooth terrain on Comet 67P. Right-hand panel: Physical temperature versus depth at a selection of time instances during day and night for $\zeta = 0$ (upper) and $\zeta = 7.5 \times 10^{-3}$ m (lower). Note that the solid-state greenhouse effect leads to positive near-surface temperature gradients at all rotational phases, and sub-surface temperature maxima.

However, if the temperature gradient is positive (T increasing with depth), then $U_1 < 0$ and equation (3) suggests that the observed radiance, as well as the antenna temperature, would fall strongly with increasing e , peaking at $I_\lambda(0) = (U_0 - |U_1|Y/(Y+1))/\pi$ at nadir and decreasing towards $I_\lambda(90^\circ) = (U_0 - |U_1|)/\pi$. That observation led to the suspicion that the MIRO measurements perhaps could be matched by a model that would have a positive temperature gradient on the day-side. Negative day-time temperature gradients are unavoidable in models that assume that the surface material is fully opaque to visual radiation, so that all solar energy is absorbed at the very surface. However, models that allow for a finite visual opacity (combined with opaqueness in the thermal infrared) absorb energy within a near-surface volume, as opposed to just the surface itself, while the radiative cooling from such depths is insignificant. Thus, day-side temperature profiles develop that peak at a certain depth, having temperatures that fall both towards the surface, and towards greater depths. An example is seen in the lower right-hand panel of Fig. 11. This phenomenon, referred to as ‘the solid-state greenhouse effect’ has been thoroughly explored theoretically (e.g. Brown & Matson 1987; Clow 1987; Matson & Brown 1989; Kömle, Dettlaff & Dankert 1990; Davidsson & Skorov 2002), experimentally (e.g. Kaufmann, Kömle & Kargl 2006, 2007; Kaufmann & Hagermann 2015), and has been observed in space (e.g. Urquhart & Jakosky 1996).

Accordingly, NIMBUS was modified to accept a flux profile $\exp(-z/\zeta)$ of incident radiation, where ζ is the e -folding scale of light penetration. A total of 30 NIMBUS models were run, considering $\zeta = 5 \times 10^{-3}$ m, $\zeta = 7.5 \times 10^{-3}$, and $\zeta = 10^{-2}$ m, with different dust mantle thicknesses on the range 6–27 mm and tube dimensions on the range $\{100, 10\} \mu\text{m} \leq \{L, r_p\} \leq \{28, 6.6\}$ mm. Most models had $\Gamma \approx 30$ MKS, except one low- r_p model for which $\Gamma \approx 50$ MKS was forced, and several high- r_p models that reach $\Gamma \approx 50$ MKS naturally through a significant radiative contribution to heat transfer. The peak shape problem was not resolved for $\zeta = 5 \times 10^{-3}$ m, but drastic improvements were seen for larger e -folding scales as long as the mantle was not too thick and the $\{L, r_p\}$ -values were not too large. An example of peak shape improvement (thick blue curve) caused by the solid-state greenhouse effect is seen in the left-hand panel

of Fig. 11, along with remaining issues that could not be resolved. Near $d_n = 286.8$ the antenna temperature drops from ~ 205 K when the medium is considered opaque ($\zeta = 0$) to ~ 185 K when light is absorbed with a penetration length-scale of $\zeta = 7.5 \times 10^{-3}$ m. At $d_n = 286.85$, where the sensitivity to the properties of the near-surface temperature gradient are low because of the modest e -values, the synthetic antenna temperature is modified rather little. Therefore, the model that includes the solid-state greenhouse effect reproduces the entire second peak. A temperature reduction is seen at the first peak as well, for the same reason (see e -values in Fig. 7). Temperature increases are seen at the beginning and end of the curve, as well as just before the first dip. These are likely secondary-effects, caused by the higher efficiency by which solar energy is driven into the surface material.

Because of the drastic improvement seen for $\zeta \geq 7.5 \times 10^{-3}$ m, we consider the existence of a solid-state greenhouse effect consistent with MIRO measurements. We think that the prominent solid-state greenhouse effect is caused by the nature of airfall material, consisting of loosely assembled mm-cm-sized chunks that form a medium with substantial macro porosity (Pajola et al. 2016, 2017; Davidsson et al. 2021). Solar radiation is being absorbed gradually with depth, creating a sub-surface temperature peak and a positive temperature gradient in the uppermost layer that causes a clearly observable signature in the MIRO data: an unusually low antenna temperature at strongly illuminated and warming regions observed at large emergence angles.

Encouraged by these initial models, another 51 NIMBUS simulations were performed, to further expand the considered set of mantle thicknesses, tube dimensions, and ζ -values, for different thermal inertia. Many simulations aimed at a thermal inertia near ~ 30 MKS. About half of those simulations considered $\{L, r_p\} = \{20, 2\}$ mm, resulting in a relatively small radiative contribution to heat transport. A lower limit on the Hertz factor was placed so that the thermal inertia would not be reduced much below 30 MKS even for very high porosities. That resulted in the thermal inertia primarily being governed by solid-state conduction, with the total value typically varying diurnally within the range $30 \leq \Gamma \leq 35$ MKS. The other half considered $\{L, r_p\} = \{28, 6.6\}$ mm, resulting in a relatively large

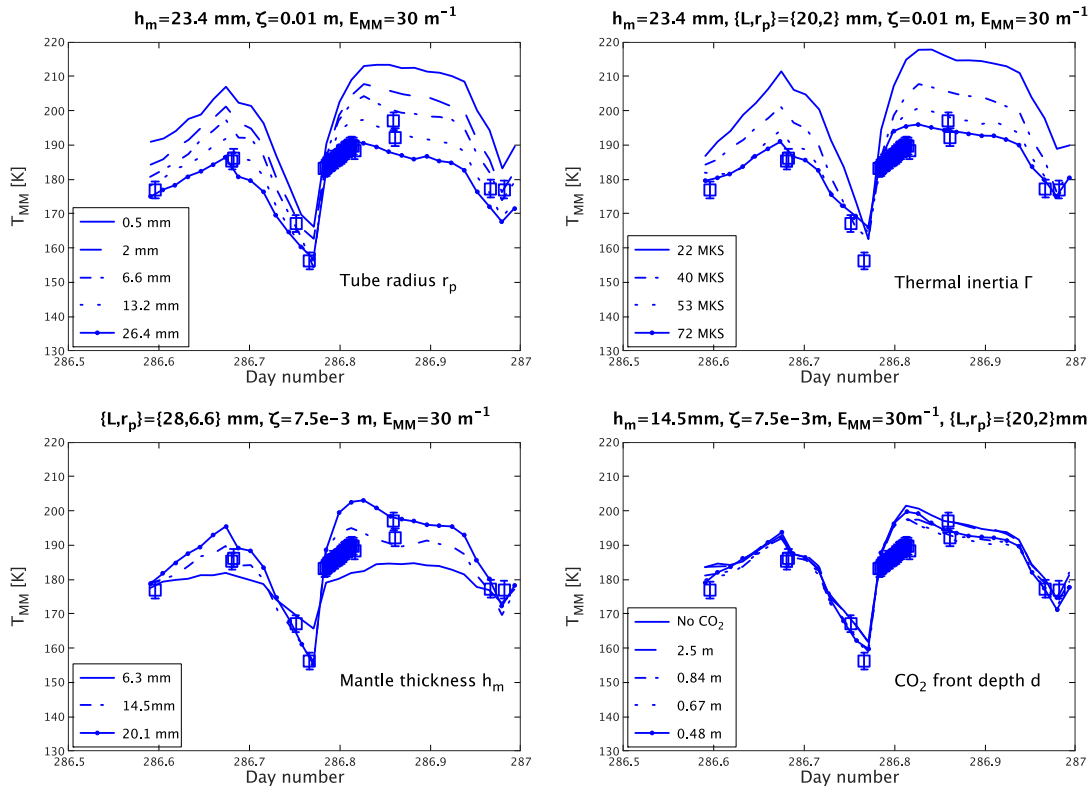


Figure 12. The panels show MIRO October 2014 MM data, and how antenna temperature curves based on NIMBUS simulations change when one parameter is varied while all others are fixed in the thermophysical model. Upper left-hand panel: effects of changing diffusivity (by varying the pore radius r_p). Note that the entire curves are being vertically displaced when r_p changes. Upper right-hand panel: Effects of changing thermal inertia, which are very small at the lowest antenna temperatures. Lower left-hand panel: effects of changing the thickness of the dust mantle. Note that those effects are very small at the very beginning/end of the curves. Lower right-hand panel: Effects of changing the depth of the CO₂ sublimation front (including one case without CO₂). The biggest effects are seen at the beginning of the curve, and at the lowest/highest temperatures.

radiative contribution to heat transport. In this case the nominal Shoshany et al. (2002) porosity-correction of heat conductivity was used, leading to negligible solid-state conduction for the high-porosity characterizing the dust mantle. That resulted in the thermal inertia primarily being governed by radiative transfer, typically varying diurnally within the range $25 \leq \Gamma \leq 40$ MKS. Two methods were used in the remaining models to consider higher thermal inertia. The first method considered $\{L, r_p\} = \{20, 2\}$ mm but multiplied the Hertz factor (having the previously mentioned enforced lower limit) with factors 2, 4, or 6 in order to push the thermal inertia (dominated by solid-state conduction) into the ranges $50 \leq \Gamma \leq 55$ MKS, $65 \leq \Gamma \leq 75$ MKS, and $80 \leq \Gamma \leq 90$ MKS, respectively. There were also cases where the Hertz factor lower limit was reduced to consider $15 \leq \Gamma \leq 25$ MKS. The second method applied the nominal Shoshany et al. (2002) Hertz factor but boosted the tube dimensions to $\{L, r_p\} = \{56, 13.2\}$ mm (yielding $35 \leq \Gamma \leq 60$ MKS) or $\{L, r_p\} = \{112, 26.4\}$ mm (yielding $55 \leq \Gamma \leq 90$ MKS). Note that heat transport dominated by radiation has a stronger temperature dependence, thus a wider diurnal thermal inertia range, than does solid-state heat conduction. We considered both options to make sure our modelling is not biased towards one particular type of behaviour. We considered mantle thicknesses ranging from 6.3 mm to 6.8 cm and e -folding scales $7.5 \times 10^{-3} \leq \zeta \leq 2.5 \times 10^{-2}$ m.

The large combined set of 81 NIMBUS models allows for systematic studies of how the antenna temperature curve changes when one given parameter changes and all other conditions are held fixed. Such a study is valuable in order to better understand how to

improve a given model curve towards a given empirical data set, by adjustments of its model parameters. The upper left-hand panel of Fig. 12 exemplifies how the synthetic antenna temperature curve changes with tube dimensions $\{L, r_p\}$. Larger pores, resulting in a larger net sublimation and cooling, lowers the antenna temperature curve, as expected. It is interesting to note that this reduction is substantial both at day and at night. To first order, changing $\{L, r_p\}$ therefore leads to a vertical displacement of the entire curve. Changes due to the thermal inertia are illustrated in the upper right panel of Fig. 12. Increasing the thermal inertia reduces the amplitude of the curve. Interestingly, the temperature at the coolest part of the curve barely changes at all. Therefore, Γ -adjustments have a large effect on the day-time temperatures while the dip temperature is very stable. Changes to the thickness of the dust mantle are illustrated in the lower left-hand panel of Fig. 12. The thicker the mantle, the larger is the amplitude of the antenna temperature curve. In this case, the temperatures at the beginning and at the end of the curve hardly changes, while there are substantial shifts elsewhere. Also note that the peak shape problem is prominent in most of these curves. As previously stated, this happens when the mantle is either too thick or the $\{L, r_p\}$ -value is too large for the considered ζ -value. In fact, there is a substantial improvement of the shape of the second peak in the lower left-hand panel of Fig. 12, as the mantle thickness is reduced.

As can be seen from Fig. 12, many modelling attempts were unsuccessful, leading to curve shapes and absolute values that are incompatible with the measured data. Only four models were formally consistent with the data ($Q > 0.01$ for ± 2.5 K error

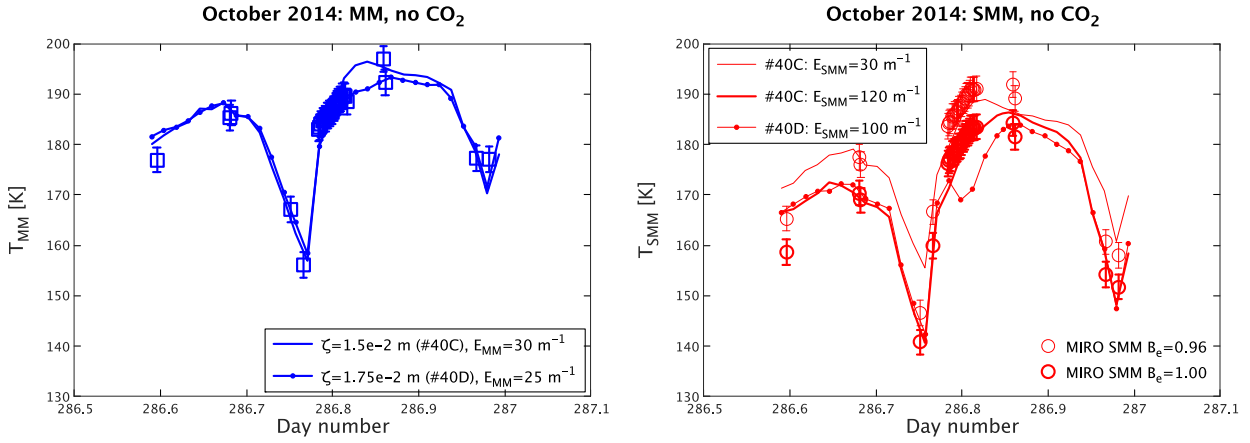


Figure 13. The best available NIMBUS-based reproductions of the MIRO 2014 October MM (left-hand panel) and SMM (right-hand panel) T_A for models without sublimating CO_2 ice. These models have $\{L, r_p\} = \{28, 6.6\}$ mm and $h_m = 20.1$ mm, but different light penetration length scales ($\zeta = 1.5 \times 10^{-2}$ m for #40C, but $\zeta = 1.75 \times 10^{-2}$ m for #40D). Model #40C requires $E_{\text{MM}} = 30 \text{ m}^{-1}$, but #40D needs $E_{\text{MM}} = 25 \text{ m}^{-1}$. The models are too warm at the beginning of the curve. At SMM, model #40C needs an unrealistically low $E_{\text{SMM}} = 30 \text{ m}^{-1}$ if $B_e = 0.96$ (and completely misses the first dip) but would increase towards $E_{\text{SMM}} \rightarrow 120 \text{ m}^{-1}$ and match most data (except being much too warm at $d_n = 286.6$) if $B_e \rightarrow 1$. The higher ζ of model #40D yields sufficiently low near-surface temperatures for night-time frost formation, and the daytime sublimation of this frost produces an unacceptable $T_{\text{sy, SMM}}$ reduction at the bin cluster (red bullet curve). That cooling is barely detectable in $T_{\text{sy, MM}}$.

bars). The two best MM solution are seen in the left-hand panel of Fig. 13. The first model (#40C) had $\{L, r_p\} = \{28, 6.6\}$ mm and the original Shoshany et al. (2002) Hertz factor, resulting in a radiation-dominated thermal inertia varying between 23–39 MKS during rotation. That model had a light penetration lengthscale of $\zeta = 1.5 \times 10^{-2}$ m, a $h_m = 20.1$ mm dust mantle thickness, and the best fit was reached for $E_{\text{MM}} = 30 \text{ m}^{-1}$, having $Q = 0.059$. The other model (#40D) was identical except that $\zeta = 1.75 \times 10^{-2}$ m, having $Q = 0.039$ at $E_{\text{MM}} = 25 \text{ m}^{-1}$. Those models suggest the MIRO MM channel would sample radiation in the top $E_{\text{MM}}^{-1} = 3.3\text{--}4.0$ cm of the surface. The largest residual is at the first bin ($d_n \approx 286.6$), where the models were somewhat too warm. It was also notoriously difficult to reach a sufficiently low-temperature at the dip ($d_n \approx 286.75$) when the fit was reasonable elsewhere.

In order to qualify as possible solutions, the same physical model should reproduce the MIRO SMM data as well. That comparison is complicated by the error margins on the beam efficiency, B_e . If $B_e = 0.96$, the MIRO SMM measurements would suggest relatively high antenna temperatures, shown in the right-hand panel of Fig. 13 by the thin red circles. Pushing the #40C SMM solution (thin red curve) to reproduce the continuous-stare bin cluster of the $B_e = 0.96$ data requires $E_{\text{SMM}} = 30 \text{ m}^{-1}$. However, because the transparency of comet analogue material is expected to increase with the wavelength ($E_{\text{MM}} < E_{\text{SMM}}$; Gary & Keihm 1978) that is not a satisfactory solution (for 67P, the average is $E_{\text{SMM}} = 100_{-33}^{+100} \text{ m}^{-1}$ according to Schloerb et al. 2015). Furthermore, that model has a significant peak shape problem, and the dip temperature is far too high. Assuming $B_e = 1$ for the SMM channel yields the somewhat cooler thick red circles, with model #40C providing the smallest residuals for $E_{\text{SMM}} = 120 \text{ m}^{-1}$, where $Q = 0.0039$ (thick red curve). As was the case for the MM channel the biggest residual is at the first bin ($d_n \approx 286.6$). Model #40D (red bullet curve), having a larger ζ -value, is very similar to #40C, except at the second peak where the temperature dips temporarily when reaching ~ 170 K (at the bin cluster of the continuous stare) and remaining substantially below the measurements until the peak tip. The reason for this phenomenon is frost formation within the dust mantle during the dip, and cooling because of water ice sublimation once the Sun illuminates Hapi D.

All $\zeta > 0$ models have rather low-surface temperatures at day, and even lower ones at night (see Fig. 11 to the lower right-hand panel), sometimes forcing vapour from the warmer interior to condense near the surface. Model #40C accumulates a maximum of 11.0 kg m^{-3} worth of water ice during the first dip (peaking ~ 2 mm below the surface), that is removed rather quickly. However, #40D accumulates 18.6 kg m^{-3} (corresponding to a volumetric abundance of ~ 10 per cent relative refractories, for an assumed porosity of $\psi = 0.8$), resulting in more substantial cooling. It is interesting to note that MIRO likely would have been capable of detecting frost removal, had it been an important process at the sampled parts of the temperature curve. VIRTIS did detect $3 \mu\text{m}$ absorption due to near-surface water ice in other regions of Hapi in September 2014, suggesting 5–14 per cent ice by volume (De Sanctis et al. 2015). Such ice was only seen near shadows, and disappeared after ~ 15 min of illumination, indicating it was frost that condensed during darkness. We note that only the NIMBUS models with $\zeta > 0$ display frost formation at night and during shadowing, typically reaching 5–10 per cent abundances (i. e., closely matching the levels inferred from VIRTIS observations). The lack of frost signatures at Hapi D according to MIRO, and its presence elsewhere at Hapi according to VIRTIS, could mean that the frost-formation efficiency varies strongly by location. Because $\zeta > 0$ seem to be one of the requirements for frost formation, this suggests that VIRTIS provides additional support for the existence of a solid-state greenhouse effect, extending beyond Hapi D.

We consider #40C and #40D marginal fits, at best. Realistically, $B_e \leq 0.98$, which means E_{SMM} could be substantially lower than 120 m^{-1} (although perhaps not as low as 30 m^{-1}). The excess temperature near $d_n \approx 286.6$ (of about 10 K) does not appear to be correctable with the means available. Figs 11 and 12 show that changes to the dust mantle thickness and the solid-state greenhouse effect parameter ζ have very weak influences on that part of the curve. The most effective way of modifying the $d_n \approx 286.6$ temperature is to change the tube dimensions and/or the thermal inertia, but that leads to large modifications elsewhere and does not solve the problem. The models with the over-all best performance also had trouble to fully reach the lowest temperature at the dip. Increasing the net sublimation and cooling capacity of the water sublimation front requires a high diffusivity, i. e.

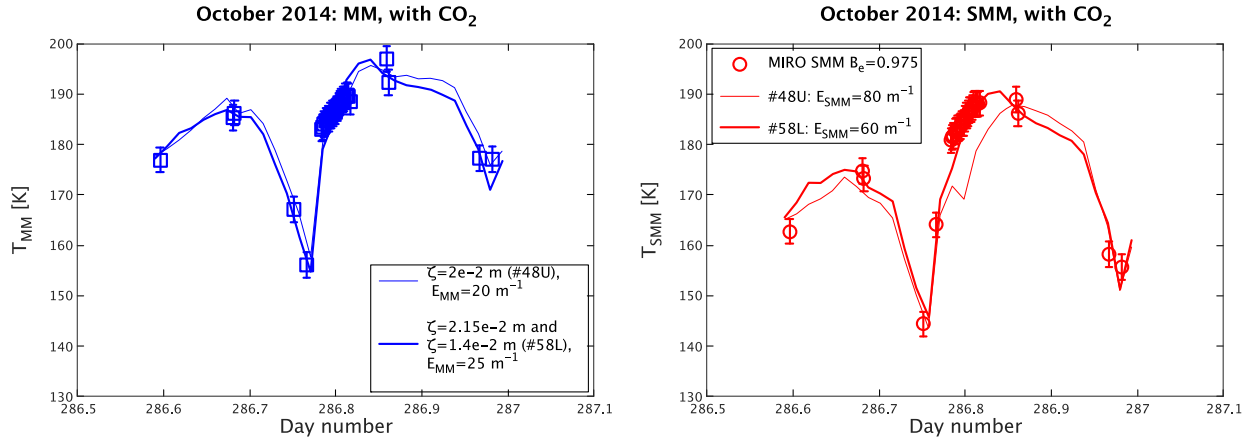


Figure 14. The best available NIMBUS-based reproductions of the MIRO October 2014 MM (left-hand panel) and SMM (right-hand panel) for models including sublimating CO₂ ice. Model #48U with tube dimensions $\{L, r_p\} = \{28, 6.6\}$ mm, light penetration length scale $\zeta = 2.0 \times 10^{-2}$ m, dust mantle thickness $h_m = 27.1$ mm, and CO₂ at a depth of 0.48 m performed best at MM (for $E_{MM} = 20 \text{ m}^{-1}$, light blue), but was less satisfactory at SMM (for $E_{SMM} = 80 \text{ m}^{-1}$, light red). A better SMM fit (model #58L, thick red) was obtained for a variable light penetration length scale (nominally $\zeta = 2.15 \times 10^{-2}$ m, but reducing to 1.4×10^{-2} m in the up per centimetre at $d_n = 286.767\text{--}286.85$) in combination with a somewhat thicker mantle ($h_m = 23.4$ mm), while tube dimensions and CO₂ depth remained the same (using $E_{SMM} = 60 \text{ m}^{-1}$). The corresponding MM model (#58L with $E_{MM} = 25 \text{ m}^{-1}$, thick blue) also performed well. Note the significant improvement at the beginning of the curves with respect to Fig. 13, that considered CO₂-free models. The best-fitting model parameters are given in Table 4.

large $\{L, r_p\}$ values. But large pores also enhances the thermal inertia because of the efficient radiative heat transfer, which tends to reduce the amplitude of the antenna temperature curve. The best compromise between sufficient cooling and not having excessive thermal inertia appeared to be $\{L, r_p\} = \{28, 6.6\}$ mm. We do not think it is possible to further reduce the residuals between model curves and the data, within the limitations of the currently considered model.

Thinking of ways to increase the cooling without having to increase the diffusivity, we decided to test the effect of having an additional sublimation front at larger depth, caused by CO₂. Initial tests, seen in the lower right-hand panel of Fig. 12, showed no measurable differences between a model without CO₂, and another model that had CO₂ at a depth of 2.5 m. However, models with CO₂ at depths of 0.48–0.84 m caused a reduction of the antenna temperature at the dip of a few Kelvin, which potentially could improve the model fits. More importantly, the addition of CO₂ had another unexpected and desirable effect: it caused a distinct drop of temperature at the beginning of the curve around $d_n \approx 286.6$. This was seen as a potential way of removing the excess temperature problem seen in CO₂-free models, without causing too large changes elsewhere. Encouraged by these initial results we ran 97 models including CO₂ (increasing the total of NIMBUS models to 192 for October 2014). These models considered different combinations of tube dimensions, ζ -values, dust mantle thicknesses, and CO₂ front depths, primarily targeting thermal inertia in the 20–40 MKS range dominated either by solid-state conduction or radiative heat transfer.

Among these CO₂ NIMBUS models, nine had higher Q -values in the MM than the best non-CO₂ NIMBUS models. The best of these (#48U), shown in the left-hand panel of Fig. 14 as a thin blue curve, had $\{L, r_p\} = \{28, 6.6\}$ mm and the original Shoshany et al. (2002) Hertz factor, resulting in a radiation-dominated thermal inertia varying between 23–38 MKS during rotation. That model had $\zeta = 2.0 \times 10^{-2}$ m, a $h_m = 27.1$ mm dust mantle, CO₂ at a depth of 0.48 m, and $Q = 0.140$ for $E_{MM} = 20 \text{ m}^{-1}$. As can be seen, the synthetic curve reproduces the measured data well. Compared to the best CO₂-free solution in the left-hand panel of Fig. 13, the fit near the first bin has been substantially improved, and the lowest temperature

at the dip is reproduced more convincingly. The corresponding SMM curve seen as a thin red curve in the right panel of Fig. 14 fits well, except at the data cluster near $d_n = 286.8$. Here, the temperature is too low, because of the removal of some frost that accumulated near the surface of the dust mantle during the shadowing period. The SMM signal is very sensitive to the temperature profile in the uppermost layer, and the difference between the model and the data is obvious. The fact that the same model conforms very well with the data in the MM channel illustrates how the local cooling quickly becomes undetectable when a thicker slab contributes to the measured signal.

At this point, we speculated if the very presence of frost could have an effect on the capability of visual radiation to penetrate into the surface material. We therefore experimented with a radiation e -folding scale being reduced to 1.4×10^{-2} m within the up per centimetre during the $d_n = 286.767\text{--}286.85$ part of the curve. This would concentrate heating to the upper part of the dust mantle and remove the frost more quickly. In those experiments, we found the best solution for $\{L, r_p\} = \{28, 6.6\}$ mm, $22 \leq \Gamma \leq 41$ MKS, $\zeta = 2.15 \times 10^{-2}$ m (except for the brief reduction to 1.4×10^{-2} m), $h_m = 23.4$ mm, and CO₂ at a depth of 0.48 m. In this case the SMM model (#58L) had $Q = 0.019$ for $E_{SMM} = 60 \text{ m}^{-1}$ when assuming $B_e = 0.975$, seen in the right-hand panel of Fig. 14 as a thick red curve. The corresponding MM model, seen in the left-hand panel of Fig. 14 as a thick blue curve had $Q = 0.086$ for $E_{MM} = 25 \text{ m}^{-1}$. This is marginally worse than model #48U, but still an acceptable fit. We consider these solutions the best achievable with the available models, and believe that the corresponding parameters collected in Table 4 are representative of the physical properties of Hapi D in October 2014.

It is significant that the same physical solution that works at SMM also reproduces the MM data. The SMM footprint primarily samples Hapi D. The fact that the larger MM footprint includes some additional terrain, and yet is consistent with the same physical conditions, indicates the presence of a solid-state greenhouse effect and shallow CO₂ ice deposits in a region that is larger than the pits themselves.

Table 4. The physical properties of the surface material of Hapi D in October and November 2014, based on best-fitting NIMBUS models to MIRO MM and SMM data. Note that a refractories/water–ice mass ratio $\mu = 2$ was used for October and $\mu = 1$ was used for November. Both values are compatible with outgassing from airfall material, with a preference for the former (Davidsson et al. 2022b). The molar CO₂ abundance was 30 per cent relative to water, as found by Davidsson et al. (2022b).

Physical quantity	Best-fit physical properties of Hapi D	
	October 2014	November 2014
Thermal inertia Γ of dust mantle	22–41 MKS	110 MKS (65 MKS in top 8 mm)
Dust mantle thickness h_m	2.3 cm	21 cm
Tube dimensions $\{L, r_p\}$	{28, 6.6} mm	{10, 1} μ m
Light penetration e -folding scale ζ	2.15×10^{-2} m (1.4×10^{-2} m when frost)	0
MM extinction coefficient E_{MM}	25 m^{-1}	80 m^{-1}
SMM extinction coefficient E_{SMM}	60 m^{-1}	600 m^{-1}
SMM single-scattering albedo w_{SMM}	0	0.1
CO ₂ sublimation front depth	0.48 m	0.44 m

4.2 November 2014

4.2.1 November: BTM results

The November data set was the first to be analysed, and the methodology was somewhat different from the final one, applied for the October data set. The initial efforts focused on a subset of the November data: the 24 bins constituting the (time-shifted) $d_n = 314.55\text{--}314.60$ continuous stare at Hapi D. The first 16 bins track a MM antenna temperature increase from 184 K to 190 K, during which Hapi D is illuminated. At that point, Hapi D moves into shadow and the remaining eight bins of the continuous stare track a temperature reduction to 185 K. The rate of cooling after the sudden switch-off of strong illumination was considered a particularly important indicator of the thermophysical properties of the surface material. A total of 16 BTM models were run for a grid of volumetric ice abundances $f_i = \{0, 0.05, 0.1, 0.2\}$ and thermal inertia-values $\Gamma = \{30, 50, 80, 100\}$ MKS. Then, a total of 108 THEMIS models were run (assuming $w_{MM} = 0$), in order to find the E_{MM} -values that yielded the smallest residuals between synthetic and measured MM antenna temperatures, for each BTM model. The best match was $\{f_i, \Gamma, E_{MM}\} = \{0.05, 100 \text{ MKS}, 30 \text{ m}^{-1}\}$ with $Q = 0.98$ (this early work assumed error bars of ± 1 K at MM and ± 1.5 K at SMM, i.e., the Q -values would be somewhat larger if applying our standard ± 2.5 K value).

For the SMM investigation of this limited data set we assumed $B_e = 0.94$ and made 52 searches with THEMIS for the best E_{SMM} -value, assuming $w_{SMM} = 0$, and additionally 202 models for which $w_{SMM} > 0$. The best $w_{SMM} = 0$ solution had $\{f_i, \Gamma, E_{SMM}\} = \{0.05, 50 \text{ MKS}, 200 \text{ m}^{-1}\}$ with $Q = 0.090$. The $\{f_i, \Gamma\} = \{0.05, 100 \text{ MKS}\}$ model (that performed best at MM) had $Q = 0.045$ for $E_{SMM} = 400 \text{ m}^{-1}$. Allowing for $w_{SMM} > 0$ the best solution was $\{f_i, \Gamma, E_{SMM}, w_{SMM}\} = \{0, 50 \text{ MKS}, 200 \text{ m}^{-1}, 0.15\}$ with $Q = 0.824$. This limited investigation suggested a lower level of sublimation cooling and potentially a higher thermal inertia in November compared to October.

The investigation was then extended to the full November 2014 data set (i.e. also including the eight bins outside the continuous stare). THEMIS simulations were run for all combinations $f_i = \{0, 0.05, 0.1\}$ and $\Gamma = \{30, 50, 80, 100\}$ MKS, primarily considering the E_{MM} values that had worked best for the limited data set, though some additional E_{MM} values were considered (25 models in total). The best model was $\{f_i, \Gamma, E_{MM}\} = \{0.05, 80 \text{ MKS}, 45 \text{ m}^{-1}\}$ with $Q = 0.624$, seen

in the left-hand panel of Fig. 15 as a thick blue curve. Two other models provided temperature curves similar to this one; $\{f_i, \Gamma, E_{MM}\} = \{0.05, 100 \text{ MKS}, 30 \text{ m}^{-1}\}$ with $Q = 0.543$ (i.e. the best fit for the $d_n = 314.55\text{--}314.60$ peak), $\{f_i, \Gamma, E_{MM}\} = \{0.1, 100 \text{ MKS}, 45 \text{ m}^{-1}\}$ with $Q = 0.226$. A fourth model, shown in the left-hand panel of Fig. 15 as a thin blue curve, had $\{f_i, \Gamma, E_{MM}\} = \{0, 30 \text{ MKS}, 35 \text{ m}^{-1}\}$ with $Q = 0.100$, for which discrepancies with respect to the data start to become obvious. All other models performed substantially worse.

Another 25 THEMIS models were run at SMM, assuming $B_e = 0.96$. The best of these models, seen as a thin red curve in the right-hand panel of Fig. 15 had $\{f_i, \Gamma, E_{SMM}, w_{SMM}\} = \{0.1, 100 \text{ MKS}, 405 \text{ m}^{-1}, 0.07\}$ with $Q = 3 \times 10^{-11}$, i.e. it did not formally fit the data (though this $\{f_i, \Gamma\}$ -combination worked well at MM). The best case from the MM study, $\{f_i, \Gamma\} = \{0.05, 80 \text{ MKS}\}$, had the smallest residuals at SMM ($Q = 2 \times 10^{-16}$) for $\{E_{SMM}, w_{SMM}\} = \{315 \text{ m}^{-1}, 0.12\}$, seen as a thick red curve in the right-hand panel of Fig. 15. In both cases, the main problem is a too slow cooling after the first peak, and a too rapid cooling after the second peak.

In summary, the BTM produced very convincing fits for the November 2014 MIRO MM data, suggesting 5–10 per cent water ice by volume and a thermal inertia of $80 \leq \Gamma \leq 100$ MKS. Although such models provided SMM antenna temperature curves with an amplitude and shape that were about right, they were not statistically compatible with the measurements. Yet, it is interesting that BTM performed far better in November than in October. This suggests that the Hapi surface material may have evolved significantly, in a manner that makes the BTM a better representation of reality. Although the BTM did not represent the MM October 2014 data well, the model in Fig. 10 with reasonable amplitude and absolute values (having $\{f_i, \Gamma\} = \{0.3, 30 \text{ MKS}\}$) suggests that the cooling by sublimation was reduced, and the thermal inertia increased, when going from October to November 2014. We now turn to NIMBUS simulations to investigate whether that model confirms that conditions have changed, and if so, what those new conditions might be.

4.2.2 November: NIMBUS results

A total of 56 NIMBUS simulations were performed in order to better understand the 2014 November MIRO observations. The models assumed (initial values) refractories to water ice mass ratio $\mu = 1$ (also consistent with the inbound water production rate; Davidsson

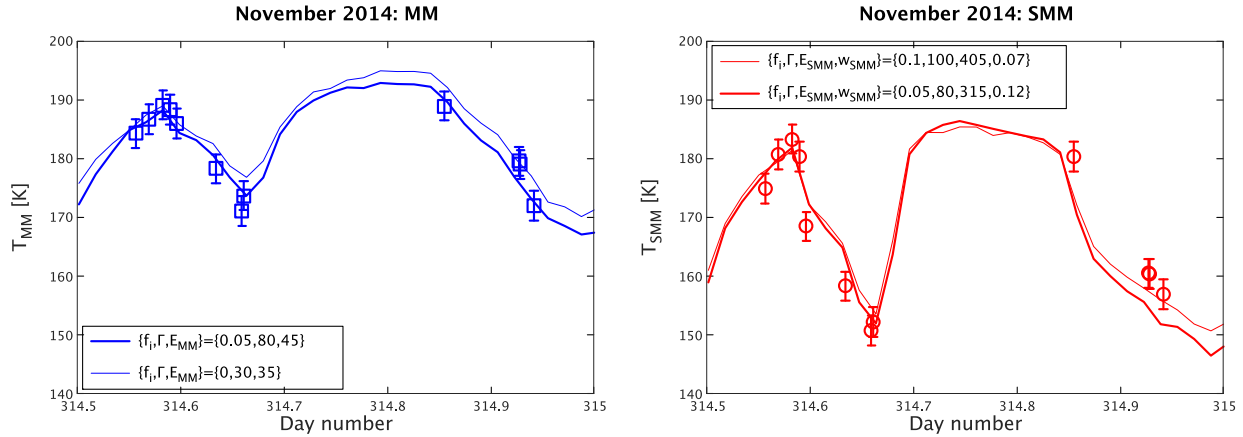


Figure 15. The best available BTM solutions versus MIRO 2014 November MM (left-hand panel) and SMM (with $B_e = 0.96$, right-hand panel) data (note that just a handful of the bins at the first ‘continuous stare’ peak were plotted to ease a comparison between models and data). Though not perfect, the BTM performed substantially better in November compared to October 2014. This suggests that some change has taken place in the near-surface material of Hapi D, so that the basic thermophysical model is a better representation of reality. This change seems to be associated with a reduction of cooling by sublimation and an increase of the thermal inertia.

et al. 2022b), 30 percent CO_2 with respect to water by number, and a porosity of 63 percent (in order to obtain a bulk density of 535 kg m^{-3}). One model was run from aphelion to November 8, 2014 (about 2.5 d before the start of the master period) in order to have a starting-point that reasonably accounted for previous evolution (in terms of temperature, stratification, etc.). All other models continued that model with new parameter combinations and used the 2.5 d (about five revolutions) as a relaxation period to adjust to the new conditions.

The first eleven models all considered conditions similar to the 2014 October solution (2.5 cm dust mantle, $\zeta = 2.15 \times 10^{-2} \text{ m}$, CO_2 at 0.44 m depth), but having smaller or higher Hertz factors compared to nominal conditions (to achieve different thermal inertia in the 40–100 MKS range) and $\{L, r_p\}$ values ($\{10, 1\} \mu\text{m}$ or $\{28, 6.6\} \text{ mm}$). This was done because of the suspected increase of thermal inertia and reduction of sublimation cooling (by lowering the diffusivity) with respect to October 2014. None of these models worked well, primarily because the MM antenna temperature amplitude was too large. The biggest difference compared to the rather successful BTM simulations turned out to be the heat capacity of the dust mantle, that was 3.4 times smaller in the NIMBUS simulations.

Therefore, 19 additional models were considered where the cell dust masses were increased 3.5–4.7 times (which also decreased the porosity), with the overall effect of producing thermal inertia in the 85–130 MKS range. These had $\{L, r_p\} = \{10, 1\} \mu\text{m}$ to minimize the sublimation cooling, and considered different combinations of dust mantle opacities (ζ values) and dust mantle thicknesses (ranging 2.5–16.4 cm). Despite the low diffusivity, most of these models were too cold. The exception was the case (model @021A) with the thickest dust mantle ($h_m = 16.4 \text{ cm}$) that had $\Gamma = 110$ –130 MKS and $\zeta = 10^{-2} \text{ m}$, which yielded $Q = 0.068$ for $E_{MM} = 100 \text{ m}^{-1}$. However, when that model was tested at the SMM wavelength, the antenna temperature amplitude was far too small.

At this point, 14 models with 3.5 times the original dust mass, and low thermal inertia (30–60 MKS) were run for different combinations of $\{L, r_p\}$, ζ , and $3.2 \leq h_m \leq 9.4 \text{ cm}$, primarily to investigate if models with low thermal inertia are viable, despite the indications from BTM that the thermal inertia is high. All these models had $Q < 0.01$, and the best cases (with Q on an $\sim 10^{-3}$ level) both had relatively thick dust mantles. It therefore seemed that the recipe for success (as

suggested by the BTM work) indeed is to consider a relatively high thermal inertia (~ 100 MKS) and a substantially smaller level of cooling (heavily reducing the diffusivity is not sufficient, but the water sublimation front has to be comparably deep as well).

Therefore, the final twelve models considered thick dust mantles ($14.4 \leq h_m \leq 27.3 \text{ cm}$), dust mass enhancements that yielded thermal inertia in the 80–140 MKS range and $\{L, r_p\} = \{10, 1\} \mu\text{m}$. Because several of these models were convincing at MM wavelength, the focus shifted more to finding ways to fit the SMM MIRO observations. The primary problem were the SMM amplitudes, although substantial improvements were seen compared to other SMM cases. The best overall solution (that somewhat degraded MM performance while substantially improving the SMM fit) was obtained by considering a somewhat lower dust mass enhancement in the top 8 mm, yielding a somewhat lower thermal inertia (~ 65 MKS) near the surface, compared to deeper parts of the mantle (~ 110 MKS).

This model (@056A) had a thick dust mantle ($h_m = 21 \text{ cm}$), was opaque ($\zeta = 0$), and had a best-fitting extinction coefficient of $E_{MM} = 80 \text{ m}^{-1}$ (resulting in $Q = 0.048$). In the SMM this model had $Q = 0.002$ for a beam efficiency of $B_e = 0.96$, when $E_{SMM} = 600 \text{ m}^{-1}$ and the single-scattering albedo was $w_{SMM} = 0.1$. Though formally not statistically consistent with the data, this solution is still an improvement upon the best BTM model (Section 4.2.1). These solutions are shown in Fig. 16 and listed in Table 4. If the MIRO SMM beam efficiency is closer to unity (as illustrated by the thin red circles in the right-hand panel of Fig. 16), this lowering of the SMM antenna temperature can be accommodated by increasing the single-scattering albedo a bit further.

The NIMBUS simulations seem to confirm the BTM results – the physical and chemical properties of Hapi D in the top decimetres is distinctively different in November 2014 compared to the previous month. The dust mantle has become substantially thicker, and the properties of this mantle have changed. The thermal inertia has increased, the diffusivity has decreased substantially, there is no longer a measurable solid-state greenhouse effect, the extinction coefficients at both MM and SMM have increased significantly (i.e. the medium is less transparent), and there appears to be a need for multiple scattering at SMM wavelengths that was not present in October. All these changes are consistent with a significant

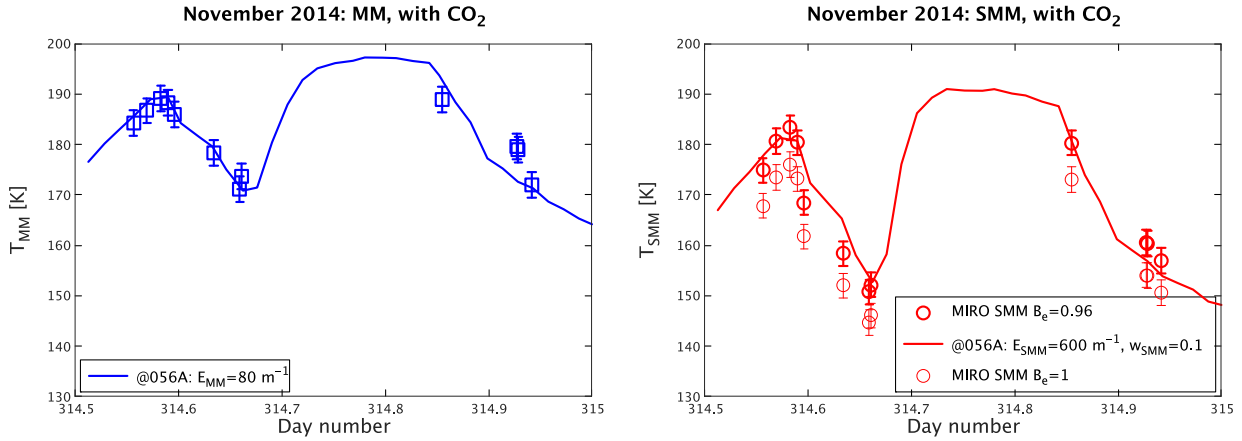


Figure 16. The best available NIMBUS-based antenna temperature solutions (model @056A) compared with MIRO November 2014 MM (left-hand panel) and SMM (right-hand panel) data. This model has a thick ($h_m = 21$ cm) and opaque ($\zeta = 0$) dust mantle with ~ 65 MKS in the top 8 mm and ~ 110 MKS below. Tubes are small, $\{L, r_p\} = \{10, 1\}$ μm , and CO_2 is at a depth of 0.44 m. The extinction coefficients are $E_{MM} = 80 \text{ m}^{-1}$ and $E_{SMM} = 600 \text{ m}^{-1}$, with a non-zero SMM single-scattering albedo of $w_{SMM} = 0.1$. These solutions confirm the differences at Hapi D in November compared to the previous month, hinted at by the BTM solutions. The cooling has been reduced because the dust mantle is thicker and the diffusivity is orders of magnitude lower, the thermal inertia and extinction coefficients have increased, the solid-state greenhouse effect is no longer detectable, and there may be some multiple-scattering at the SMM wavelength.

compaction of the granular medium (see Section 4.3 for a further discussion).

As was the case for October, the fact that the same thermophysical model provides acceptable fits simultaneously at SMM and MM wavelengths speaks against a sharp difference in physical properties between Hapi D and its immediate surroundings. Rather subtle differences in dust mantle strength and/or the exact depth of the CO_2 could have been responsible for the more obvious morphological changes at Hapi D in late December 2014, compared to the weaker alterations at Hapi C revealed by the change of the spectral slope observed by OSIRIS.

4.3 Contextual simulations

The description of the physical and chemical properties of Hapi D in October and November 2014 (summarized in Table 4) are based on interpretations of MIRO observations with thermophysical and radiative transfer models. These results give rise to a number of questions: (1) under what conditions, if any, are the physical conditions in October 2014 a natural consequence of thermophysical evolution of this region in the previous years? (2) What is causing the drastic change observed between October and November 2014, and is the short one-month time-scale for these changes realistic? (3) How is the region expected to change after 2014 November, and can an explanation be found as to why pit formation was initiated at the end of 2014 December? (4) Why did the pit changes stop at some point between late February and early March in 2015? In order to address these questions, we performed NIMBUS simulations from the May 2012 aphelion until mid-March 2015.

Table 4 states that CO_2 is present at shallow depths, and we first need to investigate if and how the supervolatile can remain relatively close to the surface over extended periods of time. We first note, that the total amount of energy absorbed by Hapi D between perihelion to aphelion (according to the model in Section 3.1) is $1.9 \times 10^9 \text{ J m}^{-2}$, the energy absorbed between the 2012 May 23 aphelion and late September 2014 is $3.1 \times 10^9 \text{ J m}^{-2}$, and a total of $4.3 \times 10^9 \text{ J m}^{-2}$ is absorbed from aphelion to perihelion. This means that Hapi D receives ~ 1.6 times more energy between aphelion and the first considered MIRO observations, compared to that absorbed

by the newly deposited airfall material near perihelion, on its way to aphelion. Therefore, we here only model the part of the orbit after May 2012, but will later discuss the effect of having been processed by an additional ~ 60 per cent of energy since the previous perihelion.

A first set of NIMBUS simulations considered model parameters consistent with our reproduction of October 2014 MIRO data ($\mu = 2$, 30 per cent CO_2 by number relative to water, $\{L, r_p\} = \{28, 6.6\}$ mm, $\zeta = 2.15 \times 10^{-2}$ m). Five models with CO_2 fronts initially located at depths between 0.19–0.50 m at aphelion were considered. These models were stopped after one year, because the CO_2 had already withdrawn to 0.79–1.11 m, i.e. significantly below the targeted 0.48 m depth (Table 4). It is clear that preservation of CO_2 within half a metre of the surface requires special conditions, if at all possible.

Davidsson et al. (2022b) performed global modelling of Comet 67P with NIMBUS and simultaneously reproduced the global H_2O and CO_2 production rates measured by Rosetta/ROSINA, both pre- and post-perihelion. They found that successful reproduction of the post-perihelion branch (when fresh airfall material deposited during the perihelion polar night is first exposed to sunlight) required a very large diffusivity on the Northern hemisphere, consistent with $\{L, r_p\} = \{0.1, 0.01\}$ m. Such a high diffusivity would be expected in material dominated by loosely packed chunks with sizes ranging MMs to decimetres. However, the pre-perihelion branch required a diffusivity corresponding to $\{L, r_p\} = \{100, 10\}$ μm . Such values are more consistent with particles ranging micrometres to MMs. Davidsson et al. (2022b) speculated that this three orders-of-magnitude drop in diffusivity taking place somewhere around aphelion was due to significant fragmentation in a top layer, caused by thermal fatigue and fracturing in brittle low-temperature material already weakened by water ice loss. Macroscopic chunks were pulverised and transformed to a low-porosity layer of fine grains. Such a layer could be MMs to centimetres thick, yet provide an efficient gas diffusion barrier. It would overlay an interior still dominated by large chunks and substantial macroporosity.

We therefore considered the same NIMBUS models as before, but applied $\{L, r_p\} = \{100, 10\}$ μm (and $\zeta = 0$ because the conditions for efficient light penetration would temporarily be removed as well). Those simulations were run for more than twice as long (until the

end of September 2014) compared to the first set, yet the CO₂ ice only withdrew to 0.70–0.79 m (meanwhile, water ice withdrew from the surface to a depth of 8.4 mm and the total dust mantle erosion was merely 2 mm). This was a substantial improvement, yet not satisfactory. A third set considered $\{L, r_p\} = \{10, 1\} \mu\text{m}$ and additionally switched to $\mu = 1$ (in order to increase the CO₂ bulk density from 105 to 144 kg m⁻³ for a fixed 30 per cent abundance relative to water). That kept CO₂ ice at 0.56–0.63 m in late September 2014 (increasing erosion to 3.4 mm because of the dust mantle bulk density reduction, and reducing the mantle thickness to 4 mm). Note that the front propagation rate only is sensitive to diffusivity when sublimation is weak (for an explanation of the lack of such sensitivity during strong sublimation, see section 3.2 in Davidsson et al. 2021).

A final test lowered the Hertz factor by a factor 4, so that the typical dust mantle thermal inertia became ~ 15 MKS instead of ~ 30 MKS. Such a reduction could take place if the quenching top layer has relatively few and small points of contact with the coarse substrate. Under such optimized conditions, CO₂ ice withdrew from 0.19 to 0.35 m between aphelion and the end of September 2014 (or by 16 cm). If the front initially was at 0.31 m, simulations showed that it withdrew by just 8 cm to 0.39 m. In this case, a 3.6-mm layer was eroded, and the dust mantle thickness became 4 mm. Considering that substantially less energy was available outbound, we therefore find the following sequence plausible: (1) the CO₂ ice was located to within ~ 0.2 m of the surface when Hapi D emerged from polar night after the 2009 perihelion; (2) it withdrew to ~ 0.3 m by the time the comet reached aphelion in 2012; (3) it withdrew further to ~ 0.4 m by the end of 2014 September.

We therefore believe we have identified the conditions that would allow for the existence of shallow CO₂ ice at Hapi D in 2014 October (~ 0.48 m according to our interpretations of MIRO measurements). It requires a combination of low diffusivity, low heat conductivity, and a high CO₂ concentration (yet, all parameters being within reasonable limits). Additionally, the CO₂ ice would have to be shallow when emerging from near-perihelion polar night on the previous orbit, suggesting substantial removal of dust and perhaps water ice during an earlier pre-perihelion pit formation event.

We postulate that the isolating and quenching layer was removed in early October 2014 by intensified erosion (most of the nominal 3.6-mm erosion takes place during September, and in reality, it may have been a factor of a few more substantial). Thereby, underlying coarse material was exposed. That removal would quickly increase the diffusivity by four orders of magnitude (here, from $\{L, r_p\} = \{10, 1\} \mu\text{m}$ to $\{L, r_p\} = \{28, 6.6\} \text{mm}$), and restore the nominal Hertz factor. That would speed up the withdrawal of both the H₂O and CO₂ fronts. As the dust mantle thickened, the near-surface opacity would decrease and ζ increase.

We ran a NIMBUS model throughout October 2014 that initially had H₂O and CO₂ fronts at 4 mm and 0.35 m, with $\zeta = 0$ during the first week, $\zeta = 4 \times 10^{-3}$ m during the second week, and $\zeta = 2.15 \times 10^{-2}$ m during the remainder of the time (except if the dust mantle developed water frost at a > 0.1 kg m⁻³ level, which triggered temporary reinstatement of $\zeta = 4 \times 10^{-3}$ m). We found that the dust mantle thickness grew to 1.3, 1.9, 4.0, and 5.8 cm during weeks #1 through #4. We also found that the CO₂ ice withdrew from 0.35 to 0.44 m. Considering that the October 2014 MIRO observations were performed during a 15-d period centred at the middle of the month (see Section 2.2), our inferred dust mantle thickness of 2.3 cm (Table 4) is consistent with the predicted dust mantle growth. In order to match a CO₂ depth of ~ 0.48 m (Table 4), the initial depth in early October should have been somewhat deeper than the 0.35 m used here (perhaps at ~ 0.40 m, as mentioned previously). However, we

think this test shows that the CO₂ likely would have stayed within centimetres of the inferred depth throughout the 15-d period, despite the high diffusivity and resulting net sublimation rate.

The contextual simulations indicate an ~ 6 cm dust mantle at the end of October 2014, while the NIMBUS best fit of November 2014 suggests an ~ 21 cm mantle at that time. Possible explanations of this discrepancy include: (1) further growth during the remaining 10 d until the first November 2014 MIRO observation, as well as to the November 20 mid-point of that measurement series; (2) more rapid growth if the dust-to-water-ice mass ratio is closer to $\mu = 2$ than the assumed $\mu = 1$ (as suggested by Davidsson et al. 2022b, for airfall material); (3) the potential presence of an ice-free layer somewhere in the 6–21-cm region. For example, a $\lesssim 14$ cm ice-free mantle may have covered H₂O- and CO₂-rich material at Hapi D as it went into polar-night during the previous apparition, to be covered by a $\gtrsim 6$ cm layer of fresh ice-rich airfall during the September 2009 perihelion. If so, that water ice could have been gradually removed during the time leading up to the end of October 2014. That could explain the jump in dust mantle thickness from ~ 6 to ~ 21 cm, as October transited into November 2014, provided that our interpretation of MIRO measurements is correct.

As previously pointed out, there is a distinct difference between the inferred October and November 2014 best-fitting solutions to MIRO data (Table 4). We suggest, that the water ice that was rapidly removed during 2014 October, left behind a fragile dust mantle made up of eroded chunks that would have been weakened by the loss of the icy ‘glue’ that held them intact. Continuously under stress and with forced relative movements caused by the CO₂ and H₂O vapour welling up from underneath, it is likely that the chunks would rub against one another and eventually crumble. We propose that the dust mantle chunks fragmented and decomposed into their smallest building-blocks, and that these tiny grains settled into a compact low-porosity layer in 2014 mid-November. Such a collapse would explain the significant increases in thermal inertia and the MM/SMM extinction coefficients, as well as the four orders-of-magnitude drop in diffusivity, and the removal of the solid-state greenhouse effect ($\zeta = 0$), seen in Table 4. Furthermore, local grain concentrations in this fine powder (forming optically active sub-units; Hapke 1993) may explain why the SMM channel seems to display signs of multiple-scattering ($w_{\text{SMM}} > 0$), as seen in lunar regolith (Gary & Keihm 1978).

We continued the contextual simulations, using 2014 November parameters and variants thereof. First, the dust bulk density was boosted a factor 4.7 (except in the top ~ 8 mm that was boosted a factor of 4) in order to account for the presumed compaction. Additionally, we set $\{L, r_p\} = \{10, 1\} \mu\text{m}$, $\zeta = 0$, and moved the water sublimation front to a depth of 21 cm. That simulation was run throughout November and 2014 December, this time focusing on the CO₂ vapour pressure profile $p_{\text{CO}_2}(z)$. We are interested in the CO₂ vapour pressure due to its potential role in pit formation, because it exerts a substantial outward force on the near-surface material. We found, that by the end of 2014 December (when pit formation first became visible, see Fig. 1, lower panels), the CO₂ ice had withdrawn to 0.57 m, and the vapour pressure at the CO₂ sublimation front had reached $p_{\text{CO}_2}(z = 0.57 \text{ m}) \approx 0.3$ kPa.

In an additional simulation we decreased the diffusivity further by an order of magnitude during December 2014, by increasing the tortuosity from unity to $\xi = \sqrt{10} \approx 3.2$. The peak H₂O and CO₂ pressures as functions of time for the total chain of contextual simulations are shown in Fig. 17 (left-hand panel). The CO₂ pressure first exceeds 0.01 kPa at 5.4 au inbound in March 2013, and remains below 0.045 kPa until late 2014 September. Because of the postulated

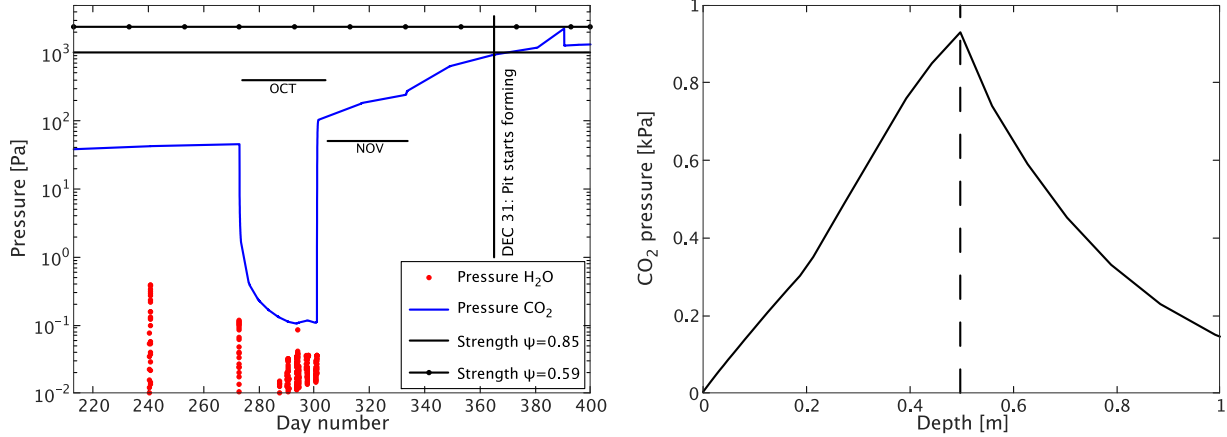


Figure 17. Left-hand panel: The peak vapour pressures of CO₂ and H₂O, from early August 2014 (arrival of *Rosetta* at Comet 67P) to late January 2015. The pressure of the shallowly located H₂O displays substantial diurnal variations (the value at every 10° of rotational angle at selected revolutions are shown; the pressure is < 10⁻² Pa as of November 2014). The deeper CO₂ yields a quasi-constant pressure on rotation-period time-scales. The dip in early October is due to the removal of an assumed low-diffusivity surface layer, and the return to a strong CO₂ pressure in early November is due to an inferred fragmentation, collapse, and compaction of solids in the upper ~ 0.5 m. The pressure difference between the CO₂ front and the surface eventually exceeds the tensile strength of porous assemblages of μm-sized grains measured in the laboratory by Güttler et al. (2009) and represented by the black lines: ~ 1 kPa (strength of a $\psi = 0.85$ medium) in late December when the first signs of pit formation were observed, reaching ~ 2.4 kPa three weeks later (strength of a $\psi = 0.59$ medium). Right-hand panel: The CO₂ pressure versus depth z in late 2014 December. The pressure peaks near the CO₂ sublimation front (located at the dashed vertical line), and falls off both inwards and outwards.

loss of the quenching top layer and the strong increase in diffusivity, the CO₂ pressure plummets to 10⁻⁴ kPa during 2014 October. The CO₂ is deep below the thermal skin depth, hence the blue curve shows no diurnal variations. However, the water ice is close to the surface, and the corresponding water vapour peak pressure (red) shows strong day/night variations. Except when $\{L, r_p\} = \{28, 6.6\}$ mm in 2014 October, the CO₂ pressure is orders of magnitude stronger than that of H₂O (note that the water pressure drops below 10⁻² Pa after 2014 October because of the thickening dust mantle, and falls outside the plot). The compaction of the dust mantle in 2014 November, reinstates a high CO₂ pressure and it continues to grow with time thanks to the higher thermal conductivity, as solar radiation intensifies. With $\xi = \sqrt{10} \approx 3.2$ after 2014 November, the CO₂ ice withdraws to 0.50 m, and the vapour pressure at the CO₂ sublimation front reaches $p_{\text{CO}_2}(z = 0.50 \text{ m}) \approx 1 \text{ kPa}$ at the end of 2014 December.

Fig. 17 (left-hand panel) also shows the tensile strengths of ‘dust cakes’ consisting of 1 μm silica grains measured in the laboratory by Güttler et al. (2009). These comet dust mantle analogues have a tensile strength of ~ 1 kPa when the dust cake porosity is $\psi = 0.85$, and a tensile strength of 2.4 kPa when $\psi = 0.59$. We note that the peak CO₂ pressure reaches ~ 1 kPa at the end of December in the NIMBUS model with $\xi \approx 3.2$, and reaches 2.4 kPa three weeks later. We note the similarity between calculated CO₂ vapour pressures and measured dust mantle analogue tensile strengths, and emphasize that the timing when this similarity took place coincides with the observed start of pit formation. We therefore propose that the pit formation observed by OSIRIS at Hapi D at the end of 2014 December, was caused by the sublimation of shallow (~ 0.5 m) CO₂ ice, that became sufficiently strong to start ejecting the mantle to space.

The right-hand panel of Fig. 17 shows $p_{\text{CO}_2}(z)$ at the end of 2014 December. The CO₂ vapour pressure peaks at the sublimation front and falls off both towards the surface and towards the deep interior (vapour diffuses both upwards and downwards, following local gradients in pressure and temperature). Note that the tensile failure would occur at the depth where the mantle is weakest, having

a strength that is smaller than the local CO₂ pressure. This depth is not necessarily coinciding with the CO₂ sublimation front, but could be more shallow. That suggests that pit deepening may have been gradual, i.e. shallower layers were ejected first and additional material was ejected later, as the pressure function adjusted to the new conditions. That is to say, the entire ~ 0.5 m layer of dust was probably not ejected at once. Removal of decimetres of dust also means that energy can reach buried CO₂ ice laterally near the rim, in addition to conduction from above. That may explain why the pits were spreading laterally over time. Finally, the depths of the pits (~ 0.5 m) would be a natural consequence of ejecting loose dust and old airfall material (but not necessarily indigenous material, still held together by water ice).

The pits of Hapi D seem to have stopped expanding at some point between 2015 February 28 and March 17 (Fig. 3). This may be understood by using the illumination simulations (see Section 3.1) and calculating the total energy absorbed by Hapi D per nucleus rotation (rot). This amount of energy peaks on 2015 February 15, at $2.98 \times 10^6 \text{ J m}^{-2} \text{ rot}^{-1}$. Between 2015 February 28 and March 17, this energy fell rapidly from $2.87 \times 10^6 \text{ J m}^{-2} \text{ rot}^{-1}$ to $2.63 \times 10^6 \text{ J m}^{-2} \text{ rot}^{-1}$, reaching the same level that had prevailed in early June 2014. It is therefore clear, that pit growth proceeded at Hapi D until the comet reached $r_h = 2.06\text{--}2.21 \text{ au}$, but at that point (by virtue of the spin axis orientation and shadows caused by nucleus topography around the Hapi valley), the daily solar heating suddenly fell to a level as low as in June 2014 (when the comet had been at $r_h = 3.9 \text{ au}$). Therefore, detectable morphology changes at Hapi D stopped.

We note that Hapi is a large region, and changes were recorded elsewhere at later times. Importantly, the ‘aeolian ripples’ (Thomas et al. 2015b) started disappearing in 2015 April, and were replaced by an expanding pit, until the ripples reformed in 2015 December (see fig. S10 in the supplementary material of El-Maarry et al. 2017). Whereas Hapi D is located close to the north pole, the aeolian ripples are found near the equator. They were strongly illuminated around the time of the May 2015 equinox, which explains their later onset with respect to Hapi D.

5 DISCUSSION

Our understanding of the evolution of Hapi D that has emerged through this work is summarized as follows. The region likely experienced excavation of several decimetres of material in February and March 2009, similarly to what OSIRIS observed on the following orbit. It entered polar night with an ~ 0.1 m dust mantle, overlaying an icy interior, rich in both H_2O and CO_2 ice. During the 2009 perihelion another ~ 0.1 m was added in the form of mm-dm-sized airfall chunks consisting of refractories and water ice. On the way toward aphelion, CO_2 withdrew from ~ 0.2 to ~ 0.3 m, while the upper few mm-to-cm lost its water ice and crumbled into a low-diffusivity top layer, having poor thermal contact with the substrate. This isolating and quenching top layer slowed the CO_2 withdrawal, and it was removed, through intensified erosion, around September 2014. When MIRO started observing Hapi D in October, the antenna temperature revealed a solid-state greenhouse effect (caused by the coarse near-surface material), and measurable signatures of shallow (~ 0.5 m) CO_2 ice. Rapid dust mantle thickening followed by collapse and compaction of the fragile dust layer in late October or early 2014 November, caused significantly increased heat conductivity, optical opacity, and microwave extinction, as well as a drastic drop in diffusivity. Those modifications caused measurable changes to the thermal emission observed by MIRO. This scenario is also supported by the OSIRIS spectrophotometry (Section 2.1.2), that suggested that the top decimetres were not particularly ice-rich. The relatively high heat conductivity and low diffusivity, caused a gradually increasing CO_2 vapour pressure and steepening pressure gradients. In late 2014 December, the tensile strength of the mantle was exceeded and pits started to form, as observed by OSIRIS. Pit formation removed the upper ~ 0.5 m of cometary material. These shallow depressions grew laterally (with a terminal velocity of $\sim 1.5 \text{ m d}^{-1}$) until the daily solar energy input fell below an activity threshold in early March 2015. Towards the end of growth, gas drag was not sufficiently strong to eject the 2.1 ± 0.4 m boulder B3. When pit growth stopped at Hapi D, the stratification may have been similar to that in early 2009. If so, pit formation may be a cyclic behaviour that repeats every orbit. We note that the escarpment stopped moving near a point where there previously was a ridge (compare Fig. 3, lower right, with Fig. 1, upper right-hand panel). That ridge possibly marks the location where the 2009 escarpment came to a halt.

We now discuss various aspects of this scenario in the light of other investigations in the literature. Cambianica et al. (2020) attempted to determine the thickness of the material deposited in Hapi during one perihelion passage by measuring the length of shadows cast by boulders. Their average for 10 boulders suggests the addition of a 1.4-m thick layer, but unfortunately the error bars for all individual boulders are as large or larger than the reported deposition thickness. We therefore consider our proposed deposition (~ 0.1 m) consistent with the measurements of Cambianica et al. (2020).

The compaction we propose to have taken place in late October or early November has not been observed in the form of a measurable subsidence. However, Davidsson, Buratti & Hicks (2022a) demonstrate that the single-scattering albedo at Hapi D was reduced between 2014 August 30 and December 10. They suggest that this darkening (presumably caused by a decrease of porosity and an increased coherent effect, as small brighter grains started acting as larger and darker optically effective particles) is a manifestation of the compaction that actually was observable by OSIRIS.

Davidsson et al. (2022b) found that CO_2 ice on average is located ~ 4 m below the surface on the Northern hemisphere. It means that the CO_2 ice at Hapi D is unusually shallow. That may explain

why pit formation is a localized phenomenon. The CO_2 sublimation front depth probably varies strongly within the Hapi valley, so that some areas evolve more calmly, while others are subjected to more violent morphological changes. If roundish and laterally expanding depressions in smooth terrain are indicative of shallow CO_2 deposits, it automatically means that the local airfall coverage is thin (because airfall chunks are not expected to carry CO_2 – that substance much be located in the native comet material, below the airfall layer). Mapping of regions with or without pit formation may therefore offer a method of ‘tomography’ that probes the thickness of smooth material in such terrain.

Davidsson et al. (2022b) also found that the mass ratio of refractories to water ice was $\mu \approx 1$ on the strongly active Southern hemisphere, and that the water abundance of airfall material is somewhat lower ($\mu \approx 2$). That increase of the refractory to water ice mass ratio is consistent with the level of water loss from cm-dm-sized chunks that are fully exposed to solar radiation in the coma during transfer times of 12 h, according to NIMBUS calculations by Davidsson et al. (2021). The current study confirms that a water abundance corresponding to $\mu = 1\text{--}2$ is consistent with the dust mantle thickness and its variation with time, as inferred from MIRO observations. Davidsson et al. (2022b) showed that the total comet production rates of H_2O and CO_2 vapours measured by *Rosetta*/ROSINA places strong constraints on the depths of the sublimation fronts of both species. They also found that reproduction of the high CO_2 production rate right after perihelion, required a high CO_2 abundance, perhaps as large as 30 per cent relative to water by number. This is consistent with what we find in the current work. Keeping CO_2 ice as close to the surface as inferred from the October 2014 MIRO observations (even in the limit of very low diffusivity and conductivity) requires a CO_2 concentration of $\gtrsim 100 \text{ kg m}^{-3}$. For a bulk density of 535 kg m^{-3} (i. e., the nucleus average), and a mass ratio of refractories to water ice of $\mu = 1\text{--}2$, this corresponds to a molar CO_2 abundance of at least 30 per cent with respect to water. That is somewhat high compared with the range of 10–23 per cent measured in massive protostars (Gerakines et al. 1999), but is consistent with the 32 ± 2 per cent range measured for low-mass protostars (Pontoppidan et al. 2008), assuming that the near-surface abundance is representative of the bulk. The latter should be more relevant analogues of the Solar System.

Birch et al. (2019) proposed a scenario to explain the presence of roundish expanding features in smooth terrain. Sloped surfaces are illuminated directly from above by the Sun, but additionally, by infrared self-heating from surrounding flat terrain. Dust is more readily removed from an inclined surface compared to one that is perpendicular to local gravity. In their view, the combination of preferential heating and facilitated water ice exposure causes the slopes to evolve into moving escarpments through a higher erosion rate than for surrounding material. We do not reject this hypothesis, that may accurately describe the origin of certain moving escarpments on 67P. However, we do not think this mechanism primarily is causing the formation of the particular pits studied in this paper. Our thermophysical modelling shows that superficial water ice barely is active at the prevailing illumination conditions. The MIRO antenna temperatures seem to require the presence of an additional cooling agent besides water. CO_2 activity offers a substantially more compelling explanation of the observed dramatic phenomenon, owing to its volatility. The engine that drives escarpment movement is buried decimetres under ground, and is more sensitive to reductions of that depth, than to near-surface topography. Once the mantle has been ejected at one point, CO_2 activity near the escarpment base will intensify and rapidly remove additional material, until the escarpment

enters a region where the CO₂ ice is located too deeply to lift material, or the level of illumination becomes too low.

Another scenario was proposed by Bouquety et al. (2022). They measured a range of morphometrical parameters describing the dimensions, shapes, and orientations for 131 depressions on 67P, and found an analogy with terrestrial alases and martian scalloped depressions. Such structures on Earth and Mars form when water ice is evacuated from a soil, and the remaining porous solid loses its mechanical integrity and collapses. Bouquety et al. (2022) therefore propose a similar formation scenario for the depressions on 67P. These have depths ranging 0.4–16 m, with a mean and standard deviation of 4.8 ± 4.5 m. Additionally, Thomas (2020) report depth measurements of a shallow depression in Anubis, and found that its elevation was reduced by ~ 2 m between September 2014 and June 2016. If the Bouquety et al. (2022) scenario is correct, it implies large local variations in the dust mantle thickness. The average thickness required to explain the observed water production rate, is ~ 0.02 m (Davidsson et al. 2022b), and the switch-off of dust jets (that are common across the entire nucleus) just beyond the terminator requires a water ice sublimation front at ~ 0.006 m according to Shi et al. (2016). In pit-forming regions, the dust mantle would have to be ~ 5 m thick on average. We note that a CO₂ sublimation front average depth of ~ 4 m is necessary to explain the carbon dioxide production rate curve of 67P according to Davidsson et al. (2022b). The similarity between the average pit depth and the average CO₂ front depth suggests that ejection of dust and water ice due to CO₂ activity is an alternative to the water loss and mantle collapse proposed by Bouquety et al. (2022). Further analysis is needed to demonstrate whether the CO₂-driven ejection of a ≥ 5 m thick layer indeed is possible, i. e., if sufficient CO₂ pressure can be reached at such depths to overcome the tensile strength of the overlying ice–dust mixture. Whereas Bouquety et al. (2022) see subsidence as the major pit-forming mechanism, we here see the collapse as a smaller prelude, that does not lead to detectable morphological changes (put perhaps leads to darkening, as previously mentioned; Davidsson et al. 2022a). In the currently proposed scenario, morphological changes come after compaction and darkening, and are due to ejection of material, not subsidence.

In order to further investigate the role of CO₂ ice in pit formation and escarpment expansion on 67P, the MIRO data base should be searched for observations at the time and place of other prominent examples of morphological changes in smooth terrain. It would be particularly interesting to perform an analysis of the Imhotep region prior to, and during, the May–July 2015 events documented by Groussin et al. (2015b). We hope that the current paper serves as an inspiration and guide on how to perform such an investigation. It would be important to better understand whether near-surface CO₂ ice is common within smooth terrain on 67P, or if the pits in Figs 1–3 are unique. Such an investigation could prove extremely valuable in the context of a cryogenic comet sample–return mission. Retrieval of CO₂-rich material at a few decimetres depth is substantially easier and cheaper than being forced to drill several metres. Knowing where to sample is another difficult practical problem that needs to be solved. If escarpments in smooth terrain prove to be indicative of shallow CO₂ deposits, such visible surface expressions of past activity could be exploited during reconnaissance prior to sampling. The unique capability of microwave instruments to measure sub-surface temperatures from orbit could further facilitate the search for accessible supervolatiles.

As a final comment on our work, we note that Fig. 17 (right-hand panel) shows an interesting phenomenon: the CO₂ vapour pressure *below* the CO₂ sublimation front falls to very small values over

a distance that is comparable to the depth of the front below the surface. In addition to the pressure difference between the front and the surface that is responsible for ejecting mantle material, there is also a strong pressure difference between the front and deeper regions, that would strive to displace material downwards. It means that the CO₂ vapour not only can eject shallow material into the coma, but it might also be capable of compressing material at depth.

The structural changes of a porous medium with its pores filled with a pressurized gas or liquid are studied in the branch of continuum mechanics known as poroelasticity, first formulated in detail by Biot (1941). The equation of motion for the solid describes its coupling to the gas;

$$\rho \frac{\partial^2 u}{\partial t^2} = G \frac{\partial \sigma}{\partial z} - \frac{2(1 + \nu_p)G}{3(2 - \nu_p)H} \frac{\partial p}{\partial z} + \frac{G}{1 - 2\nu_p} \frac{\partial \epsilon_v}{\partial z}, \quad (9)$$

where ρ is the density, u is the displacement, t is the time, z is depth, G is the shear modulus, $\sigma = K\partial u/\partial z$ is the stress (K is the bulk modulus), ν_p is the Poisson ratio, p is the gas pressure, H^{-1} is the poroelastic expansion coefficient, and ϵ_v is the volume change of the solids. As long as the tensile material strength (first right-hand term) balances the pressure force (second right-hand term), the solid is static and the other terms are zero. Once the material yields, particle acceleration begins and the medium is deformed according to equation (9) until balance is restored anew. If equation (9) is integrated over a slab of thickness dz , the force due to gas pressure is proportional to the pressure difference between the slab walls, which explains the importance of the pressure profile in Fig. 17 (right-hand panel): the prerequisites for ejection above the front and compression below the front, are co-existing. In this context, we note that thermophysical comet nucleus models typically treat dust mantle ejection by requiring that the combined gas drag force and centrifugal force overcome nucleus gravity on a grain-by-grain basis (e.g. Shul’man 1972; Rickman, Fernández & Gustafson 1990; Espinasse et al. 1993; Orosei et al. 1995). However, in the seminal paper by Fanale & Salvail (1984), the dust mantle ejection criterion was formulated for an entire mantle slab of thickness dz (as discussed above), and they indeed applied the pressure difference over the slab in their criterion. In the context of sub-surface compaction, we are interested in understanding which magnitude the pressure difference might reach, compared to the compressive strength of the solids.

A numerical experiment was performed with NIMBUS, where the model in Fig. 17 was propagated to mid-February 2015. At that point, the diurnal illumination profile was scaled up to peak at the flux expected at the perihelion sub-solar point of Comet 67P. Such conditions are not relevant for Hapi D but could have been for other parts of the comet. After two weeks of cycling at those flux levels, the CO₂ vapour pressure peaked at 4.9 kPa, which may be considered the highest CO₂ vapour pressure achievable for 67P at a depth of ~ 0.5 m (but note that CO₂ at ~ 0.2 m at the south pole reached a pressure of 19 kPa at perihelion; Davidsson et al. 2022b). According to the work of Güttler et al. (2009) on compressive strength, 1 μ m-grain silica powder would compress to a porosity $\psi = 0.73$ if the pressure reaches 4.9 kPa. Mixtures of dust and ices are stronger, and by applying the method described by Davidsson (2021) for an ice volumetric fraction of 40 per cent, such a mixture compacts to $\psi = 0.76$ at 4.9 kPa. These values are similar to the bulk porosity of 0.75–0.85 inferred for the nucleus itself (Kofman et al. 2015). Taken at face value, this would not suggest significant additional compression of the nucleus material because of the CO₂ vapour pressure.

However, the measured porosity–pressure relation is based on short-term strength and ignores the creep deformation that would take place when the medium is subjected to a continuous stress for

weeks and months. Laboratory investigations of creep in icy soils subjected to long-term loads show that the strain (i.e. the degree of deformation, here equivalent with compaction) increases with time (e.g. Fish 1983; Gardner, Jones & Harris 1984; Hampton 1986). Measurements of the strain for terrestrial snow (which constitutes an upper limit in terms of strength, because ice/dust mixtures are weaker than pure ice; Lorek et al. 2016) shows that

$$\epsilon = \frac{\sigma}{33 \text{ GPa}} \left(1 - \frac{T}{273 \text{ K}}\right)^{-0.65} \left(\frac{\rho}{0.9 \text{ Mg m}^{-3}}\right)^{-9} t^{0.6} \quad (10)$$

with t measured in hours (Meussen, Mahrenholtz & Oerter 1999). Considering compaction from an assumed bulk porosity of $\psi = 0.8$ to 0.6 (equivalent to a strain $\epsilon = 0.75$), and assuming $\sigma = 4.9 \times 10^{-6}$ GPa, $T = 130$ K, and $\rho = 0.3 \text{ Mg m}^{-3}$, then that compaction could be achieved in seven months.

Furthermore, strength typically decreases with increasing size scales. This suggests that comet nucleus material on the metre-scale and above might be weaker than the strength measured in the laboratory by Güttler et al. (2009) on much smaller scales. Indeed, by studying collapsed overhangs on 67P, Groussin et al. (2015a) found that the compressive strength of cometary material was merely 0.03–0.15 kPa on 5–30-m scales.

Compression of the type suggested here was not observed in the KOSI experiments 3–7 that included CO₂ (Lämmerzahl 1995). However, the diffusivity was rather high ($\sim 0.1 \text{ m}^2 \text{ s}^{-1}$; Benkhoff & Spohn 1991) in these experiments, because of relatively coarse grains and similarly-sized pore spaces (0.01–1 mm; Lämmerzahl 1995), resulting in modest CO₂ partial pressures (peaking at 13 Pa; Hsiung & Roessler 1989). This is insufficient to cause compaction. We reach kPa-level pressures by having 10^{-5} – $10^{-4} \text{ m}^2 \text{ s}^{-1}$ diffusivities, as expected for porous but homogeneous aggregates of μm -sized monomers.

The CO₂ sublimation front can therefore be thought of as a slowly propagating wave that compacts the material before it, leaving behind a mixture of refractories and water ice that is compressed with respect to the deep interior. The compaction process might be self-reinforcing to a certain level. By decreasing the porosity, which lowers the diffusivity but increases heat conductivity, the CO₂ sublimation front needs to develop ever-increasing vapour pressures to elevate the vapour mass flux rate to the point where most heat conducted to the front is being consumed by net sublimation. This effect decreases the porosity further, which facilitates additional compaction, and so on. The material that is observable on the surface of comet nuclei could therefore very well have experienced substantial compression, structural alteration, and mechanical modification before it became exposed. Such processing could affect the way near-surface material fractures, and the size-frequency distribution function of coma material.

Davidsson et al. (2022b) found that the post-perihelion CO₂ production rate of 67P required a substantial near-perihelion reduction of diffusivity (at the depth where CO₂ vapour is being produced) on the Southern hemisphere, by a factor of 10–250. They proposed that this reduction of diffusivity was due to the movement of the CO₂ sublimation front into a deeper layer that it previously had compressed during strong near-perihelion activity. Therefore, sub-surface compression due to CO₂ activity appears consistent with ROSINA data.

This type of CO₂-driven near-surface compaction might explain some puzzling observations of comets. Comparisons between the densities of the top few meters of comets inferred from radar observations, and those of the bulk nuclei derived from non-gravitational force modelling, led to suggestions of a thin compacted

surface layer on comets even before *Rosetta* (Davidsson, Gutiérrez & Rickman 2009; Kamoun et al. 2014). The CONSERT experiment of *Rosetta/Philae* showed that the upper few hundred metres of the small lobe of 67P has an average dielectric constant (at 90 MHz) of $\epsilon' = 1.27$, and an inferred porosity of $\psi = 0.75$ – 0.85 (Kofman et al. 2015). Further analysis of this data set revealed a radial gradient of the dielectric constant, taking values of $\epsilon' = 1.7$ near the surface that transitioned to $\epsilon' = 1.3$ at a depth of 150 m (Ciarletti et al. 2015) or of ‘tens/hundreds of metres’ (Ciarletti et al. 2018). This suggested an increase of porosity and/or decrease of the dust-to-ice mass ratio with depth (Ciarletti et al. 2015). Measurements by *Philae/SESAME-PP* showed that $\epsilon' = 2.45 \pm 0.2$ (at 409–758 Hz) within the top metre at Abydos, consistent with a porosity of $\psi < 0.5$ or 0.75 for dust analogues of carbonaceous or ordinary chondrites, respectively (Lethuillier et al. 2016). The work by Brouet et al. (2016) on SESAME-PP data suggests the upper limit on porosity may even be as low as 0.18–0.55. Comparing with ground-based Arecibo radar observations of 67P ($\epsilon' = 1.9$ – 2.1 at 2.38 GHz in the top ~ 2.5 m; Kamoun et al. 2014), it was suggested by Lethuillier et al. (2016) that there ‘may also be a gradient in porosity in the first meters of the cometary mantle’. Temperature measurements by *Philae/MUPUS-TM* at Abydos are consistent with a thermal inertia of 85 ± 35 MKS and a porosity of $\psi = 0.3$ – 0.65 near the surface (Spohn et al. 2015).

We propose that compaction of material passed by the CO₂ sublimation front, caused by the CO₂ vapour pressure gradient below the front, is responsible for the observed increase of porosity with depth (the H₂O vapour pressure is orders of magnitude weaker, and is not capable of such compression of the solids). We have demonstrated that the CO₂ pressure difference between the front and the interior is sufficiently large to reduce the porosity from $\psi = 0.75$ – 0.85 at large depth, to ~ 0.6 in near-surface regions that previously have been passed by the CO₂ sublimation front, on time-scales that are short compared to the orbital period. Such a porosity gradient is consistent with the porosity values at depth and near the surface inferred from the *Rosetta* and Arecibo observations described above. Davidsson et al. (2022b) show that the CO₂ sublimation front on average is located ~ 4 m below the surface on the Northern hemisphere, and ~ 2 m below the surface on the Southern hemisphere of 67P, which roughly would correspond to the thickness of the compressed layer. We further propose that this type of compaction is responsible for the formation of consolidated material on 67P observed by OSIRIS (e.g. Thomas et al. 2015a; El-Maarry et al. 2015b). It is visually recognisable by the ‘rock-like’ appearance caused by its brittleness that makes it prone to fracturing and forming angular faceted shapes (e.g. El-Maarry et al. 2015a; Auger et al. 2018). Sheet-like overhangs with thicknesses of 5–30 m and lateral extensions of 10–100 m at the time of eventual collapse (Groussin et al. 2015a) serve as illustrations that the compacted near-surface layers of consolidated material are thin and stronger than the material that has been eroded from underneath them.

6 CONCLUSIONS

We present *Rosetta/OSIRIS* observations that document the gradual growth of a ~ 0.5 m deep pit in the Hapi region on Comet 67P, from 2014 December 31 until 2015 March 17, when it reached lateral dimensions of $140 \times 100 \text{ m}^2$. We use thermophysical models and a radiative transfer equation solver, in order to analyse *Rosetta/MIRO* microwave observations of the region in October and November, 2014, prior to pit formation. Our main conclusions are the following:

(i) MIRO measurements are consistent with the existence of a solid-state greenhouse effect on 67P, which is active in coarse airfall material with high macro porosity.

(ii) MIRO has provided an estimated inferred depth of the CO₂ sublimation front on 67P, being ~ 0.5 m at the particular pit-forming region in Hapi.

(iii) In October 2014, the pit-forming region of Hapi was characterized by a low-thermal inertia ($\sim 30 \pm 10$ MKS), a thin (~ 2 cm) dust mantle, a large diffusivity (indicative of pores and channels in the 1–10 cm range), a measurable solid-state greenhouse effect, the presence of shallow (~ 0.5 m) CO₂ ice, modest microwave extinction coefficients, and no evidence of multiple-scattering.

(iv) The properties of the near-surface material of comet nuclei may change drastically and rapidly. Between October and November 2014, the pit-forming region at Hapi experienced a rapid removal of water ice, and a collapse of the dust mantle that resulted in significant compaction. These events measurably changed the thermal inertia (from 30 to 110 MKS, falling toward 65 MKS at the surface), the dust mantle thickness (from ~ 2 to ~ 21 cm), reduced the diffusivity by four orders of magnitude (indicative of pores and channels in the 1–10 μ m range), increased the microwave extinction coefficients by a factor 3–10, and introduced multiple-scattering at SMM wavelengths.

(v) Contextual thermophysical simulations with NIMBUS show that CO₂ can be maintained within the 0.2–0.5-m region below the surface due to seasonally recurring pit-formation events, combined with low-thermal inertia and low-diffusivity near aphelion.

(vi) We constrain the conditions under which the CO₂ vapour pressure becomes sufficiently high to overcome the tensile strength of porous 1 μ m grain dust mantle analogues, and to do so at a location in the orbit that coincides with the observed start of pit formation: a high-thermal inertia of ~ 100 MKS, a low diffusivity consistent with homogeneous assemblages of μ m-sized grains (with a non-zero but low tortuosity), and CO₂ ice located to within 0.5 m of the surface.

(vii) Accordingly, we propose that pit formation and escarpment propagation in smooth terrain on comet nuclei may be primarily due to rapid ejection of dust into the coma driven by superficial CO₂ ice sublimation.

(viii) We find that the CO₂ vapour pressure at the sublimation front may become sufficiently strong to cause an inward compression of comet material. Accordingly, we propose that the moving CO₂ front compresses material before it, and leaves behind a compacted mixture of dust and water ice that is exposed at the surface of comets.

(ix) Accordingly, we propose that the compaction of material in the upper few meters in 67P with respect to the more porous material at depth, inferred from observations by CONSERT and SESAME on *Rosetta/Philae*, as well as by the Arecibo radar, is caused by processing during CO₂ sublimation.

(x) We propose that the consolidated terrain observed on the surface of 67P (where it is not covered by smooth terrain) is the observable surface expression of material that has been partially or primarily compacted by previous CO₂ sublimation.

(xi) We recommend enhanced efforts to investigate other pit-forming events observed by OSIRIS and MIRO, *vis-à-vis* near-surface supervolatile deposits and visually observable surface expressions of recent pit formation and escarpment movements. This is particularly important in the context of cryogenic comet sample-return missions, for which deep excavation in the hunt for cold ice drastically drives up costs and technical complexity. We recommend the usage of microwave instruments on orbiting reconnaissance spacecraft in order to locate suitable sampling sites.

ACKNOWLEDGEMENTS

We dedicate this paper to the memory of our dear friend and colleague, Dr. Claudia J. Alexander (1959–2015), Project Scientist of the US portion of the Rosetta mission, whose dedication to science and the search for knowledge remains a lasting inspiration to all of us. Parts of this research were carried out at the Jet Propulsion Laboratory, California Institute of Technology, under a contract with the National Aeronautics and Space Administration. PJG acknowledges financial support from the State Agency for Research of the Spanish Ministerio de Ciencia, Innovación y Universidades through project PGC2018–099425–B–I00 and through the ‘Center of Excellence Severo Ochoa’ award to the Instituto de Astrofísica de Andalucía (SEV–2017–0709). MRELM. is partly supported by the internal grant (8474000336–KU–SPSC). The MIRO instrument was developed by an international collaboration led by NASA and the Jet Propulsion Laboratory, California Institute of Technology, with contributions from France, Germany, and Taiwan. OSIRIS was built by a consortium led by the Max–Planck–Institut für Sonnensystemforschung, Göttingen, Germany, in collaboration with CISAS, University of Padova, Italy, the Laboratoire d’Astrophysique de Marseille, France, the Instituto de Astrofísica de Andalucía, CSIC, Granada, Spain, the Scientific Support Office of the European Space Agency, Noordwijk, The Netherlands, the Instituto Nacional de Técnica Aeroespacial, Madrid, Spain, the Universidad Politécnica de Madrid, Spain, the Department of Physics and Astronomy of Uppsala University, Sweden, and the Institut für Datentechnik und Kommunikationsnetze der Technischen Universität Braunschweig, Germany. The support of the national funding agencies of Germany (DLR), France (CNES), Italy (ASI), Spain (MEC), Sweden (SNSB), and the ESA Technical Directorate is gratefully acknowledged. We thank the *Rosetta* Science Ground Segment at ESAC, the *Rosetta* Mission Operations Centre at ESOC and the *Rosetta* Project at ESTEC for their outstanding work enabling the science return of the *Rosetta* Mission.

DATA AVAILABILITY

The data underlying this article will be shared on reasonable request to the corresponding author.

REFERENCES

- Anderson J. A., Sides S. C., Soltesz D. L., Sucharski T. L., Becker K. J., 2004, in Mackwell S., Stansbery E., eds, *Lunar and Planetary Inst. Technical Report Vol. 35, Lunar and Planetary Science Conference. Lunar and Planetary Institute, Houston, TX*, p. 2039
- Auger A.-T. et al., 2015, *A&A*, 583, A35
- Auger A.-T. et al., 2018, *Icarus*, 301, 173
- Barucci M. A. et al., 2016, *A&A*, 595, A102
- Benkhoff J., Spohn T., 1991, *Geophys. Res. Lett.*, 18, 261
- Biot M. A., 1941, *J. App. Phys.*, 12, 144
- Birch S. P. D. et al., 2019, *Geophys. Res. Lett.*, 46, 12794
- Biver N. et al., 2019, *A&A*, 630, A19
- Bouquety A., Groussin O., Jorda L., Sejourne A., Costard F., Bouley S., 2022, *A&A*, 662, A72
- Brouet Y. et al., 2016, *MNRAS*, 462, S89
- Brown R. H., Matson D. L., 1987, *Icarus*, 72, 84
- Cambianica P. et al., 2020, *A&A*, 636, A91
- Choukroun M. et al., 2015, *A&A*, 583, A28
- Ciarletti V., Levasseur-Regourd A. C., Lasue J., Statz C., Plettemeier D., Hérique A., Rogez Y., Kofman W., 2015, *A&A*, 583, A40
- Ciarletti V. et al., 2018, *MNRAS*, 469, S805
- Clow G. D., 1987, *Icarus*, 72, 95

- Davidsson B. J. R. et al., 2021, *Icarus*, 354, 114004
- Davidsson B. J. R., 2021, *MNRAS*, 505, 5654
- Davidsson B. J. R., Rickman H., 2014, *Icarus*, 243, 58
- Davidsson B. J. R., Skorov Y. V., 2002, *Icarus*, 159, 239
- Davidsson B. J. R., Gutiérrez P. J., Rickman H., 2009, *Icarus*, 201, 335
- Davidsson B. J. R., Buratti B. J., Hicks M. D., 2022a, *MNRAS*, 516, 5125
- Davidsson B. J. R., Samarasinha N., Farnocchia D., Gutiérrez P., 2022b, *MNRAS*, 509, 3065
- De Sanctis M. C. et al., 2015, *Nature*, 525, 500
- Deshapriya J. D. P. et al., 2016, *MNRAS*, 462, S274
- El-Maarry M. R. et al., 2015a, *Geophys. Res. Lett.*, 42, 5170
- El-Maarry M. R. et al., 2015b, *A&A*, 583, A26
- El-Maarry M. R. et al., 2016, *A&A*, 593, A110
- El-Maarry M. R. et al., 2017, *Science*, 355, 1392
- Espinasse S., Coradini A., Capria M. T., Capaccioni F., Orosei R., Salomone M., Federico C., 1993, *Planet. Space Sci.*, 41, 409
- Fanale F. P., Salvail J. R., 1984, *Icarus*, 60, 476
- Filacchione G. et al., 2016, *Science*, 354, 1563
- Fish A. M., 1983, Thermodynamic Model Of Creep At Constant Stresses And Constant Strain Rates. US Army Corps of Engineers, Hanover
- Fornasier S. et al., 2015, *A&A*, 583, A30
- Fornasier S. et al., 2016, *Science*, 354, 1566
- Fornasier S. et al., 2017, *MNRAS*, 469, S93
- Fornasier S. et al., 2019, *A&A*, 630, A13
- Frerking M., Gulkis S., Hofstadter M., Kamp L., Koch T., Nowicki R., Schloerb F. P., 2020, MIRO Experiment User Manual. NASA Planetary Data System, College Park, MD
- Gardner A. R., Jones R. H., Harris J. S., 1984, *Cold Regions Sci. Technol.*, 9, 271
- Gary B. L., Keihm S. J., 1978, *Proc. Lunar Planet. Sci. Conf.*, 9, 2885
- Gerakines P. A. et al., 1999, *ApJ*, 522, 357
- Glassmeier K.-H., Boehnhardt H., Koschny D., Kührt E., Richter I., 2007, *Space Sci. Rev.*, 128, 1
- Groussin O. et al., 2015a, *A&A*, 583, A32
- Groussin O. et al., 2015b, *A&A*, 583, A36
- Gulkis S. et al., 2007, *Space Sci. Rev.*, 128, 561
- Gulkis S. et al., 2010, *Planet. Space Sci.*, 58, 1077
- Gulkis S. et al., 2015, *Science*, 347, aaa0709
- Güttler C., Krause M., Geretshauer R. J., Speith R., Blum J., 2009, *ApJ*, 701, 130
- Hampton C. N., 1986, PhD thesis. University of Nottingham, Nottingham
- Hapke B., 1993, Theory of Reflectance And Emittance Spectroscopy. Cambridge Univ. Press, Cambridge
- Hofstadter M., Pan L., von Allmen P., Lee S., Springer P., 2019, ROSETTA-ORBITER 67P MIRO 4 PRL V2.0, RO-C-MIRO-4-PRL-67P-V2.0t, ESA Planetary Science Archive and NASA Planetary Data System
- Horai K.-I., 1971, *J. Geophys. Res.*, 76, 1278
- Hsiung P., Roessler K., 1989, in Hunt J. J., Guyenne T. D., eds, Physics and Mechanics of Cometary Materials, Vol. 302, ESA Special Publication. p. 191
- Hu X. et al., 2017, *A&A*, 604, A114
- Jorda L. et al., 2016, *Icarus*, 277, 257
- Kamoun P., Lamy P. L., Toth I., Herique A., 2014, *A&A*, 568, A21
- Kaufmann E., Hagermann A., 2015, *Icarus*, 252, 144
- Kaufmann E., Kömle N. I., Kargl G., 2006, *Icarus*, 185, 274
- Kaufmann E., Kömle N. I., Kargl G., 2007, *Adv. Space Res.*, 39, 370
- Keller H. U., Kührt E., 2020, *Space Sci. Rev.*, 216, 14
- Keller H. U. et al., 2007, *Space Sci. Rev.*, 128, 433
- Keller H. U. et al., 2015b, *A&A*, 583, A34
- Keller H. U., Mottola S., Skorov Y., Jorda L., 2015a, *A&A*, 579, L5
- Keller H. U. et al., 2017, *MNRAS*, 469, S357
- Klinger J., 1980, *Science*, 209, 271
- Klinger J., 1981, *Icarus*, 47, 320
- Kofman W. et al., 2015, *Science*, 349, aab0639
- Kömle N. I., Dettliff G., Dankert C., 1990, *A&A*, 227, 246
- Lagerros J. S. V., 1996, *A&A*, 315, 625
- Lämmerzahl P., 1995, *Adv. Space Res.*, 15, 19
- Lee S. et al., 2015, *A&A*, 583, A5
- Lethuillier A. et al., 2016, *A&A*, 591, A32
- Lorek S., Gundlach B., Lacerda P., Blum J., 2016, *A&A*, 587, A128
- Marshall D. et al., 2018, *A&A*, 616, A122
- Matson D. L., Brown R. H., 1989, *Icarus*, 77, 67
- Meussen B., Mahrenholtz O., Oerter H., 1999, *Cold Regions Sci. Technol.*, 29, 177
- Mottola S. et al., 2014, *A&A*, 569, L2
- Mottola S. et al., 2015, *Science*, 349, aab0232
- Müller T. G., 2002, *Meteo. Planet. Sci.*, 37, 1919
- Oklay N. et al., 2016a, *MNRAS*, 462, S394
- Oklay N. et al., 2016b, *A&A*, 586, A80
- Orosei R., Capaccioni F., Capria M. T., Coradini A., Espinasse S., Federico C., Salomone M., Schwehm G. H., 1995, *A&A*, 301, 613
- Pajola M. et al., 2016, *MNRAS*, 462, S242
- Pajola M. et al., 2017, *MNRAS*, 469, S636
- Pajola M. et al., 2019, *MNRAS*, 485, 2139
- Pätzold M. et al., 2019, *MNRAS*, 483, 2337
- Pommerol A. et al., 2015, *A&A*, 583, A25
- Pontoppidan K. M. et al., 2008, *ApJ*, 678, 1005
- Press W. H., Teukolsky S. A., Vetterling W. T., Flannery B. P., 2002, Numerical Recipes in C. Cambridge Univ. Press, Cambridge
- Preusker F. et al., 2015, *A&A*, 583, A33
- Rezac L., Zhao Y., Hartogh P., Ji J., Marshall D., Shi X., 2019, *A&A*, 630, A34
- Rezac L. et al., 2021, *A&A*, 648, A21
- Rickman H., Fernández J. A., Gustafson B. Å. S., 1990, *A&A*, 237, 524
- Robie R. A., Hemingway B. S., Takei H., 1982, *American Mineralogist*, 67, 470
- Schloerb F. P. et al., 2015, *A&A*, 583, A29
- Schwehm G., Schulz R., 1999, *Space Sci. Rev.*, 90, 313
- Shi X. et al., 2016, *A&A*, 586, A7
- Shoshany Y., Prialnik D., Podolak M., 2002, *Icarus*, 157, 219
- Shul'man L. M., 1972, in A.Chebotarev G., Kazimirchak-Polonskaia E. I., Marsden B. G., eds, Proc. IAU Symp. 45, The Motion, Evolution of Orbits, and Origin of Comets. Springer, Dordrecht, p. 271
- Sierks H., the OSIRIS Team, 2020, ROSETTA-ORBITER 67P OSINAC 4 [PRL-MTP006/008, ESC1-MTP013, ESC2-MTP014, ESC4-MTP024, EXT1-MTP025/026, EXT2-MTP028/030] RDR-INF-REFL V1.0, RO-C-OSINAC-4 [PRL-67P-M06/08, ESC1-67P-M13, ESC2-67P-M14, ESC4-67P-M24, EXT1-67P-M25/26, EXT2-67P-M28/30]-INF-REFL-V1.0, ESA Planetary Science Archive and NASA Planetary Data System
- Sierks H. et al., 2015, *Science*, 347, aaa1044
- Spohn T. et al., 2015, *Science*, 349, aab0464
- Tancredi G., Rickman H., Greenberg J. M., 1994, *A&A*, 286, 659
- Taylor M. G. T., Altobelli N., Buratti B. J., Choukroun M., 2017, *Phil. Trans. R. Soc. A*, 375, 20160262
- Thomas N., 2020, An Introduction to Comets. Post-Rosetta Perspectives. Springer Nature, Cham
- Thomas N. et al., 2015a, *Science*, 347, aaa0440
- Thomas N. et al., 2015b, *A&A*, 583, A17
- Thomas N. et al., 2018, *Planet. Space Sci.*, 164, 19
- Tubiana C. et al., 2015, *A&A*, 583, A46
- Urquhart M. L., Jakosky B. M., 1996, *J. Geophys. Res.*, 101, 21169
- Weast R. C., 1974, Handbook of Chemistry and Physics, 55 edn. CRC Press, Cleveland

¹Jet Propulsion Laboratory, California Institute of Technology, M/S 183-401, 4800 Oak Grove Drive, Pasadena, CA 91109, USA

²University of Massachusetts, Department of Astronomy, LGRT-B 847 710 North Pleasant Street, Amherst, MA 01003-9305, USA

³LESIA, Université Paris Cité, Observatoire de Paris, Université PSL, CNRS, Sorbonne Université, 5 place Jules Janssen, F-92195 Meudon, France

⁴Institut Universitaire de France (IUF), 1 rue Descartes, F-75231 PARIS CEDEX 05, France

⁵Independent researcher, Berlin, Germany

⁶Instituto de Astrofísica de Andalucía (CSIC), Glorieta de la Astronomía s/n. E-18080 Granada, Spain

⁷*Jet Propulsion Laboratory, California Institute of Technology, M/S 183-601, 4800 Oak Grove Drive, Pasadena, CA 91109, USA*

⁸*Jet Propulsion Laboratory, California Institute of Technology, M/S 321-655, 4800 Oak Grove Drive, Pasadena, CA 91109, USA*

⁹*200 W Highland Dr., Unit 104, Seattle, WA 98119, USA*

¹⁰*Jet Propulsion Laboratory, California Institute of Technology, M/S 183-301, 4800 Oak Grove Drive, Pasadena, CA 91109, USA*

¹¹*Institut für Geophysik und extraterrestrische Physik (IGeP), Technische Universität Braunschweig, Mendelssohnstr. 3, D-38106 Braunschweig, Germany*

¹²*Deutsches Zentrum für Luft- und Raumfahrt (DLR), Institut für Planetenforschung, Asteroiden und Kometen, Rutherfordstr. 2, D-12489 Berlin, Germany*

¹³*Max Planck Institute for Solar System Research, Justus-von-Liebig-Weg 3, D-37077 Göttingen, Germany*

¹⁴*European Space Agency (ESA), European Space Astronomy Centre (ESAC), Camino Bajo del Castillo s/n, E-28692 Villanueva de la Cañada, Madrid, Spain*

¹⁵*Centrum Badań Kosmicznych Polskiej Akademii Nauk, Bartycka 18A, PL-00716 Warszawa, Poland*

¹⁶*Department of Physics and Astronomy, Uppsala University, Box 516, SE-75120 Uppsala, Sweden*

¹⁷*Jet Propulsion Laboratory, California Institute of Technology, M/S 168-200, 4800 Oak Grove Drive, Pasadena, CA 91109, USA*

¹⁸*CNR-IFN Padova, Via Trasea 7, I-35131 Padova, Italy*

¹⁹*Aix Marseille Univ, CNRS, CNES, LAM, Marseille, France*

²⁰*German Aerospace Center (DLR), Institute of Optical Sensor Systems, Rutherfordstr. 2, D-12489 Berlin, Germany*

²¹*Space Research and Planetology Division, Physikalisches Inst., University of Bern, Sidlerstrasse 5, CH-3012 Bern, Switzerland*

²²*Istituto di Astrofisica e Planetologia Spaziali – IAPS/INAF, Via del Fosso del Cavaliere 100, I-00133 Roma, Italy*

²³*Space and Planetary Science Center, and Department of Earth Sciences, Khalifa University, PO Box 127788 Abu Dhabi, UAE*

²⁴*Department of Physics and Astronomy, University of Padova, Vicolo Osservatorio 3, I-35122 Padova, Italy*

²⁵*INAF-Astronomical Observatory of Padova, Vic. Osservatorio 5, I-35122 Padova, Italy*

This paper has been typeset from a $\text{\TeX}/\text{\LaTeX}$ file prepared by the author.